

THE UNIVERSITY OF MICHIGAN
COLLEGE OF ENGINEERING
Department of Electrical Engineering
Space Physics Research Laboratory

Scientific Report No. 5

AN ATOMIC OXYGEN BEAM SYSTEM FOR THE INVESTIGATION
OF MASS SPECTROMETER RESPONSE IN THE UPPER ATMOSPHERE

Hasso B. O. Niemann

ORA Project 07065

under contract with:

NATIONAL AERONAUTICS AND SPACE ADMINISTRATION
GODDARD SPACE FLIGHT CENTER
CONTRACT NO. NAS 5-9113
GREENBELT, MARYLAND

administered through:

OFFICE OF RESEARCH ADMINISTRATION ANN ARBOR

June 1969

ABSTRACT

An atomic oxygen beam system has been designed and tested for the laboratory evaluation of mass spectrometers used in upper atmospheric measurements. The atomic oxygen is generated by thermal dissociation of molecular oxygen on the surface of a tungsten filament heated to 2800°K. A symmetrical bidirectional beam is produced to permit simultaneous monitoring of the particle flux in the beam while target experiments are being conducted. Flux levels of 5×10^{14} particles/cm²sec over a cross-sectional area of 1 cm² have been produced with a relative atomic oxygen concentration of 70%. At flux levels below 10^{13} particles/cm²sec, relative atomic oxygen concentrations of more than 90% were obtained. The oxygen beam is of high purity and free from chemically active contaminants. Strong chemical and cryogenic pumping are used to reduce background gas contributions to less than 1%.

Measurements of the relative atomic concentration in the beam were made with an open ion-source quadrupole spectrometer. The absolute flux of molecular oxygen was determined with the aid of an enclosed omegatron mass spectrometer. The combined use of both instruments permitted a determination of the magnitude of the atomic oxygen flux in the beam.

Measurements of the net atomic recombination and absorption were made with two stainless steel omegatron systems, one of which was gold-plated. Little difference was found between the performance of the two instruments. Initial exposure of the omegatron system to an atomic flux of about 10^{13} atoms/cm²sec showed 80% absorption and 20% recombination. After a two-hour exposure to atomic oxygen, the absorption decreased to 65% and net recombination increased to 35%, indicating a partial saturation of the surface. A small flux dependence of the net absorption and net recombination was observed for both instruments.

ACKNOWLEDGEMENTS

I wish to express my thanks to the people who have encouraged me in my research during the past several years as well as those who have assisted and encouraged me in the preparation of the thesis. I am especially indebted to Professor William G. Dow, Chairman of my doctoral committee, for many stimulating discussions and suggestions and guidance in the thesis research. Mr. George R. Carignan, Director of the Space Physics Research Laboratory, also a member of my doctoral committee, has advised me in the experimentation and interpretation of data. In addition, he has generously made available the facilities of the Space Physics Research Laboratory for the accomplishment of the work.

I am most grateful to the other members of my committee, Professors Chiao M. Chu, Karl T. Hecht, and Gunnar Hok, who have been helpfully critical and understanding.

Many people in the Space Physics Research Laboratory have given much help in the completion of the work. In particular, I wish to acknowledge the assistance of Richard W. Simmons, Bud J. Campbell, Heinz J. Grassl, Richard A. Jacoby, and Martha A. Moon. The invaluable assistance of Frank S. Lee throughout the experimental phase of the investigation is

gratefully acknowledged.

Finally, I wish to give special thanks to Gerald A. Schmitt, Helen G. Denning, and Roslyn A. Drummond who have given freely of their time. Their critical reading of the manuscript several times, their pertinent suggestions and assistance in the technical details necessary for the completion of the manuscript are greatly appreciated.

The research for the thesis was supported by the National Aeronautics and Space Administration, Contract No. NAS5-9113, Goddard Space Flight Center, Greenbelt, Maryland.

TABLE OF CONTENTS

	Page
ACKNOWLEDGEMENTS	ii
LIST OF SYMBOLS	vii
LIST OF TABLES	xvi
LIST OF FIGURES	xvii
CHAPTER I: INTRODUCTION	1
CHAPTER II: THE PROBLEMS OF DIRECT MEASUREMENTS IN THE ATMOSPHERE AND THE NEED FOR A LABORATORY OXYGEN BEAM GENERATOR	4
2.1 BACKGROUND	4
2.2 EXTENSION OF THE GAS DYNAMIC THEORY TO INCLUDE GAS SURFACE INTERACTIONS WITH APPLICATION TO FLIGHT MEASUREMENTS OF ATMOSPHERIC ATOMIC OXYGEN	11
2.2.1 Recombination of Atoms inside a Chamber with Uniform Surfaces	11
2.2.2 Recombination of Atomic Oxygen inside a Chamber with Nonuniform Surfaces	25
2.3 SIMPLE SURFACE PROCESSES	33
2.4 DETERMINATION OF THE FRACTIONAL SURFACE COVERAGE	45
2.5 DISCUSSION OF ADSORPTION AND RECOMBINATION MODELS	48
2.6 VALIDITY OF THE STEADY STATE ASSUMPTION	54
CHAPTER III: AN ATOMIC OXYGEN BEAM GENERATOR	58
3.1 METHODS FOR GENERATING ATOMIC OXYGEN	58
3.1.1 Glow Discharge Method	58

	Page
3.1.2 Thermal Decomposition of Ozone	59
3.1.3 Thermal Dissociation of Oxygen Molecules	60
3.2 GENERATION OF ATOMIC OXYGEN BY THERMAL DISSOCIATION ON A HOT TUNGSTEN SURFACE	66
3.3 DESIGN OF THE ATOMIC OXYGEN BEAM SYSTEM	71
3.3.1 General Design Considerations	71
3.3.2 Technique for Measurements of the Flux Intensity and the Relative Concentration of Atoms in the Oxygen Beam	72
3.3.3 Determination of the Fractional Dissociation and the Relative Concentration of Atoms from Quadrupole Measurements	85
3.3.4 Determination of the Absolute Particle Flux	93
3.3.5 Electronic Instrumentation	96
3.3.6 The Atomic Oxygen Beam System	97
3.3.7 The Vacuum System	103
3.3.8 System Assembly and Preparation	114
3.4 BEAM STUDIES	120
3.4.1 Flux Dependence of the Fractional Dissociation	120
3.4.2 Demonstration from Mass Spectra of Production of a Beam Primarily Consisting of Oxygen Atoms	122
3.4.3 The Strong Dependence of the Fractional Dissociation on the Temperature of the Tungsten Filament	135
3.4.4 Flux Intensity Profile of the Oxygen Beam	139
3.5 DISCUSSION OF THE RESULTS	144
CHAPTER IV: EXPERIMENTAL STUDIES	155
4.1 ATOM RECOMBINATION AND ABSORPTION IN THE OMEGATRON SYSTEM	155
4.2 EVALUATION OF A GOLD-PLATED OMEGATRON SYSTEM	160
4.3 EVALUATION OF A STAINLESS STEEL OMEGATRON SYSTEM	166
4.4 DISCUSSION OF THE RESULTS	168

	Page
CHAPTER V: CONCLUSIONS AND SUGGESTIONS	179
BIBLIOGRAPHY	183
APPENDIX A: ATOMIC OXYGEN GENERATION BY THERMAL DISSOCIATION ON HOT TUNGSTEN	191
APPENDIX B: DETERMINATION OF THE WALL TEMPERATURE OF THE ATOMIC OXYGEN SOURCE	197
APPENDIX C: DERIVATION OF EQUATIONS RELATING ATOMIC AND MOLECULAR FLUXES OF THE OXYGEN BEAM TO THE PARTICLE DENSITIES, NET RECOMBINATION, AND ADSORPTION INSIDE THE OMEGATRON CHAMBER	200
APPENDIX D: DERIVATION OF RELATIONS BETWEEN INCOMING AND OUTGOING MASS FLUXES IN THE OMEGATRON SYSTEM BY TAKING INTO CONSIDERATION RECOMBINATION, PERMANENT ADSORPTION OF ATOMIC OXYGEN, AND THE FORMATION OF NITROUS OXIDE	206
APPENDIX E: PARTICLE FLUX THROUGH A KNIFE-EDGE ORIFICE OF A MOVING VEHICLE	212

LIST OF SYMBOLS

a	probability of adsorption
a_o	probability of adsorption with no activation energy
a_o'	probability of adsorption in a nonisothermal system
a_1, a_2	sticking probability of atomic oxygen and molecular nitrogen respectively (Appendix D)
A_1, A_2	effective surface area of the tungsten filament for radiation of heat and titanium tube for the absorption of heat respectively (Appendix B)
b	evaporation rate of atoms
b_o	surface constant
b_1, b_2	evaporation rate of atomic oxygen and molecular nitrogen (Appendix D)
C	net loss of atomic oxygen in the omegatron chamber
\bar{C}	net absorption of atomic oxygen in the omegatron chamber
C_o	most probable velocity of ambient gas
C'	modified net loss of atomic oxygen
d	wall thickness of the titanium tube
e	effective emissivity (Appendix B)
e_1, e_2	emissivity of the tungsten filament and titanium tube respectively (Appendix B)
E_a	activation energy of adsorption
E_a'	activation energy for adsorption in a nonisothermal system
E_D	activation energy for surface recombination from the gas phase
E_m	activation energy for surface diffusion
E_s	activation energy for surface recombination

LIST OF SYMBOLS (Continued)

$f(\vec{u}, \vec{v})$	Maxwell-Boltzmann velocity distribution of a moving medium
$F(s)$	modified thermal transpiration relation
$f_1(\theta)$	probability of finding an adsorption site
$f_2(\theta)$	probability of finding an occupied adsorption site
$g(Z)$	acceleration of gravity at altitude Z
G	collimation factor
h	Planck's constant (6.6253×10^{-34} J sec)
H_i	scale height of the i^{th} atmospheric constituents $= \frac{kT(Z)}{m_i g(Z)}$
$I_{\Omega c}(\ell), I_{\Omega h}(\ell)$	ion current of constituent ℓ at the omegatron, c without dissociation, h during dissociation
$I_{\Omega T}(O_2)$	molecular oxygen ion current in the omegatron during dissociation
k	Boltzmann constant (1.3805×10^{-23} J/deg)
K	loss factor of molecular oxygen
K'	corrected loss factor
k_3, \dots, k_9	rate coefficients for dissociation and oxidation (Appendix A)
ℓ	number of distinct surface patches
$\bar{\ell}$	characteristic length of the test chamber
ℓ_{Ω}	distance of omegatron orifice from the tungsten filament
$m(\ell)$	mass of constituent
n	number of particles adsorbed per unit area
N	number of available adsorption sites per unit area
\vec{n}	unit vector normal to the chamber orifice

LIST OF SYMBOLS (Continued)

$n(t)$	particle density in the test chamber at time t
$n_1(\ell)$	atmospheric particle density of constituent ℓ
$n_2(\ell)$	particle density of constituent ℓ in the test chamber
n_b	beam particle density in the quadrupole ion source
n_{bg}	background particle density in the oxygen source vacuum chamber
$n_c(O_2)$	average beam particle density of molecular oxygen at the quadrupole ion source when the tungsten filament is at room temperature
$n_h(O_2)$	average beam particle density of molecular oxygen at the quadrupole ion source when the tungsten filament is heated
Δn_i	fraction of particles which leave the test chamber after the i^{th} bounce
$n_\ell(Z)$	atmospheric particle density of the constituent ℓ at altitude Z
n_o	initial particle density
n_s	particle density of multiple scattered particles in the quadrupole ion source
n_{sc}	particle density in the ionization region caused by one collision scattering
$n_{\Omega h}(\ell), n_{\Omega c}(\ell)$	particle density of constituent ℓ in the omegatron chamber, c when the dissociation is off, h when dissociation is on
p	escape probability
P	pumping speed of the vacuum pump
p_i	escape probability after the i^{th} bounce
p_{ij}	collision probability of a particle emitted from surface patch i and collision with patch j

LIST OF SYMBOLS (Continued)

p_{io}	probability of escape through the orifice from the i^{th} surface density
p_{oj}	collision probability of a particle entering through the orifice and colliding with patch j
q	heat conductivity (Appendix B)
Q	heat of adsorption
R	universal gas constant (8.314×10^7 erg/mole $^\circ$ K)
R	net recombination of atomic oxygen in the omegatron chamber
R'	corrected net recombination
r_{ij}	distance from a surface element of patch i to a surface element of patch j
s, \bar{s}	speed ratios
S_b	beam aperture area of the quadrupole ion source
S_{fil}	surface area of the omegatron filament
S_i	surface area of i^{th} patch
S_o	area of the test chamber orifice or exit area of beam source
$S_{qp}(\ell)$	sensitivity of the quadrupole mass spectrometer for constituent ℓ
S_s	venting area of the quadrupole ion source
S_Ω	area of the orifice in the omegatron chamber
$S_\Omega(\ell), S_{qp}(\ell)$	sensitivity of the omegatron (Ω) or quadrupole (qp) for constituent
t	time
T	absolute temperature
$T(Z)$	kinetic gas temperature at altitude Z
$T_1(\ell)$	kinetic temperature of the atmospheric atoms of constituent ℓ

LIST OF SYMBOLS (Continued)

T_2	gas temperature in the test chamber
T_2, T_3	temperature of the inner and outer surface of the titanium tube respectively (Appendix B)
T_b	kinetic temperature of beam particles
T_{fil}	temperature of the tungsten filament
t_o	average time between wall collisions
T_s	kinetic temperature of scattered particles in the quadrupole ion source
T_w	temperature of the titanium tube walls
$T_{\Omega}(\ell)$	kinetic temperature of gaseous compound ℓ in the omegatron chamber
$T_{\Omega h}(\ell)$	kinetic temperature of gaseous constituents ℓ in the omegatron chamber when dissociation is on
$T_{\Omega R}(O_2)$	kinetic temperature of recombined atomic oxygen in the omegatron chamber
\vec{u}	vehicle velocity
$U_c(\ell), U_h(\ell)$	quadrupole electrometer output voltage for constituent ℓ , c for dissociation off and h for dissociation on
U_o	quadrupole electrometer output voltage
V	chamber volume
\vec{v}	velocity of gas particles
\bar{v}	average particle velocity
$\bar{v}_1(\ell), \bar{v}_2(\ell)$	average thermal velocities of ambient atoms and atoms in the test chamber of constituent ℓ
\bar{v}_b	average velocity of beam particles
\bar{v}_{bg}	average thermal velocity of the background particles
$\bar{v}_c(O_2)$	average velocity of molecular oxygen in the beam when the tungsten filament is at room temperature

LIST OF SYMBOLS (Continued)

$\bar{v}_h(\ell)$	average velocity of constituent ℓ in the beam when dissociation is on
$v_{pl}(\ell)$	most probable thermal velocity of the ambient constituent ℓ
W	net heat flow from the tungsten filament into the titanium envelope (Appendix B)
x_1, x_2	black body radiation of the tungsten filament and titanium tube respectively (Appendix B)
Z	altitude
Z_0	reference altitude
α	angle of attack
α	thermal accommodation coefficient
$\bar{\alpha}$	real number, smaller than unity
$\alpha_{eff}(\ell)$	effective thermal accommodation coefficient of constituent ℓ
β	spherical coordinate of the velocity vector (Appendix E)
β_i	angle between the direction of an element of the i^{th} patch and the point of observation
γ	recombination coefficient of atomic oxygen
γ_{13}	formation coefficient for N_2O by collisions of gaseous atomic oxygen with adsorbed atomic oxygen
γ_{31}	formation coefficient for N_2O by collisions of molecular nitrogen with adsorbed atomic oxygen
γ_i	recombination coefficient of oxygen atoms on the i^{th} surface patch
$\epsilon(\gamma)$	correction term due to recombination of atoms
η	relative atomic oxygen concentration in the beam
$\bar{\eta}$	apparent relative atomic oxygen concentration in the beam

LIST OF SYMBOLS (Continued)

θ	fractional surface coverage (or spherical coordinate of the flux vector, Appendix E only)
θ', θ''	fractional surface coverage of atomic oxygen and molecular nitrogen respectively (Appendix D only)
κ_D	probability of direct recombination
κ_{Do}	real constant equal or smaller than unity
κ_s	probability of surface recombination
κ_s'	modified probability of surface recombination
λ	probability of absorption of atomic oxygen
μ_i	probability of dissociation and oxidation
μ_{ieff}	effective probability of dissociation and oxidation
ν	average number of collisions
τ	adsorption time constant
$\bar{\tau}$	test chamber time constant
τ_{av}	average sticking time
τ_o	period of lattice vibration
T	fractional dissociation
\bar{T}	apparent fractional dissociation
Φ	spherical coordinate of the flux vector (Appendix E)
$\phi(\ell)$	particle flux of constituent ℓ
$\phi_1(\ell)$	flux of constituent ℓ which flows into the test chamber
ϕ_2	total flux in the test chamber
$\phi_2(\ell)$	flux of constituent ℓ from the test chamber

LIST OF SYMBOLS (Continued)

ϕ_b	beam particle flux on the quadrupole ion source
ϕ_{bg}	background particle flux into the omegatron chamber
ϕ'_{bg}	background flux into the omegatron chamber from the source chamber
$\Phi_c(O_2)$	mass flux of molecular oxygen at the quadrupole ion source when the tungsten filament is at room temperature
$\phi_h(\ell)$	particle flux of constituent ℓ at the quadrupole ion source, h when dissociation is on, c when dissociation is off
$\Phi_h(\ell)$	mass flux of constituent ℓ at the quadrupole ion source when the tungsten filament is heated
$\Delta_i \phi_2(\ell)$	fraction of the flux of constituent ℓ which leaves the test chamber after the i^{th} bounce
ϕ_{ij}	impact flux on surface patch j resulting from emissions of particles from patch i
ϕ_{qp}	net particle flux leaving the quadrupole ion source
ϕ_s	particle flux at the atomic oxygen source exit
ϕ_{sc}	scattered particle flux through the ionization region of the quadrupole ion source
ϕ_w	impact flux at the tungsten filament
ψ_i	particle flow from the i^{th} surface patch
ψ_{ij}	particle flow from the i^{th} surface patch to the j^{th} surface patch
ω	hopping frequency
ω_{12}, ω_{21}	probability of nitrous oxide formation from gaseous atomic oxygen and adsorbed nitrogen and from gaseous nitrogen and adsorbed atomic oxygen respectively
ω_o	lattice vibration frequency
Ω	solid angle

LIST OF SYMBOLS (Concluded)

- Ω_p solid angle subtended by the getter pump
orifice at the source exit
- Ω_s solid angle subtended by the effective
ionization region of the quadrupole ion source
at the extraction tube entrance

LIST OF TABLES

Table		Page
4.1	RESULTS OF MEASUREMENTS OF RECOMBINATION AND ABSORPTION IN THE OMEGATRON SYSTEMS.	161
4.2	MEASURED QUADRUPOLE AND OMEGATRON DATA AND APPARENT KINETIC TEMPERATURE OF THE MOLECULAR OXYGEN.	170
4.3	FINAL RESULTS OF NET RECOMBINATION AND ABSORPTION OF OXYGEN ATOMS IN THE OMEGATRON SYSTEM.	173

LIST OF FIGURES

Figure		Page
2.1	Geometric diagram of two surface elements of a chamber with nonuniform surfaces.	31
2.2	Potential energy curve for chemisorption of a diatomic molecule (Ehrlich, 1959).	36
2.3	Potential energy diagram for an activated complex in chemisorption on a nonuniform surface.	39
3.1	Fractional dissociation and oxide formation versus primary molecular oxygen flux on a tungsten surface at 2800°K.	67
3.2	Cross-sectional view of the ion source of the ATLAS quadrupole mass spectrometer.	75
3.3	Schematic diagram of the bidirectional atomic oxygen beam system.	79
3.4	Modified ion source of the ATLAS quadrupole mass spectrometer.	83
3.5	Retarding potential curve of the quadrupole mass spectrometer.	92
3.6	Cross-sectional view of the atomic oxygen source.	99
3.7	Atomic oxygen source assembly.	100
3.8	Front view of the atomic oxygen source assembly. The position of the tungsten filament is shown in the center of the double wall titanium tube.	101
3.9	Cross-sectional view of the titanium getter pump.	109
3.10	Double wall titanium getter pump with ionization gauge and disassembled titanium filament.	113
3.11	Atomic oxygen beam system (complete assembly).	115
3.12	Tungsten filament temperature versus filament voltage.	117

LIST OF FIGURES (Continued)

Figure		Page
3.13	Fractional dissociation versus molecular oxygen as measured at the omegatron orifice.	121
3.14a	Quadrupole mass spectra, tungsten filament at room temperature with background gases only.	124
3.14b	Quadrupole mass spectra, tungsten filament at room temperature with a molecular oxygen flux of 10^{14} molecules $\text{cm}^{-2}\text{sec}^{-1}$ at the omegatron orifice, and with the shutter open.	125
3.14c	Quadrupole mass spectra, tungsten filament at room temperature with a molecular oxygen flux of 10^{14} molecules $\text{cm}^{-2}\text{sec}^{-1}$ at the omegatron orifice, and with the shutter closed.	126
3.15a	Quadrupole mass spectra, tungsten filament at 2800°K with a molecular oxygen flux of 10^{14} molecules $\text{cm}^{-2}\text{sec}^{-1}$ at the omegatron orifice and with the shutter open.	128
3.15b	Quadrupole mass spectra, tungsten filament at 2800°K with a molecular oxygen flux of 10^{14} molecules $\text{cm}^{-2}\text{sec}^{-1}$ at the omegatron orifice and with the shutter closed.	129
3.16a	Omegatron mass spectra, tungsten filament at room temperature with a molecular oxygen flux of 10^{14} molecules $\text{cm}^{-2}\text{sec}^{-1}$ and with the shutter open.	132
3.16b	Omegatron mass spectra, tungsten filament at room temperature with a molecular oxygen flux of 10^{14} molecules $\text{cm}^{-2}\text{sec}^{-1}$ and with the shutter closed.	133
3.16c	Omegatron mass spectra, tungsten filament at 2800°K with a molecular oxygen flux of 10^{14} molecules $\text{cm}^{-2}\text{sec}^{-1}$ and with the shutter open.	134

LIST OF FIGURES (Concluded)

Figure		Page
3.17	Dependence of the mass 32 and mass 16 output signal on the temperature of the tungsten filament.	136
3.18	Dependence of the fractional dissociation on the temperature of the tungsten filament.	138
3.19	Angular flux profile of the oxygen beam when the tungsten filament is at room temperature (molecular oxygen).	140
3.20	Angular flux profile of the oxygen beam when the tungsten filament is at 2800°K (molecular oxygen)	141
3.21	Angular flux profile of the oxygen beam when the tungsten filament is at 2800°K (atomic oxygen).	142
3.22	Relative atomic oxygen flux versus total particle flux at the omegatron orifice, $T(O)=2800^{\circ}K$, $T(O_2)=300^{\circ}K$.	151
3.23	Comparison of the atomic oxygen velocity distribution in the beam with the distribution encountered during a typical rocket flight at normal incidence.	152
4.1	Omegatron envelope with magnet and omegatron cage.	156
4.2	Omegatron cage.	157
4.3	Normalized mass 32 output signals of the quadrupole and the omegatron versus temperature of the tungsten filament at constant source flux.	172
4.4	Atomic oxygen flux dependence of the measured values of the net atom recombination in the omegatron.	175
E.1	Vector diagram for the angular distribution of the particle flux through a knife edge orifice of a moving vehicle.	214

CHAPTER I

INTRODUCTION

The purpose of the present work is to develop a method for a laboratory evaluation of mass spectrometers used for measurements of atomic oxygen in the upper atmosphere. An atomic beam system has been designed with which it is possible to generate a pure oxygen beam of high relative atomic concentration. Oxygen atoms are produced by thermal dissociation of oxygen molecules on a hot tungsten filament. The emitted oxygen atoms and molecules are collimated to form a particle beam. Relative atomic concentrations of more than 70% are obtained over a flux range which simulates atmospheric conditions at about 200 km. The average thermal velocity of the emitted oxygen atoms is close to velocities expected in rocket-borne measurements; that is, the kinetic energy is in the neighborhood of 0.25 eV. The beam is relatively free of contaminants (e.g., water or other additives) which are frequently used to enhance the atomic concentration in the glow discharge technique but are not required in the experiment here reported.

The beam was calibrated using an open ion source quadrupole mass spectrometer and an enclosed ion source omegatron mass spectrometer. The interpretation of the calibration data requires a knowledge of the kinetic temperature of the

beam particles and the ionization cross section ratios for atomic and molecular oxygen. The experimental arrangement permits a reasonably firm determination of the kinetic temperature. The ionization cross sections have been taken from the literature.

The application of the beam to the study of the problem of measurement of atmospheric abundance of atomic oxygen requires an extension to the existing theory of gas kinetics used in relating measured densities to ambient densities. Added to the general complexity of measuring the ambient quantities of chemically stable species are the difficulties involved in taking into account rigorously the interactions of the atomic oxygen with the instrument surfaces. In Chapter II, the physics of direct measurement of neutral atmospheric density is reviewed as a prelude to the extension of the theory to include surface adsorption and recombination.

The final configuration of the atomic oxygen beam system evolved from many iterations of a concept that was adopted after an initial study of existing methods of atomic oxygen generation. A detailed description of the beam system and its development is given in Chapter III. A particularly valuable aspect of the beam system is its ability to produce almost identically the conditions of a rocket measurement of the 100-200 km region of the earth's atmosphere. This makes the system potentially useful for a wide variety of studies pertaining to the measurement of atomic oxygen and to the

effects of surface reactions with atomic oxygen.

The completed beam system has been used to study recombination and absorption phenomena in two flight-type omegatron gauges. The two gauges were identical except that the stainless steel surfaces of one had been chemically gold-plated. Gauges of both types have been flown previously in attempts to measure atmospheric atomic oxygen. The results of the laboratory measurements do not fully satisfy the questions raised by the in-flight measurements, but the preliminary results clearly point the way to further studies of gas-surface interactions using the atomic oxygen beam.

CHAPTER II

THE PROBLEMS OF DIRECT MEASUREMENTS IN THE ATMOSPHERE AND THE NEED FOR A LABORATORY OXYGEN BEAM GENERATOR

2.1 BACKGROUND

The knowledge of the gas density, the gas composition, and the temperature of the upper atmosphere is fundamental to an understanding of the physical processes and the dynamics of the atmosphere. In efforts to obtain this information, many techniques have been employed during the last decade. Mass spectrometers mounted on rockets and satellites have been widely used for neutral particle and ion composition measurements.

The ion and neutral particle composition of the atmosphere changes with altitude because of the earth's gravitational and magnetic fields and the absorption of energy from the sun. Up to altitudes of about 100 km the atmosphere is thoroughly mixed because of turbulence and convection. In this region the composition of the neutral particles does not change significantly. At altitudes above 120 km, diffusion times become sufficiently short so that diffusive equilibrium is maintained. The change in density with altitude for each neutral constituent follows the barometric law

$$n_i(z) = n_i(z_0) \frac{T(z_0)}{T(z)} \exp \left(- \int_{z_0}^z \frac{dz}{H_i} \right), \quad (2.1)$$

where H_i is the scale height

$$H_i = \frac{kT(Z)}{m_i g(Z)} \quad (2.2)$$

$n_i(Z)$ and $n_i(Z_0)$ are the particle densities of the i^{th} constituent at altitude Z and the reference altitude Z_0 ,

$T(Z)$ and $T(Z_0)$ are the corresponding kinetic temperatures, k is Boltzmann's constant (1.3805×10^{-23} J/deg), g is the acceleration of gravity, and m_i is the mass of the particles.

The continuous change of composition results in a relatively larger fraction of light constituents with increasing altitudes. Because of its relatively large photodissociation cross section, molecular oxygen is readily dissociated by the extreme ultraviolet radiation of the sun. At the altitude of about 80 km the atomic oxygen concentration becomes significant. The decreased gas density and the associated decrease of collisions between gas particles lead to large lifetimes of the ionized, the dissociated, and the excited states of the constituents. This is well illustrated by the substantial degree of permanent ionization in the upper atmosphere and by the relatively large amounts of atomic oxygen which becomes the major constituent above 200 km.

If the absolute sensitivity of the mass spectrometer

for all constituents is known, the total mass density can be computed. This parameter can also be determined from satellite drag data. For as yet unknown reasons, the satellite drag data yield continuously higher measurements than those of the mass spectrometers. It has been suggested (von Zahn, 1967) that this discrepancy results from the large uncertainties in the atomic oxygen measurements. A primary objective of the program here described is to remove the major uncertainties.

The proper interpretation of data obtained from rocket- or satellite-borne mass spectrometers presents serious difficulties. The velocities of the rockets or satellites are usually much higher than the characteristic thermal velocities of the ambient gas particles. The measured particle densities are therefore affected by the instrument orientation with respect to the direction of motion. Particles ionized in the ion source of the mass spectrometer are composed of contributions from particles coming directly from the ambient gas and from particles which are reflected from the source surfaces. Since the velocity of the reflected particles is usually much smaller than the velocity of the direct streaming particles and the number of ions produced in the ion source is proportional to the average particle density and not to the particle flux in the ionization region, the main contribution comes from reflected particles. One can take advantage of this fact by enclosing the ion source and connecting it to

the ambient atmosphere via a knife-edge orifice. Particles then collide many times with the walls of the enclosure before they are ionized; therefore, the gas is assumed to be at the temperature of the walls (Dow and Reifman, 1946; Schultz, Spencer, and Reifman, 1948). This technique has found wide application for molecular nitrogen, argon, and helium. Atomic oxygen measurements have been considerably more difficult to obtain by this method. Because of its high chemical activity, atomic oxygen reacts strongly with the instrument-chamber walls, and many of the oxygen atoms are permanently absorbed on the surface, or recombined to molecular oxygen. As a result of these losses, the measured atom concentrations are much lower than the actual atmospheric densities.

Improvements can be obtained by using an open ion source; in this case fewer surface collisions per particle occur but one must deal with more complex gas dynamic conditions, (see, for example, Hedin, Avery, and Tschetter, 1964; Niemann and Kreick, 1966).

In order to account for the loss of oxygen atoms in an enclosed ion source system, the theory relating the ambient particle density to the particle density inside the spectrometer chamber has been extended to include atom recombination on the chamber walls. It is shown in this chapter, if proper care is taken in the choice of surface materials and system geometry, that the atomic recombination can be

accounted for in the data analysis provided a saturation stage is reached so that permanent atomic absorption is negligible.

Many different mass spectrometers have been employed for neutral particle composition measurements. Detailed descriptions of the instruments are given by Townsend (1952), Nier (1960), Schaefer and Nichols (1961), Spencer and Reber (1963), and Niemann and Kennedy (1966). In all mass spectrometers used so far, ions are produced by electron impact with the ionizing electrons obtained from thermionic emitters. However, the design details differ considerably in the various instruments. They are governed by the properties of the mass analyzer section and the experimental conditions, for example, whether the ion source is an open or closed design. The choice of surface materials has also varied considerably. Open and closed stainless steel ion sources have been employed by Nier, Hoffman, Johnson, and Holmes (March 1964) in a magnetic sector spectrometer, by Offerman and von Zahn (1964) in a quadrupole, and by Spencer, Brace, Niemann, Carignan and Taeusch (1965) in omegatron spectrometers. Gold-plated surfaces have been used by Schaefer and Nichols (1964) in a quadrupole mass spectrometer and by Taeusch, Smith, Niemann, Carignan, and Ballance (1967) in an omegatron system. Reber and Harpold (1967) have used an ion source coated with silver oxide to enhance the oxygen atom recombination on the walls so that only molecular oxygen remains in the source chamber.

More recently a quadrupole mass spectrometer with

pure titanium surfaces was employed by Philbrick, Narcisi and Wlodyka (1968). Philbrick, et al. (1968) chose titanium because its oxide has an extremely low atom recombination efficiency.

None of the instruments flown was calibrated in the laboratory for atomic oxygen. The choice of the surface materials was based on recombination data which were obtained under experimental conditions considerably different from those in the space-borne environment. Commonly used techniques for recombination coefficient measurements and large quantities of accumulated data are presented by Kaufman (1961) and Morgan and Schiff (1965). All the data presented were obtained at high gas densities under steady state conditions.

More recently, Myerson (1968) investigated the thermal response of noble metal films to oxygen atom exposure. When exposing the films, which had been previously exposed to oxygen molecules, to a step-function atom flow, Myerson found that the initial response of the film differed considerably from the steady state value. He concluded that an oxidation took place during the initial exposure. Unfortunately the experimental arrangement did not permit him to measure the amount of oxygen absorbed on the film surface.

To simulate the conditions encountered during a rocket or satellite flight accurately, a high velocity and low density atomic and molecular beam system is needed. The

required kinetic energy ranges from approximately 0.25 eV for rocket experiments to 8.0 eV for satellite experiments. Particle beams of this energy are extremely difficult to obtain with any gas and the problem is increasingly complex with atomic oxygen because its chemical activity makes it difficult to produce and to maintain. In contrast to the conditions in the upper atmosphere, atomic concentrations obtained in the laboratory are extremely low (Herzog, 1964, 1968; Narcisi, Schiff, Morgan, and Cohen, 1965). Moreover, no direct method for measuring the atomic concentration at these pressure levels is known. Measurement techniques applicable at high pressures are inadequate because of lack of sensitivity. Indirect methods, for example, detection by ionization gauges or mass spectrometers, involve assumptions which are difficult to verify. In summary, there has been a serious lack of atomic oxygen measurement resources, a lack which it is believed has been substantially reduced by the work here reported.

2.2 EXTENSION OF THE GAS DYNAMIC THEORY TO INCLUDE GAS SURFACE INTERACTIONS WITH APPLICATION TO FLIGHT MEASURE- MENTS OF ATMOSPHERIC ATOMIC OXYGEN

The well-known theory, relating the ambient particle density to the number density inside a chamber which is connected to the atmosphere by an orifice, is in this section extended to include atomic recombination. This extension is necessary for proper interpretation of the atomic oxygen data obtained from the space-borne mass spectrometers and the spectrometer calibration which can be performed on the atomic oxygen beam system described herein. Several simplifications in the derivations have been made. Because of the incomplete knowledge of the detailed surface structure, and because of mathematical complexities, simplifications are, of course, necessary. The derivation is given in two parts: first, systems with uniform surfaces are considered, and second, nonuniform surfaces are included. It is believed the results indicate well the gross behavior of the system.

2.2.1 Recombination of Atoms inside a Chamber with Uniform Surfaces

Only a single gas, atomic oxygen, is considered and the following assumptions are made:

- (1) The chamber has an ideal orifice.
- (2) The mean free path is large compared to the chamber dimensions, so that interparticle

collisions can be neglected.

- (3) The chamber volume is sufficiently large relative to the size of the orifice so that the particle density inside the chamber is uniform.
- (4) The surface has uniform characteristics.
- (5) No diffusion of the atoms into the surface occurs.
- (6) All particles inside the chamber are thermally accommodated to the wall temperature.
- (7) Molecular oxygen does not react in any way with the surface.

Let $n_1(0)$ be the ambient atomic oxygen density, $n_2(0)$ be the atomic oxygen density inside the chamber, and $n_2(O_2)$ be the molecular oxygen density inside the chamber. If the vehicle is moving with a uniform velocity through the atmosphere, the flux into the chamber is given by

$$\phi_1(0) = \frac{1}{4} n_1(0) \bar{v}_1(0) F(s), \quad (2.3)$$

where

$\bar{v}_1(0)$ is the average thermal velocity of the ambient atoms

$$\bar{v}_1(0) = \sqrt{\frac{8kT_1(0)}{\pi m(0)}}, \quad (2.4)$$

$m(0)$ is the mass of the oxygen atom,

k is Boltzmann's constant,

$T_1(0)$ is the ambient gas temperature,

$F(s)$ is the velocity correction factor to the thermal transpiration relation (Schultz, et al., 1948),

$$F(s) = e^{-s^2} + \sqrt{\pi}s[1 + \operatorname{erf}(s)], \quad (2.5)$$

where
$$s = \frac{\vec{u} \cdot \vec{n}}{v_{p1}(0)} \quad (2.6)$$

\vec{u} is the rocket velocity,

\vec{n} is the normal vector of the orifice, and

$v_{p1}(0)$ is the most probable thermal velocity of the ambient oxygen.

This velocity correction factor results from the fact that the system is in translational motion with respect to the ambient atmosphere. The flux from the chamber to the ambient atmosphere is simply the sum of fluxes of the recombined and the remaining atomic oxygen.

$$\phi_2 = \phi_2(0) + \phi_2(O_2), \quad (2.7)$$

where $\phi_2(0)$ and $\phi_2(O_2)$ symbolize the atomic and molecular oxygen fluxes. By assumption (6) and by simple kinetic theory,

$$\phi_2(0) = \frac{1}{4}n_2(0)\bar{v}_2(0), \quad (2.8)$$

$$\phi_2(O_2) = \frac{1}{4}n_2(O_2)\bar{v}_2(O_2), \quad (2.9)$$

with

$$\bar{v}_2(O) = \sqrt{\frac{8kT_2}{\pi m(O)}} , \quad (2.10)$$

$$\bar{v}_2(O_2) = \sqrt{\frac{8kT_2}{\pi m(O_2)}} , \quad (2.11)$$

T_2 is the temperature of the chamber wall, and $m(O_2)$ is the mass of the oxygen molecule.

Under steady state conditions and assumption (5), the flux into the chamber must equal the flux leaving the chamber.

Therefore we have

$$\phi_1(O) = \phi_2(O) + 2\phi_2(O_2) . \quad (2.12)$$

The objective is now to express the outgoing atomic and molecular oxygen flux in terms of the recombination coefficient and the chamber geometry. The geometry of the chamber determines how many collisions a particle makes with the wall of the chamber before it leaves through the orifice, and the number of wall collisions determine the relative concentrations of atomic and molecular oxygen inside the chamber.

Let p_i be the probability of escape of a particle through the orifice after the i^{th} bounce from the chamber wall. If we consider a sample of particles at a particular instant and follow its motion and compute the fraction which leaves through the orifice after each bounce and the fraction which recombines after each bounce, we can write

for the atomic oxygen flux escaping after the first bounce,

$$\Delta_1 \phi_2(0) = \bar{\alpha} \phi_1(0) p_1 (1-\gamma), \quad (2.13)$$

where $\bar{\alpha}$ is a real number smaller than unity, denoting that only a small test sample is considered, and γ is the recombination coefficient. The recombination coefficient, γ , is the ratio of the molecular oxygen flux leaving the surface to the atomic oxygen flux which approaches the surface. The fraction of the atomic oxygen flux which is leaving through the orifice after the second bounce is given by

$$\Delta_2 \phi_2(0) = \frac{1}{p_1} (1-p_1) \Delta_1 \phi_2(0) p_2 (1-\gamma), \quad (2.14)$$

and after the i^{th} bounce

$$\Delta_i \phi_2(0) = \frac{1}{p_{i-1}} (1-p_{i-1}) \Delta_{i-1} \phi_2(0) p_i (1-\gamma). \quad (2.15)$$

By adding all terms, we have

$$\sum_{i=1}^{\infty} \Delta_i \phi_2(0) = \bar{\alpha} \phi_1(0)$$

$$[p_1 (1-\gamma) + \dots + (1-p_1) (1-p_2) \dots (1-p_{i-1}) (1-p_i) (1-\gamma)^i + \dots], \quad (2.16)$$

or when written in a more compact form

$$\sum_{i=1}^{\infty} \Delta_i \phi_2(0) = \bar{\alpha} \phi_1(0) \sum_{i=1}^{\infty} [p_i (1-\gamma)^i \prod_{j=1}^i (1-p_{j-1})]. \quad (2.17)$$

The choice of $\bar{\alpha}$ is arbitrary. Results similar to the one above can be obtained by considering a different fraction of particles which may or may not contain $\bar{\alpha}$. By choosing all fractions so that they are independent of each other and by adding them, we obtain the total atomic oxygen flux which leaves the chamber through the orifice. Thus we have

$$\phi_2(O) = \phi_1(O) \sum_{i=1}^{\infty} [p_i (1-\gamma)^i \prod_{j=1}^i (1-p_{j-1})], \quad (2.18)$$

and with Equation (2.12)

$$\phi_2(O_2) = \frac{1}{2} \phi_1(O) \left\{ 1 - \sum_{i=1}^{\infty} [p_i (1-\gamma)^i \prod_{j=1}^i (1-p_{j-1})] \right\}. \quad (2.19)$$

The problem is solved provided that we can determine the escape probabilities and the recombination coefficient. The recombination coefficient depends on the surface parameters which characterize the adsorption and evaporation of atoms and molecules. The escape probability is a function of the detailed chamber geometry and the nature of the particle reflections and emission from the surface. It can be found only with a detailed knowledge of the particle collision distribution in the chamber. If we make the simplifying assumption that the escape probability is independent of the number of bounces, we have

$$p_1 = p_2 \dots p_i \equiv p. \quad (2.20)$$

A spherical chamber with diffusively reflecting walls (cosine law reflection) is the closest approximation to a system which satisfies this assumption. Equations (2.18) and (2.19) can now be evaluated easily.

$$\phi_2(0) = \phi_1(0) \sum_{i=1}^{\infty} p(1-p)^{i-1} (1-\gamma)^i = \phi_1(0) \frac{1}{1 + \frac{\gamma}{p(1-\gamma)}}, \quad (2.21)$$

and

$$\phi_2(0_2) = \frac{1}{2} \phi_1(0) \left[1 - \frac{1}{1 + \frac{\gamma}{p(1-\gamma)}} \right] = \frac{1}{2} \phi_1(0) \frac{1}{1 + \frac{\gamma}{p(1-\gamma)}}. \quad (2.22)$$

The probability of escape after one bounce can be estimated by considering the time response of the chamber. If at a given time, a large number of particles n_0 are in the chamber, and these particles alone are considered, then the particle density n_0 will decrease exponentially with time

$$n(t) = n_0 \exp(-t/\bar{\tau}), \quad (2.23)$$

where $\bar{\tau}$ is the chamber time constant. The time constant $\bar{\tau}$ is the ratio of the volume of the chamber to the gas conductance of the orifice. For an ideal system

$$\bar{\tau} = V / (\frac{1}{4} S_0 \bar{v}) \quad (2.24)$$

where

V is the volume of the chamber,
 $\frac{1}{4}S_o\bar{v}$ is the conductance of the orifice,
 S_o is the orifice area, and
 \bar{v} is the average velocity of the gas particles.

If t_o is the average time between wall collisions, then the decrease in the particle density after each bounce is given by

$$\Delta n(t) = n(t) - n(t+t_o). \quad (2.25)$$

After the i^{th} bounce

$$\begin{aligned}
 \Delta n_i &= n\left((i-1)t_o\right) - n(it_o) \\
 &= n_o \left[\exp\left(-\frac{(i-1)t_o}{\tau}\right) - \exp\left(-i\frac{t_o}{\tau}\right) \right] \\
 &= n_o \left[1 - \exp\left(-\frac{t_o}{\tau}\right) \right] \exp\left(-(i-1)\frac{t_o}{\tau}\right).
 \end{aligned} \quad (2.26)$$

Considering now the i^{th} term of Equation (2.21) and disregarding recombination, since p is a function of the chamber geometry only, we have

$$\Delta_i \phi_2 = \phi_1 p(1-p)^{i-1}. \quad (2.27)$$

The steady state condition requires that

$$\phi_1 = \phi_2 = \frac{1}{4}n_o\bar{v}, \quad (2.28)$$

and

$$\Delta_i \phi_2 = \frac{1}{4} \Delta n_i \bar{v}. \quad (2.29)$$

Therefore we can write

$$\Delta n_i = n_o p (1-p)^{i-1}. \quad (2.30)$$

Comparing Equation (2.30) with Equation (2.26), we have

$$p(1-p)^{i-1} = \left[1 - \exp\left(-\frac{t_o}{\bar{\tau}}\right) \right] \exp\left(-(i-1)\frac{t_o}{\bar{\tau}}\right), \quad (2.31)$$

from which we find that

$$p = 1 - \exp\left(-\frac{t_o}{\bar{\tau}}\right). \quad (2.32)$$

As mentioned above in Equation (2.24)

$$\bar{\tau} = \frac{V}{\frac{1}{4} S_o \bar{v}}, \quad (2.33)$$

and the quantity t_o can be approximated by considering a characteristic length $\bar{\ell}$ of the chamber and the average velocity \bar{v} of the gas, thus

$$t_o = \frac{\bar{\ell}}{\bar{v}}. \quad (2.34)$$

Use of these selections for t_o and $\bar{\tau}$ permit expressing Equation (2.32) as

$$p = 1 - \exp\left(-\frac{\bar{\ell} S_o}{4\bar{v}}\right), \quad (2.35)$$

which becomes for small $t_o/\bar{\tau}$

$$p \approx \frac{\bar{\ell} S_O}{4V}. \quad (2.36)$$

It is useful to note that this probability p is strictly a function of the chamber geometry and independent of the temperature of the gas, since the average velocity \bar{v} is cancelled in the $t_O/\bar{\tau}$ ratio.

For typical apparatus of the kind being considered, the ratio V/S_O of volume to orifice area is about 1.5 m, and the characteristic length is about 0.03 m. Substituting these values into Equation (2.36) yielded a probability p of

$$p = \frac{0.03}{4 \times 1.5} = 5. \times 10^{-3}. \quad (2.37)$$

It is useful, in consideration of the various properties of the chamber, to have in mind separately the average time t_O between wall collisions and the time constant of the chamber for the particular gas of interest being atomic oxygen and a typical chamber temperature which might well be 300°K. At 300°K, Equation (2.10) for atomic oxygen gives

$$\bar{v}_2(0) = 620. \text{ m/sec.} \quad (2.38)$$

Substituting the values for the volume to orifice ratio V/S_O and the average velocity $\bar{v}_2(0)$ into Equation (2.33), we obtain a typical chamber time constant of

$$\bar{\tau} = \frac{1.5}{4 \times 6.20} \approx 0.01 \text{ sec} \quad (2.39)$$

and the average time between collisions t_0 is obtained from Equation 2.34

$$t_0 = \frac{0.03}{620.} = 4.83 \times 10^{-5} \approx 5. \times 10^{-5} \text{ sec.} \quad (2.40)$$

The value of γ is determined by the surface processes. Its dependence on the particle flux and the surface parameters is discussed in Section 2.3.

As was mentioned above, the quantity of interest is the ambient particle density and the quantity which is measured is the particle density inside the chamber. Therefore, the flux relations shown in Equation (2.21) and Equation (2.22) have to be converted to density relations. Substituting Equations (2.3) and (2.8) into Equation (2.21) and defining

$$\epsilon(\gamma) = \frac{\gamma}{p(1-\gamma)}, \quad (2.41)$$

we have

$$\begin{aligned} n_1(0) &= n_2(0) \frac{\bar{v}_2(0)}{\bar{v}_1(0)} \frac{1}{F(s)} [1 + \epsilon(\gamma)] \\ &= n_2(0) \sqrt{\frac{T_2}{T_1}} \frac{1}{F(s)} [1 + \epsilon(\gamma)] \end{aligned} \quad (2.42)$$

where $F(s)$ is as defined by Equation (2.5). Similarly, by substituting Equations (2.3) and (2.9) into Equation (2.22) we obtain

$$n_1(0) = \sqrt{2} n_2(O_2) \sqrt{\frac{T_2}{T_1(0)}} \frac{1}{F(s)} \left[1 + \frac{1}{\epsilon(\gamma)} \right]. \quad (2.43)$$

Equation (2.42) shows that the effect of recombination requires the addition of a corrective term to the equation for noninteracting gases which accounts for the loss of oxygen atoms. If the exact value of $\epsilon(\gamma)$ is known, the ambient atomic oxygen density can, at least in principle, be determined in the same manner as, for example, the ambient molecular nitrogen density.

If the values of $n_2(0)$ and $n_2(O_2)$ can be measured simultaneously, or at close time intervals, the ambient atomic oxygen density $n_1(0)$ can be obtained by solving Equations (2.42) and (2.43) simultaneously, or by substituting Equations (2.3), (2.8) and (2.9) into Equation (2.12) and solving for the ambient oxygen density. Thus we have

$$n_1(0) = \sqrt{\frac{T_2}{T_1(0)}} \frac{1}{F(s)} \left[n_2(0) + \sqrt{2} n_2(O_2) \right]. \quad (2.44)$$

There would, of course, be an advantage in being able to determine the ambient oxygen density by measuring only $n_2(0)$. This requires a knowledge of $1 + \epsilon(\gamma)$ where $\epsilon(\gamma)$ is given by Equation (2.41). Note that

$$1 + \epsilon(\gamma) = 1 + \frac{1}{p} \frac{\gamma}{1-\gamma}. \quad (2.45)$$

The value of p can be reasonably well estimated as illustrated by Equations (2.35) and (2.36). It is entirely a property of the geometry of the chamber, which is known and can perhaps be subject to design considerations for optimizing the accuracy with which p is known. For a sufficiently regular chamber geometry, a spherical chamber with a small knife-edge orifice for example, the accuracy to which p can be determined will increase as the value of p decreases because the assumption of finding the gas in equilibrium with the walls of the chamber is best satisfied if the chamber time constant $\bar{\tau}$ is large. A small value of p implies, however, a large average number of wall collisions of particles in the chamber and therefore a large effective atomic recombination.

If a wall material for the chamber is used that makes the recombination coefficient γ much smaller than p for all flux levels which are of interest, then the correction term $\epsilon(\gamma)$ becomes much smaller than unity and it can be neglected.

If however, γ is relatively large compared to unity, then $\epsilon(\gamma)$ will assume a very large value and it is very sensitive to variations in the value of γ . In that case it is of advantage to use Equation (2.43) for the determination of the ambient atomic oxygen density provided the complication of a substantial direct inward flux of molecular oxygen from the atmosphere can either be avoided or accounted for separately.

In the case that both γ and p are much smaller than

unity but their values are of equal magnitude Equation (2.45) becomes approximately

$$1 + \epsilon(\gamma) \approx 1 + \frac{\gamma}{p}. \quad (2.46)$$

A good knowledge of the value of γ and p is required regardless of whether Equation (2.42) or Equation (2.43) is used for the determination of $n_1(0)$.

If an arrangement can be provided that makes γ independent of flux and time, perhaps for the attainment of a saturation condition on the surface, $\epsilon(\gamma)$ will also be independent of flux and time, because p has been shown to be only a property of the chamber geometry. In this case a knowledge of the atomic oxygen scale height, determined by comparison of the $n_2(0)$ measurements at increasing or decreasing altitudes, permits the determination of $n_1(0)$ from Equation (2.42) and Equation (2.43) above because $\epsilon(\gamma)$ can be eliminated between the measurement at various altitudes. At altitude ranges below 200 km the atmospheric molecular oxygen concentration is still significant. There the mass 32 ion current is the sum of the contribution of atmospheric molecular oxygen and internally recombined atomic oxygen. However, as long as the measurements are carried out at a high enough altitude, so that diffusive separation is maintained, the atmospheric and internally recombined molecular oxygen contribution can be separated if the scale heights are known.

In summary, it has been shown that with instrumentation

provided which will with reasonable accuracy directly measure the $n_2(0)$ of Equation (2.42), it will be possible to determine the ambient density $n_1(0)$, and more especially so if in the same instrument it is possible to measure simultaneously, or at short time intervals, $n_2(0)$ and $n_2(O_2)$, permitting simultaneous use of Equations (2.42) and (2.43). In this latter case there can also be made a useful experimental determination of $1 + \epsilon(\gamma)$ and so of γ .

2.2.2 Recombination of Atomic Oxygen Inside a Chamber with Nonuniform Surfaces

The discussion in the previous section is based on the assumption that the chamber surface exhibits a uniform average behavior. This assumption is not always realistic. Frequently several different materials are used for the spectrometer electrodes in order to simplify the construction or to improve the instrument performance. Although the problem could perhaps be overcome by the surface plating of all metal surfaces with suitable materials, those used for electrical insulation cannot be avoided. In this section chambers with nonuniform surfaces are described. The chamber surface includes patches of materials with different characteristics. The size of the patches is assumed to be large on the microscopic scale so that each patch forms a homogeneous surface with particular properties and the boundary lines between the adjacent patches are sufficiently narrow so that junction effects can be neglected.

We let γ_i be the recombination coefficient of the i^{th} surface patch, where i ranges from 1 to ℓ , the total number of distinct patches. The probability of escape of a particle from the i^{th} patch through the orifice is p_{i0} . It is assumed to be independent of the number of collisions made previously. The probability that a particle which is emitted from the i^{th} surface patch collides with the j^{th} patch is p_{ij} , and the probability that a particle which enters through the orifice and collides with the j^{th} surface patch is p_{0j} . The fraction of the incoming atomic oxygen flux which leaves through the orifice after the first bounce is then given by

$$\Delta_1 \phi_2(0) = \phi_1(0)$$

$$[p_{10}p_{01}(1-\gamma_1) + p_{20}p_{02}(1-\gamma_2) + \dots + p_{\ell 0}p_{0\ell}(1-\gamma_\ell)], \quad (2.47)$$

where the first term on the right side of Equation (2.47) is the fraction leaving from surface element 1, the second term is the fraction leaving from surface element 2, etc. After the second bounce,

$$\Delta_2 \phi_2(0) = \phi_1(0)$$

$$\begin{aligned} & \{ (1-p_{10})p_{01}(1-\gamma_1)[p_{10}p_{11}(1-\gamma_1) + p_{20}p_{12}(1-\gamma_2) + \dots + \\ & p_{\ell 0}p_{1\ell}(1-\gamma_\ell)] + (1-p_{20})p_{02}(1-\gamma_2)[p_{10}p_{21}(1-\gamma_1) + \end{aligned}$$

$$\begin{aligned}
& p_{20}p_{22}(1-\gamma_2) + \dots + p_{\ell 0}p_{2\ell}(1-\gamma_\ell)] + \\
& \vdots \\
& (1-p_{\ell 0})p_{0\ell}(1-\gamma_\ell)[p_{10}p_{\ell 1}(1-\gamma_1) + p_{20}p_{\ell 2}(1-\gamma_2) + \dots + \\
& p_{\ell 0}p_{\ell \ell}(1-\gamma_\ell)]], \tag{2.48}
\end{aligned}$$

and after the third bounce,

$$\begin{aligned}
& \Delta_3\phi_2(0) = \phi_1(0) \\
& \{ (1-p_{10})(1-\gamma_1)[(1-p_{10})p_{01}p_{11}(1-\gamma_1) + (1-p_{20})p_{02}p_{21}(1-\gamma_2) + \\
& \dots + (1-p_{\ell 0})p_{0\ell}p_{\ell 1}(1-\gamma_\ell)] [p_{10}p_{11}(1-\gamma_1) + p_{20}p_{12}(1-\gamma_2) + \\
& \dots + p_{\ell 0}p_{1\ell}(1-\gamma_\ell)] + (1-p_{20})(1-\gamma_2)[(1-p_{10})p_{01}p_{12}(1-\gamma_1) + \\
& (1-p_{20})p_{02}p_{22}(1-\gamma_2) + \dots + (1-p_{\ell 0})p_{0\ell}p_{\ell 2}(1-\gamma_\ell)] [p_{10}p_{21} \\
& (1-\gamma_1) + p_{20}p_{22}(1-\gamma_2) + \dots + p_{\ell 0}p_{2\ell}(1-\gamma_\ell)] + \\
& \vdots \\
& (1-p_{\ell 0})(1-\gamma_\ell)[(1-p_{10})p_{01}p_{1\ell}(1-\gamma_1) + (1-p_{20})p_{02}p_{2\ell}(1-\gamma_2) + \\
& \dots + (1-p_{\ell 0})p_{0\ell}p_{\ell \ell}(1-\gamma_\ell)] [p_{10}p_{\ell 1}(1-\gamma_1) + p_{20}p_{\ell 2}(1-\gamma_2) + \\
& \dots + p_{\ell 0}p_{\ell \ell}(1-\gamma_\ell)] \}. \tag{2.49}
\end{aligned}$$

These expressions can be written more compactly.

$$\Delta_1\phi_2(0) = \phi_1(0) \sum_{i=1}^{\ell} p_{0i}p_{i0}(1-\gamma_i) \tag{2.50}$$

$$\Delta_2 \phi_2(O) = \phi_1(O) \sum_{j=1}^{\ell} \sum_{i=1}^{\ell} p_{oj} (1-p_{jo}) (1-\gamma_j) p_{ji} p_{io} (1-\gamma_i) \quad (2.51)$$

$$\Delta_3 \phi_2(O) = \phi_1(O) \sum_{j'=1}^{\ell} \sum_{j=1}^{\ell} \sum_{i=1}^{\ell} p_{oj'} (1-p_{j'o}) (1-\gamma_{j'}) p_{j'j} (1-p_{jo}) (1-\gamma_j) p_{ji} p_{io} (1-\gamma_i). \quad (2.52)$$

If expressed in matrix notation,

$$\Delta_1 \phi_2(O) = \phi_1(O) [p_o] [p(1-\gamma)] \quad (2.53)$$

$$\Delta_1 \phi_2(O) = \phi_1(O) [p_o] [(1-p)(1-\gamma)] [p] [p(1-\gamma)] \quad (2.54)$$

$$\Delta_3 \phi_2(O) = \phi_1(O) [p_o] \left([(1-p)(1-\gamma)] [p] \right)^2 [p(1-\gamma)] \quad (2.55)$$

$$\Delta_i \phi_2(O) = \phi_1(O) [p_o] \left([(1-p)(1-\gamma)] [p] \right)^{i-1} [p(1-\gamma)], \quad (2.56)$$

where $[p_o]$ is a row matrix with ℓ elements $p_{o1}, p_{o2} \dots p_{o\ell}$, $[p]$ is a square matrix with ℓ^2 elements p_{ij} , $[(1-p)(1-\gamma)]$ is a diagonal matrix with ℓ elements $(1-p_{io})(1-\gamma_i)$, and $[p(1-\gamma)]$ is a column matrix with ℓ elements $p_{io}(1-\gamma_i)$. The total atomic oxygen flux leaving through the orifice is obtained by adding all fractions,

$$\phi_2(O) = \sum_{i=1}^{\infty} \Delta_i \phi_2 = \phi_1(O) \sum_{i=1}^{\infty} [p_o] \left([(1-p)(1-\gamma)] [p] \right)^{i-1} [p(1-\gamma)], \quad (2.57)$$

and after summing the series on the right side of Equation (2.57),

$$\phi_2(0) = \phi_1(0) [p_o] \left([U] - [(1-p)(1-\gamma)] [p] \right)^{-1} [p(1-\gamma)], \quad (2.58)$$

where $[U]$ is the unit matrix. After rearranging we have

$$\phi_2(0) = \phi_1(0) [p_o] \left(\left[\frac{1}{(1-p)(1-\gamma)} \right] - [p] \right)^{-1} \left[\frac{p}{1-p} \right], \quad (2.59)$$

where $\left[\frac{1}{(1-p)(1-\gamma)} \right]$ is a diagonal matrix with ℓ elements with the i^{th} element given by $\frac{1}{(1-p_{io})(1-\gamma_i)}$ and $\left[\frac{p}{1-p} \right]$ is a column matrix with ℓ elements with the i^{th} element defined as $\frac{p_{io}}{1-p_{io}}$.

The determination of the escape and of the collision probabilities is a complicated procedure. In principle they can be computed by considering the detailed geometry of the chamber, the surface flux distribution, and the nature of the reflection (i.e., specular or diffusive reflection). In particular, the escape probability from the i^{th} surface patch is obtained by computing the ratio of the particle flow which passes through the orifice to the total flow emitted from the i^{th} element. Similarly, the collision probability p_{ij} is obtained by computing the fraction of the particle flow emitted from the i^{th} surface element which collides with the j^{th} element. Since free molecular flow conditions are assumed, the probabilities can be different from zero only for surface elements which are in direct view of each other. The general expressions for these probabilities are obtained by following the development of DeMarcus (1965).

By referring to Figure 2.1 and by assuming diffusive reflection on the surface, the contribution of atoms leaving a surface element of the i^{th} patch, dS_i , to the flow on the surface element dS_j on the j^{th} patch is given by

$$d(\phi_{ij} dS_i) = \frac{\phi_i dS_i}{\pi} \cos\beta_i \frac{dS_j \cos\beta_j}{r_{ij}^2}, \quad (2.60)$$

where ϕ_{ij} is the surface flux on the j^{th} surface patch which is originating from the i^{th} patch. From the i^{th} patch, ϕ_i is the emitted flux. Integrating both sides with respect to dS_i and dS_j over the patch areas S_i and S_j , we obtain the flow from patch i to patch j .

$$\Psi_{ij} = \int_{S_j} \phi_{ij} dS_j = \frac{1}{\pi} \int_{S_j} dS_j \int_{S_i} dS_i \frac{\phi_i \cos\beta_i \cos\beta_j}{r_{ij}^2}. \quad (2.61)$$

The total flow from the i^{th} patch is

$$\Psi_i = \int_{S_i} \phi_i dS_i, \quad (2.62)$$

and therefore

$$p_{ij} = \frac{\Psi_{ij}}{\Psi_i} = \frac{1}{\Psi_i} \frac{1}{\pi} \int_{S_j} dS_j \int_{S_i} dS_i \frac{\phi_i \cos\beta_i \cos\beta_j}{r_{ij}^2}. \quad (2.63)$$

If the surface flux ϕ_i is uniform, the probability becomes a function of the geometry only.

$$p_{ij} = \frac{1}{\pi} \frac{1}{S_i} \int_{S_j} dS_j \int_{S_i} dS_i \frac{\cos\beta_i \cos\beta_j}{r_{ij}^2}. \quad (2.64)$$

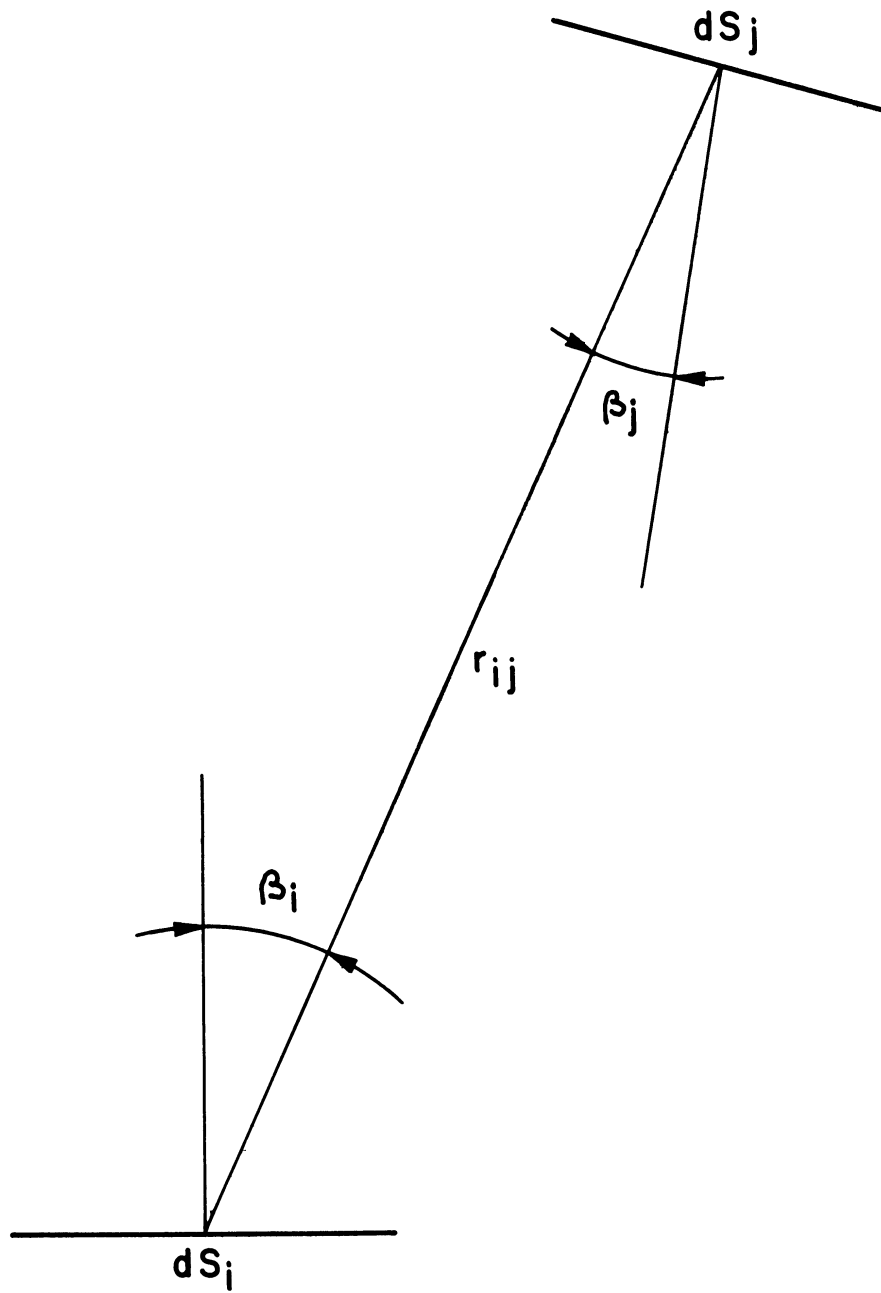


Figure 2.1 Geometric diagram of two surface elements of a chamber with nonuniform surfaces.

Similarly, the escape probability is

$$p_{io} = \frac{1}{\pi} \frac{1}{S_i} \int_{S_o} dS_o \int_{S_i} dS_i \frac{\cos \beta_i \cos \beta_o}{r_{io}^2}. \quad (2.65)$$

The subscript o denotes the orifice area.

2.3 SIMPLE SURFACE PROCESSES

In order to find the surface parameters which were used in the previous discussion, a more detailed consideration has to be given to the processes involved in the collision and the reactions of gases with metal and metal oxide surfaces. Many studies of surface reaction have been made and several theories describing adsorption and recombination have been proposed. Treatments of the problem on a quantum mechanical level are the most basic approach. However, because of the extreme complexity of the problem, only very simple systems can be treated and then only approximately. A detailed knowledge of the surface structure and of the potential distribution on the surface is required.

The surfaces employed in the mass spectrometers and ionization gauges for atmospheric measurements are amorphous and their history is uncertain. Before they come in contact with atomic oxygen, they are exposed to ambient air and have gone through several cleaning processes. The instruments are, in the final preparation, processed under ultrahigh vacuum conditions and the final cleaning usually results from a bakeout at 400°C wherein the surfaces are still partially covered with gases such as N_2 , O_2 , and water vapor. This is apparent when the temperature is raised and an additional gas release can be observed. Although these engineering surfaces differ significantly from the relatively well-defined crystal surfaces, it is expected that certain simple concepts of adsorption and evaporation can be applied in

order to evaluate the general behavior of these surfaces. Discussions of simple gas-surface interaction phenomena involving gases composed of atoms and diatomic molecules have been given by Ehrlich (1959) and Brennan (1964). Their arguments are adapted here.

The important surface processes which require consideration are atomic recombination and molecular dissociation. Both processes are closely dependent on the adsorption and evaporation characteristics of the gases on the surface. The effect of atomic recombination is a result of a competition between atomic condensation on one side and atomic reevaporation and/or recombination on the other. The recombination of atoms can occur in two ways. Atoms from the incoming gas may collide with atoms already adsorbed on the surface and recombine, or adsorbed atoms may migrate over the surface until they collide and recombine. In both cases the surface must absorb energy to prevent the atoms from separating again. Thus not every encounter of two atoms will result in recombination.

Similarly, effective molecular dissociation results from the competing processes of molecular condensation and subsequent dissociation and reevaporation of atoms, or surface recombination and evaporation of the molecules.

Ehrlich's discussion is based on thermodynamic concepts. Consideration of the detailed mechanism of the atomic or molecular binding to the surface atoms is given only as a plausibility description. The different cases of electronic

interaction in the adsorption processes are distinguished only by their different binding energies, characterized by the potential energy curves. The curve relating the potential energy of an atom or molecule to its distance from the surface usually shows a shallow minimum which causes physical adsorption and a deep minimum which causes chemisorption. Potential energy curves for a molecule of a diatomic gas are shown in Figure 2.2.

As the molecule approaches the surface from a large distance, it experiences a potential due only to physical forces between the surface and the molecule (curve a-a, Figure 2.2). If only these forces are present, the molecule will either be trapped in the shallow potential well or be reflected, depending on its kinetic energy and the energy transfer efficiency of the surface. However, when the molecule moves closer to the surface, the chemical forces between the individual atoms of the molecule and the atoms of the surface become more effective, developing a deep potential well (curve b-b, Figure 2.2), where two energetically independent atoms, initially separated by the same geometric distance as the atoms in the molecule, are considered.

At the crossover point c of both curves a-a and b-b, the two electronic states of the system are equal. This degeneracy is usually not allowed and the curves split, leaving the curve described by the solid line to be the physically realistic curve to which the incoming molecule responds. Thus, when the molecule approaches the surface,

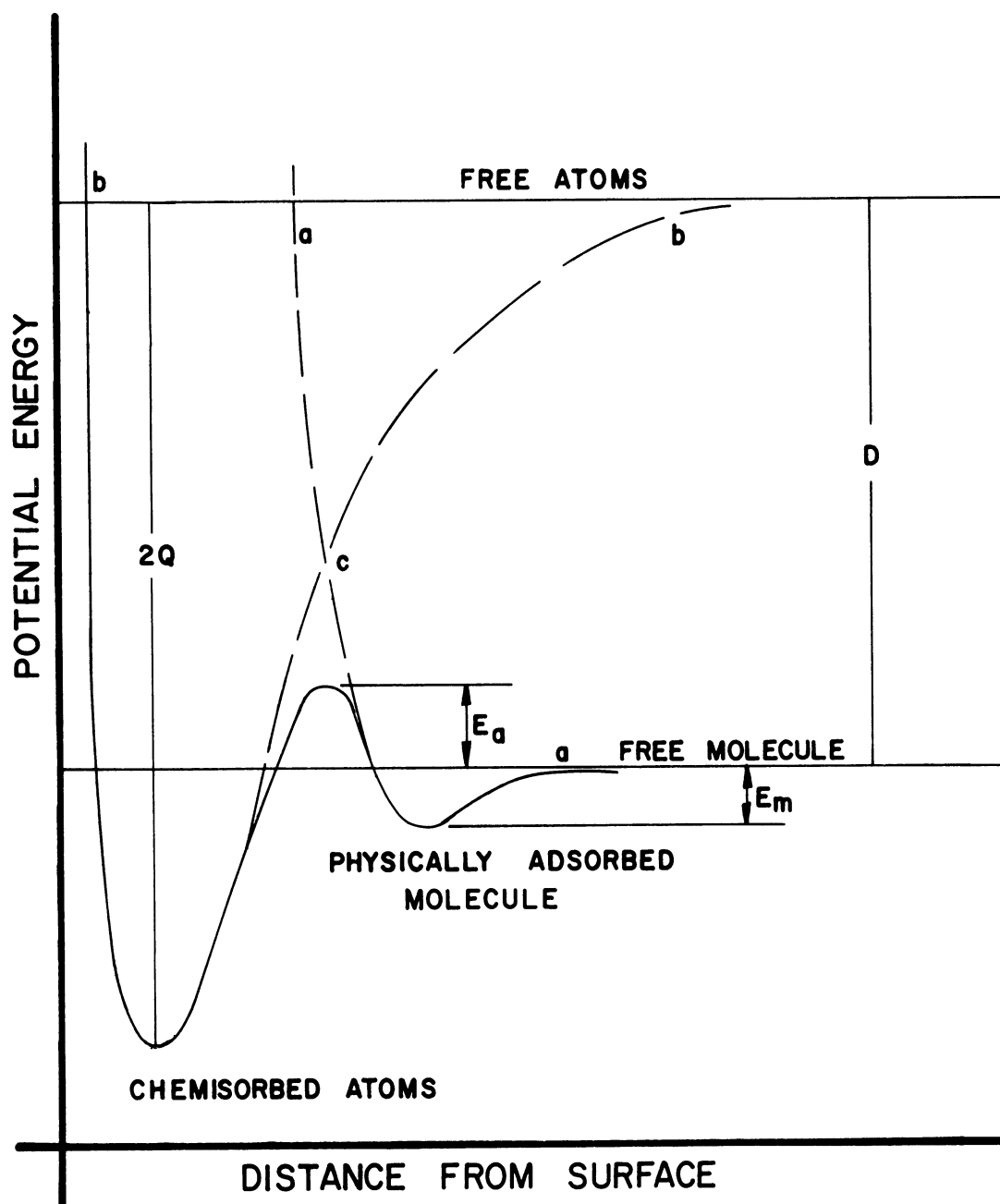


Figure 2.2 Potential energy curve for chemisorption of a diatomic molecule (Ehrlich, 1959).

its intermolecular distance will change little until it passes point c of the solid potential curve. At this point the interaction forces of surface atoms with the individual atoms of the molecule become stronger than the intermolecular forces and can cause a complete split of the molecule. The relative depth of the potential well of curves a-a and b-b and the relative separation of the minima determine whether there is an activation energy required for chemisorption and therefore for dissociation. Based on this concept, there is no activation energy for the adsorption of atoms. It has been concluded from adsorption measurements of oxygen on metal surfaces that the number of available adsorption sites is comparable with the number of lattice sites on the surface (Ehrlich, 1959). The interatomic spacing of most metal crystals is considerably larger than that of diatomic molecules, however. For example, the interatomic spacings for O_2 and N_2 are 1.20 \AA and 1.09 \AA where the interatomic spacing for tungsten is 2.73 \AA and for gold, 2.88 \AA (Ehrlich, 1959). Only one of the atoms of an oxygen molecule placed on such a surface interacts to form a bond strength equivalent to the equilibrium value of an isolated oxygen atom. The other atom is placed between two sites at which the interaction is considerably weaker. The exact position of the second atom with respect to the adjacent adsorption site may necessitate various values of activation energies to move the atom completely to the adjacent site. Maximum interaction between the adsorption sites and both atoms of

the molecule occurs only if the interatomic spacing coincides with the lattice spacing or if the molecule is put into a higher vibrational state. An extremely simplified graphical illustration of the concept is shown in Figure 2.3.

The potential energy near the surface along some axis parallel to the surface is indicated by the solid oscillating line. The nonuniform surface is characterized by the irregular fluctuations. The energy level of the free atoms and molecules, used as a reference level, is also indicated. The illustration indicates that on the heterogeneous surface the heats of adsorption and the activation energy for dissociation and/or migration on the surface vary locally. As a result, adsorption and surface diffusion vary from point to point on the surface. Thus we may find sites where at a particular temperature the adsorption is localized, while at the same temperature on other sites the adsorption will be mobile, producing favorable conditions for surface recombination.

The situation is similar on insulating or semiconducting surfaces. In general, it is assumed that adsorption sites are farther separated on semiconductor surfaces than on metal surfaces. This separation would reduce surface recombination provided that the potential wells have sufficient depth. At the same time dissociative adsorption requires a large activation energy. Thus the efficiency of thermal dissociation of oxygen on hot metals or semiconductors (ThO_2 , for example) may not be very different since high dissociation rates are compensated by high recombination

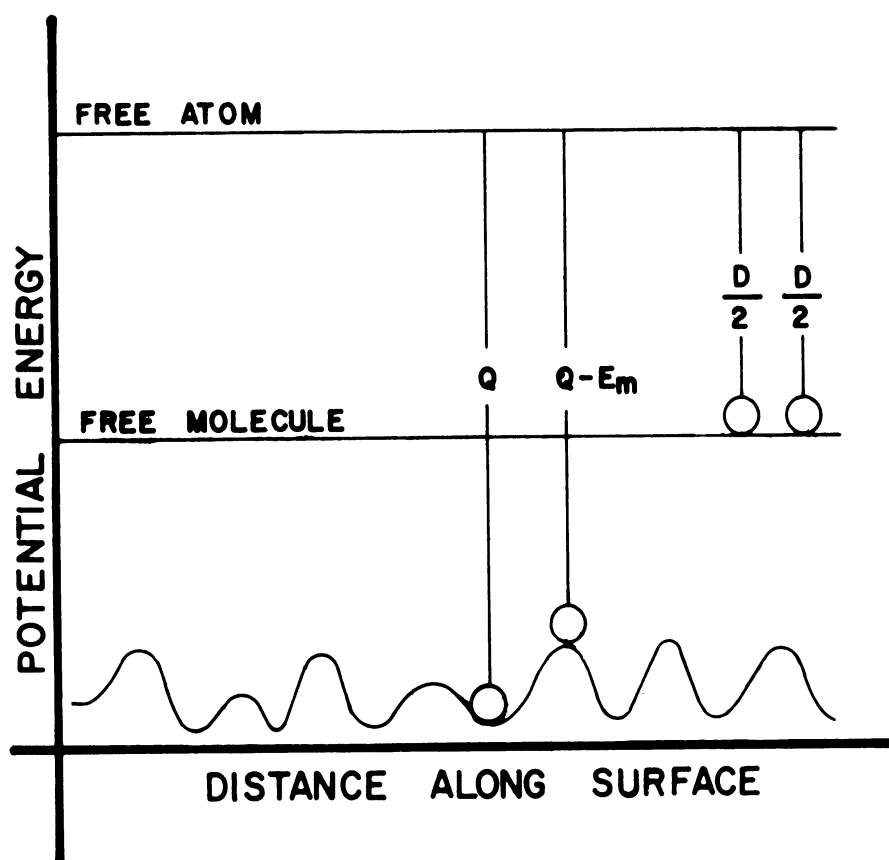


Figure 2.3 Potential energy diagram for an activated complex in chemisorption on a nonuniform surface.

rates on metal surfaces and vice versa on semiconducting surfaces. Considering atom recombination on the surface at room temperature, one would expect a low recombination efficiency for nonmetals because small surface recombination leaves only direct recombination as a result of a collision between a gas and an adsorbed atom. It is also expected that the energy transfer on nonmetals is poorer than on metals which further reduces the efficiency of atomic recombination (Ehrlich, 1959).

Based on thermodynamic arguments, the probability of adsorption, the rate of evaporation, and the recombination coefficient can be expressed in terms of the surface parameters, such as heat of adsorption, activation energies for adsorption and recombination, and number of available adsorption sites. The probability of adsorption can be written as

$$a = a_o \exp \left(- \frac{E_a}{RT} \right) \quad (2.66)$$

where

a_o is the probability that an atom or molecule is adsorbed if it has sufficient energy and when it strikes an empty site,

E_a is the activation energy of adsorption; for atomic oxygen adsorption E_a is assumed to be zero,

R is the universal gas constant (8.314×10^7 erg/g mole $^{\circ}$ K), and

T is the absolute temperature.

Similarly the rate of evaporation b is given by

$$b = b_o \exp \left(- \frac{E_a + Q}{RT} \right), \quad (2.67)$$

where

b_o is a constant to be determined, and

Q is the heat of adsorption.

In order to determine b_o we consider the equation which gives the rate at which particles leave the surface because of evaporation.

$$\left(\frac{dn}{dt} \right)_{ev} = \theta b_o \exp \left(- \frac{E_a + Q}{RT} \right) = \frac{n}{\tau_{av}}, \quad (2.68)$$

where

n is the number of particles in the adsorbed state per unit area,

τ_{av} is the average sticking time of particles on the surface,

θ is the fractional coverage of the surface.

It can be expressed as

$$\theta = \frac{n}{N} \quad (2.69)$$

where

N is the number of available adsorption sites per unit area.

We have from Equation (2.68)

$$\tau_{av} = \frac{N}{b_o} \exp \left(\frac{E_a + Q}{RT} \right) = \tau_o \exp \left(\frac{E_a + Q}{RT} \right), \quad (2.70)$$

where

$$\tau_o = \frac{N}{b_o}. \quad (2.71)$$

where τ_o is the sticking time when no activation and adsorption energies exist, i.e., a passive surface. The interaction time in that case should be of the order of $\frac{h}{kT}$ (where h is Planck's constant) the period of the surface vibration ($\approx 10^{-13}$ sec). The number of sites per unit area is estimated to be of the order of $10^{15}/\text{cm}^2$ (Ehrlich, 1959). Thus we find b_o to be of the order of $10^{28}/\text{cm}^2\text{sec}$.

The recombination coefficient is defined as the ratio of the average molecular oxygen flux leaving the surface because of atomic recombination to the atomic oxygen flux approaching the surface multiplied by two for normalization. The rate of direct recombination is proportional to the fractional surface coverage θ and the incoming atomic oxygen flux. The rate of surface recombination is proportional to θ^2 . Thus the recombination coefficient γ is given as

$$\gamma = \frac{2 \phi_2(O_2)}{\phi_2(O)} = \frac{2(\theta \phi_2(O) \kappa_D + \theta^2 \kappa_S)}{\phi_2(O)} \quad (2.72)$$

where the first term in the right side of Equation (2.72) is the contribution due to direct recombination and the second term is the contribution due to surface recombination. The

choice of the recombination term depends on the particular model which is used to describe the recombination process. Brennan (1964) proposes a hopping model in which the surface recombination term is given as $\theta^2 \kappa_s' / (1-\theta)$. Brennan's model assumes that the atoms move across the surface by actually hopping from site to site. Thus atoms are leaving the surface for short time intervals, but are unable to escape and return to the surface. This motion continues until a site is found which provides a strong surface bond or until the atom is able to escape from the surface. The factors κ_D and κ_s are the recombination probabilities for direct and surface recombination. They can be expressed as

$$\kappa_D = \kappa_{D0} \exp \left(- \frac{E_D}{RT} \right) \quad (2.73)$$

and

$$\kappa_s = \kappa_{s0} \exp \left(- \frac{E_s}{RT} \right) \quad (2.74)$$

where

E_D is the activation energy for recombination of atoms from the gas phase, and

κ_{D0} is a constant whose value is estimated to be near unity.

Similarly

E_s is the activation energy for surface recombination, and if we adopt Brennan's hopping model

$$\kappa_{s0} = N \omega \quad (2.75)$$

where

ω is the hopping frequency, given as

$$\omega = \omega_0 \exp \left(- \frac{E_m}{RT} \right) \quad (2.76)$$

ω_0 is the lattice vibration frequency of order 10^{13} /sec,
and

E_m is the activation energy for surface diffusion.

2.4 DETERMINATION OF THE FRACTIONAL SURFACE COVERAGE

The recombination probabilities κ_D and κ_S depend only on the surface parameters but the recombination coefficient depends on the particle flux through the fractional surface coverage, θ . The steady state assumption requires that the surface be in equilibrium with the gas in the chamber. To satisfy that condition the change in the flux has to be slow enough to permit the gas in the chamber to reach a quasi-equilibrium with the surface. An adsorption isotherm can then be found relating θ to the surface parameters and the gas density in the chamber.

The number of oxygen atoms adsorbed per unit area and unit time is given by

$$\left(\frac{dn}{dt}\right)_{\text{ads}} = \phi_2(0) f_1(\theta) a, \quad (2.77)$$

where

$f_1(\theta)$ is the probability of finding an available adsorption site.

The rate of desorption per unit area, the rate at which adsorption sites become available, is given by

$$\left(\frac{dn}{dt}\right)_{\text{des}} = b f_2(\theta) + \phi_2(0) f_2(\theta) \kappa_D + 2 f_2(\theta)^2 \kappa_S. \quad (2.78)$$

where

$f_2(\theta)$ is the probability of a site being occupied.

The first term on the right side of Equation (2.78) is the rate of evaporation of atoms from occupied sites, the second term is the rate of desorption due to recombination with atoms from the gas phase, and the third term is the desorption rate due to surface recombination. In equilibrium

$$\left(\frac{dn}{dt}\right)_{\text{ads}} = \left(\frac{dn}{dt}\right)_{\text{des}} \quad (2.79)$$

If we assume that the adsorbed atoms are noninteracting and only one atom can be adsorbed per site, we have

$$f_1(\theta) = 1 - \theta, \text{ and} \quad (2.80)$$

$$f_2(\theta) = \theta. \quad (2.81)$$

From Equation (2.77) and Equation (2.78), using Brennan's hopping model for surface recombination, we obtain

$$\phi_2(0) a (1-\theta) = b \theta + \phi_2(0) \theta \kappa_D + \frac{2 \theta^2 \kappa_s}{1 - \theta}. \quad (2.82)$$

After rearranging,

$$\begin{aligned} \theta^2 - \frac{\phi_2(0) (2 a + \kappa_D) + b}{\phi_2(0) (a + \kappa_D) + b + 2 \kappa_s} \theta + \\ \frac{\phi_2(0) a}{\phi_2(0) (a + \kappa_D) + b + 2 \kappa_s} = 0 \end{aligned} \quad (2.83)$$

and

$$\theta = \frac{1}{2} A \left[1 - \sqrt{1 - \frac{4 B}{A^2}} \right] \quad (2.84)$$

where

$$A \equiv \frac{\phi_2(0) (2 a + \kappa_D) + b}{\phi_2(0) (a + \kappa_D) + b + 2 \kappa_s} \quad (2.85)$$

and

$$B \equiv \frac{\phi_2(0) a}{\phi_2(0) (a + \kappa_D) + b + 2 \kappa_s}. \quad (2.86)$$

Substitution of Equation (2.84) into Equation (2.72) yields the derived expression of the recombination coefficients in terms of the surface parameters and the particle flux. As can be expected, the recombination process tends to make the relations between ambient atomic oxygen density and the particle density in the spectrometer chamber nonlinear.

Equation (2.72) for the recombination coefficient applies to monolayer adsorption on a uniform surface of any size large compared to the atom spacing on the surface. Thus if the surface is composed of many patches with different adsorption and recombination properties, the gas in the chamber will come to an equilibrium with each patch and the recombination coefficient and fractional surface coverages are given by Equation (2.72) and Equation (2.84) respectively, for each patch.

2.5 DISCUSSION OF ADSORPTION AND RECOMBINATION MODELS

Adsorption energies, recombination coefficients, and activation energies for surface diffusion are not known for atomic oxygen on most metal and metal oxide surfaces. Recombination coefficients have been measured by several researchers (Kaufman, 1961; Dickens and Sutcliffe, 1964; Morgan and Schiff, 1965; Greaves and Linnett, 1958; 1959a,b,c). Usually these measurements were made at relatively high pressures where it was assumed that direct recombination was the rate-determining process. Most measurements were also made after a sufficiently long exposure to atomic oxygen so that steady state conditions could be assumed. Myerson (1965, 1968) made measurements by exposing thin film probes of gold, silver, palladium, and platinum to a step-function flow of atomic oxygen and concluded that at the initial exposure an oxide is formed at the surface. According to Myerson this oxide formation, occurring in several steps, forms first a "low level" oxide which is gradually changed to a final stable oxide. His conclusions are based on interpretations of the measured heat flux into the catalytic surface during atomic oxygen exposure. Myerson did not analyze the exposed surfaces in order to determine their exact surface states. For our application the published value of recombination coefficients can be used only to indicate a general trend.

Heats of adsorption are known for atomic oxygen on tungsten surfaces and no values of activation energies for surface diffusion are available. Similarly, the sticking

probability is not well known. It is usually assumed (Ehrlich, 1959) that on clean metal surfaces the sticking probability of atomic oxygen is near unity and no activation energy for adsorption is required. Oxide surfaces, however, may require an activation energy of adsorption which reduces the sticking probabilities to less than unity. This is reflected in thermal accommodation coefficient measurements. For example, Wise, Wood, and Rajapakse (1966) suggest a thermal accommodation coefficient of atomic oxygen on silicon monoxide of $\alpha = 0.01$.

Depending on the value of these parameters, the recombination coefficient of a surface at the pressure range of interest here ($10^{-5} - 10^{-9}$ torr) can differ considerably from the value at high pressure ($10^{-2} - 10^{-3}$ torr) and can be a function of the surface flux while it is independent of flux at high pressures. Thus, for example, if we assume that the heat of adsorption is $Q \approx 30$ Kcal/mole, the activation energy for surface diffusion is $E_m \approx \frac{1}{5}Q = 6$ Kcal/mole (Ehrlich, 1959), $\kappa_G = 0.1$ and $a = 1$. We can further assume that the rate of surface recombination is given as

$$\kappa_S = N \omega \kappa_D \quad (2.87)$$

which implies that a hopping atom after leaving the surface has the same probability of recombination when it encounters an adsorbed atom as the atom coming from the gas phase.

With $\omega_O = 10^{13} \text{ sec}^{-1}$, $N = 10^{15} \text{ cm}^{-2}$, and $b_O = 10^{28} \text{ cm}^{-2} \text{ sec}^{-1}$, we obtain

$$b = 2 \times 10^6 \text{ cm}^{-2} \text{ sec}^{-1} \text{ and}$$

$$\kappa_s = 4.54 \times 10^{22} \text{ cm}^{-2} \text{ sec}^{-1}. \quad (2.88)$$

Since the flux values, corresponding to the pressure values of 10^{-6} torr and 10^{-9} torr, are $\approx 2 \times 10^{15}$ and 2×10^{12} atoms/cm²sec, respectively, we find that surface recombination is the rate determining process, and the fractional surface coverage is given by

$$\theta = \sqrt{\frac{a \phi_2(0)}{2 \kappa_D}} \quad (2.89)$$

and the recombination coefficient is

$$\gamma = \frac{2 \theta^2 \kappa_D}{(1-\theta) \phi_2(0)} \approx \frac{2 \theta^2 \kappa_D}{\phi_2(0)} = 1. \quad (2.90)$$

The numerical values for θ are

$$\theta = 4.7 \times 10^{-4} \text{ for } \phi_2(0) = 2 \times 10^{16} \text{ atoms cm}^{-2} \text{ sec}^{-1} \quad (2.91)$$

and

$$\theta = 4.7 \times 10^{-6} \text{ for } \phi_2(0) = 2 \times 10^{12} \text{ atoms cm}^{-2} \text{ sec}^{-1}. \quad (2.92)$$

Even at much lower recombination probabilities, i.e., $\kappa_D = 10^{-4}$, the situation would not be changed significantly. The surface coverage would increase by $10^{3/2}$ but γ would still be near unity. One could argue, for example, that the activation energy for surface diffusion is of the same order as the heat of adsorption. This is true when the adsorption sites are

widely separated as is expected on oxide surfaces. Thus we assume $Q \approx 30$ Kcal/mole, $E_m \approx 30$ Kcal/mole and if $\kappa_D \approx 0.1$, we have

$$b = 2 \times 10^6 \text{ cm}^{-2}\text{sec}^{-1} \text{ as before} \quad (2.93)$$

and

$$\kappa_s = 2 \times 10^5 \text{ cm}^{-2}\text{sec}^{-1}. \quad (2.94)$$

In this case surface diffusion and direct evaporation are negligible compared to direct recombination and we have

$$\theta = \frac{a}{a + \kappa_D} \quad (2.95)$$

and

$$\gamma = \frac{2 \kappa_D}{1 + \kappa_D} \quad (2.96)$$

and therefore

$$\theta = \frac{1}{1.1} = 0.91, \quad \gamma = \frac{0.2}{1.1} = 0.18. \quad (2.97)$$

While in both cases the recombination coefficients are independent of the surface flux, a desirable quality for practical reduction of atmospheric data, the surface coverage is nearly complete in the second case and we must expect a buildup of a second layer. The adsorption and recombination properties on this layer will then be rate-determining. If the heat of adsorption in the second layer is small (perhaps only physical adsorption occurs) and if the activation energy

for surface diffusion on the second layer is as high as the adsorption energies, then evaporation will be the rate-controlling process on the second layer and there will not be a noticeable change in the results. If, however, surface diffusion is very rapid on the second layer, it must be expected that due to surface recombination on the second layer we will have a higher recombination coefficient than that computed from single layer theory.

A more critical situation arises when the heats of adsorption and the activation energy for surface diffusion are about 15 Kcal/mole. This value can perhaps be expected for oxide surfaces. With $\kappa_D \approx 0.1$ we find

$$b = 1.4 \times 10^{17} \text{ cm}^{-2} \text{ sec}^{-1}, \kappa_s = 1.4 \times 10^{16} \text{ cm}^{-2} \text{ sec}^{-1} \quad (2.98)$$

and no simplifications are permissible in the expression for θ and γ . Thus we find for $\phi_2(0) = 2 \times 10^{10} \text{ atoms/cm}^2 \text{ sec}$

$$\theta = 0.122, \gamma = 0.048 \quad (2.99)$$

and for $\phi_2(0) = 2 \times 10^{12} \text{ atoms cm}^{-2} \text{ sec}^{-1}$

$$\theta = 1.43 \times 10^{-5} \text{ and } \gamma = 5.7 \times 10^{-6}. \quad (2.100)$$

The fractional coverage is small in both cases so that multiple layer adsorption does not have to be considered. If we assume $\kappa_D \approx 10^{-4}$, we have for $\phi_2(0) = 2 \times 10^{16} \text{ atoms cm}^{-2} \text{ sec}^{-1}$

$$\theta = 0.231 \text{ and } \gamma = 2.47 \times 10^{-5} \quad (2.101)$$

and if $\phi_2(0) = 2 \times 10^{12}$ atoms $\text{cm}^{-2}\text{sec}^{-1}$

$$\theta = 1.43 \times 10^{-5} \text{ and } \gamma = 2.47 \times 10^{-9}. \quad (2.102)$$

Comparing the last result with a case in which $\phi_2(0)$ is of the order of 2×10^{19} corresponding to a pressure of 10^{-2} torr, we obtain $\gamma = 0.2$ and 2×10^{-4} respectively for $\kappa_D \approx 0.1$ and 10^{-4} .

2.6 VALIDITY OF THE STEADY STATE ASSUMPTION

The examples above demonstrate the complexity of the physical systems that determine the recombination coefficient. Since all derivations and computations have been made for steady state assumptions, it is necessary to find the range of applicability of these conditions. In order to apply the steady state assumptions, the surface must come to an equilibrium with the gas in the chamber in a much shorter time than the density changes because of the change in altitude and/or angle of attack of the instrument. Subtracting Equation (2.78) from (2.77) we obtain the net rate of adsorption

$$\left(\frac{dn}{dt}\right)_{\text{ads}} - \left(\frac{dn}{dt}\right)_{\text{des}} = N \frac{d\theta}{dt} = \phi_2(0) (1-\theta) a - b\theta - \phi_2(0)\theta\kappa_D + \frac{2\theta^2\kappa_s'}{1-\theta}. \quad (2.103)$$

If we consider first the case where surface recombination can be neglected, Equation (2.103) reduces to

$$\frac{d\theta}{dt} + \frac{b + \phi_2(0)(a+\kappa_D)}{N} \theta = \frac{\phi_2(0)a}{N} \quad (2.104)$$

and after integration, by assuming $\theta = 0$ at $t = 0$,

$$\theta(t) = \frac{\phi_2(0)a}{b + \phi_2(0)(a+\kappa_D)} \left[1 - \exp\left(-\frac{t}{\tau}\right) \right] \quad (2.105)$$

where

$$\tau = \frac{N}{b + \phi_2(O) (a + \kappa_D)}. \quad (2.106)$$

Thus, if τ is small compared to the time during which $\phi_2(O)$ is expected to change, we can assume that the steady state assumption is sufficiently satisfied. Recalling the example given above for $Q \approx 30$ Kcal/mole, $E_m \approx 30$ Kcal/mole, and $\kappa_D \approx 0.1$, we find τ to be

$$\tau = \frac{10^{15}}{10^6 + 2 \times 10^{16} (1+0.1)} \approx 0.05 \text{ sec} \quad (2.107)$$

for $\phi_2(O) = 2 \times 10^{16}$ atoms $\text{cm}^{-2}\text{sec}^{-1}$
and $\tau = 500$ sec for $\phi_2(O) = 2 \times 10^{12}$ atoms $\text{cm}^{-2}\text{sec}^{-1}$.
(2.108)

A different value of κ_D will change the result only insignificantly. Thus in this case the steady state condition is not satisfied at the higher altitude since the density varies more rapidly than the 500 sec time would require. Similarly, the last example with $Q \approx 15$ Kcal/mole, $E_m \approx 15$ Kcal/mole and $\kappa_D \approx 10^{-4}$

$$\tau = \frac{10^{15}}{1.4 \times 10^{17} + 2 \times 10^{16} (1+10^{-4})} = 6.25 \times 10^{-3} \text{ sec} \quad (2.109)$$

for $\phi_2(O) = 2 \times 10^{16}$ atoms $\text{cm}^{-2}\text{sec}^{-1}$
and

$$\tau = \frac{10^{15}}{1.4 \times 10^{17}} = 7.15 \times 10^{-3} \text{ sec} \quad (2.110)$$

for $\phi_2(0) = 2 \times 10^{12} \text{ atoms cm}^{-2} \text{sec}^{-1}$.

In this case the rapid evaporation of atoms is responsible for the fast time response. We consider now the case in which surface diffusion determines the response time. From Equation (2.103) we have, neglecting the term which contains κ_D and b , and assuming that $\theta \ll 1$,

$$N \frac{d\theta}{dt} = \phi_2(0) (1-\theta) a - 2 \theta^2 \kappa_s' \quad (2.111)$$

or

$$\frac{d\theta}{\phi_2(0) (1-\theta) a - 2 \theta^2 \kappa_s'} = \frac{dt}{N} \quad (2.112)$$

After integration, we assume that at $t = 0$, $\theta = 0$, and therefore

$$\begin{aligned} \theta(t) &= 2 \frac{1 - \exp\left(-\frac{t}{\tau}\right)}{1 - \exp\left(-\frac{t}{\tau}\right) + \sqrt{1 + \frac{8 \kappa_s'}{a \phi_2(0)}} [1 + \exp\left(-\frac{t}{\tau}\right)]} \\ &= 2 \frac{1}{1 + \sqrt{1 + \frac{8 \kappa_s'}{a \phi_2(0)}} \coth\left(\frac{t}{2\tau}\right)} \approx \sqrt{\frac{a \phi_2(0)}{2 \kappa_s}} \tanh\left(\frac{t}{2\tau}\right) \\ &\quad \left(\kappa_s \gg \phi_2(0)\right) \end{aligned} \quad (2.113)$$

where

$$\tau = \frac{N}{[(a \phi_2(0))^2 + 8 a \phi_2(0) \kappa_s']^{\frac{1}{2}}} \quad (2.114)$$

is the time constant of the system. For the example above where $Q \approx 30$ Kcal/mole and $E_m \approx 6$ Kcal/mole, we have for $\phi_2(0) = 2 \times 10^{16}$ atoms $\text{cm}^{-2}\text{sec}^{-1}$.

$$\tau = \frac{10^{15}}{(4 \times 10^{32} + 8 \times 2 \times 10^{16} \times 4.54 \times 10^{22})^{1/2}} \approx 1.2 \times 10^{-5} \text{ sec} \quad (2.115)$$

and for $\phi_2(0) = 2 \times 10^{12}$ atoms $\text{cm}^{-2}\text{sec}^{-1}$

$$\tau = \frac{10^{15}}{(4 \times 10^{22} + 7.25 \times 10^{35})^{1/2}} \approx 1.2 \times 10^{-3} \text{ sec.} \quad (2.116)$$

These examples indicate that only in cases where the heat of adsorption Q and/or the activation energy for surface diffusion, E_m , are small, is the response of the surface adequate for the steady state assumption. In the case where $Q \approx 30$ Kcal/mole and $E_m \approx 30$ Kcal/mole we must consider second layer adsorption.

Note, however, if the time constant for second layer adsorption is very small, then after a sufficiently long initial exposure (larger than 500 sec), we should expect a fast total surface response.

CHAPTER III

AN ATOMIC OXYGEN BEAM GENERATOR

3.1 METHODS FOR GENERATING ATOMIC OXYGEN

In this section a short review is given of the methods commonly employed to generate atomic oxygen for laboratory experiments.

3.1.1 Glow Discharge Method

The dissociation of oxygen molecules in a glow discharge has been the most frequently used method for atomic oxygen generation. Usually molecular oxygen flows from a reservoir through a flow-controlling valve into a long pyrex or vycor tube where it is ionized in an electrodeless radio-frequency glow discharge. The gas pressure in the tube has to be kept between 0.1 and 10 torr in order to maintain a stable glow. As a result of the high plasma temperature a large fraction of the molecular oxygen becomes dissociated. Depending on the particular experimental arrangement, a target is usually placed some distance downstream beyond the point where all ionized particles have been removed. Some of the oxygen atoms will have recombined by the time they reach the target area, but atomic concentrations as high as 40% have been reported by Greaves and Linnett (1959c). Such

high concentrations could be maintained only by adding 3% of water to the molecular oxygen. With pure oxygen, they obtained an atomic concentration of only 1%. Similar results were obtained by Herzog (1964). Herzog added 1% of sulphur hexafluoride (SF_6) to the oxygen and obtained a relative concentration of atoms of 20%. Relatively large atomic concentrations were also obtained by adding helium to the oxygen stream. However, large quantities (80%) of helium had to be added to maintain a large atom-to-molecule ratio.

Narcisi, et al. (1963) produced atomic oxygen by titrating atomic nitrogen and nitric oxide. Atomic nitrogen was formed in a radio-frequency discharge of molecular nitrogen and the atomic oxygen was formed in the reaction $\text{N} + \text{NO} \rightarrow \text{N}_2 + \text{O}$. The atomic oxygen yield in this system is very low; only a fraction of a percent was obtained by Narcisi, et al. However, the almost complete absence of molecular oxygen makes this method very attractive.

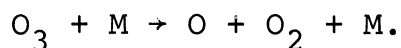
Several difficulties arise if these techniques are used to supply the oxygen atoms for a flight mass spectrometer study. Since atoms can be generated only at a gas pressure which is much higher than the permissible pressure, a reducing system is required which can maintain a pressure difference of several orders of magnitude without significantly reducing the relative concentration of atoms. Ion sources in which ions are formed by electron impact, produce, aside from singly ionized atomic oxygen, doubly ionized and dissociatively ionized molecular oxygen. If pure oxygen is dissociated in

a glow discharge, it is difficult to separate the small quantities of atomic oxygen from the background produced by the molecular oxygen. The conditions are improved by adding impurities, but these impurities may also contaminate the surfaces of the test instruments. The disadvantage of the nitrogen titration method is the low concentration of atoms. If, for example, the highest operating pressure of the mass spectrometer is 10^{-5} torr and the relative concentration of atoms is 0.1%, the maximum atomic oxygen pressure at which the spectrometer can be tested is only 10^{-8} torr.

3.1.2 Thermal Decomposition of Ozone

In an effort to produce an uncontaminated flow of electronically unexcited oxygen atoms, Kaufman and Kelso (1964) and Kelso (1966) generated atomic oxygen by thermal decomposition of ozone.

Ozone is produced by an electric arc which is formed in purified oxygen at atmospheric pressure. Ozone concentrations between 0.4 and 3% were obtained by Kelso (1966). The resulting mixture of ozone and molecular oxygen is then trapped on silica gel at 195°K, a method which provides an easy storage of ozone. Kelso (1966) reported that 600 g of silica gel stores 30 to 48 g of ozone. The ozone is recovered by passing a carrier gas over the gel. Molecular oxygen or helium was suggested by Kelso (1966). The atomic oxygen is produced by causing the gas mixture to flow through a quartz furnace which is heated to about 1300°K. The ozone decomposes according to the reaction



Intensive cooling of the furnace exit is required to avoid rapid recombination of the oxygen atoms on the furnace walls. Residual ozone can be minimized by the proper choice of the furnace length, the temperature, and the flow rate.

When molecular oxygen is used as a carrier gas, the relative concentration of atoms is very small (<0.5%). In helium the ratio of atomic to molecular oxygen is expected to be higher because molecules are formed only by the ozone decomposition and by recombination of atoms. However, a large helium background remains. The operating pressure is between 0.5 and 3 torr, and therefore a pressure reduction is required in order to adapt this system for mass spectrometer evaluation.

3.1.3 Thermal Dissociation of Oxygen Molecules

The atomization of hydrogen molecules by a hot tungsten filament was first studied by Langmuir (1912, 1915), and his method to study the simplest process of heterogeneous catalysis has been adopted by many other workers. Several different filament materials were used as catalytic surfaces and attempts were made to extend the method to dissociate molecular oxygen. Brennan (1964) and Ehrlich (1959) have given qualitative explanations of the dissociation and recombination processes on solid surfaces. Theoretical considerations leading to quantitative predictions have not been successful.

The process of molecular dissociation on hot solid surfaces is just the reverse of the recombination process considered in Section 2.2. An exact description of the mechanics is difficult because it is not known which of the many possible reactions involved in dissociation and evaporation is effective in the process. If there is only single layer adsorption, then the effective dissociation is determined by the competition between evaporation and surface recombination. If multilayer adsorption occurs, we have competing processes of horizontal and vertical surface recombination and atomic evaporation.

Let us consider a molecular gas in contact with a hot metal surface in a system so arranged that all atoms which evaporate from the surface are immediately removed. Restricting oneself to single layer adsorption, the steady state fluxes are equated to give

$$2 \phi(O_2) (1-\theta)^2 a_o' \exp\left(-\frac{E_a'}{RT}\right) = \theta b + \theta^2 \kappa_s. \quad (3.1)$$

The left side of Equation (3.1) expresses the rate of condensation and dissociation, and the terms on the right side are atomic and molecular evaporation rates from the surface. E_a' is the activation energy for dissociation and a_o' is the probability of success if a pair of sites is found by a molecule with sufficient energy. The primes are used to distinguish between the equilibrium process in an isothermal system and the present nonisothermal system. The factors b and κ_s are defined in Section 2.3.

The fractional dissociation is given as

$$T = \frac{\frac{1}{2} \theta b}{\phi(O_2)} \quad (3.2)$$

where θ is obtained from Equation (3.1). It is seen that, even in this simple case, T depends, in a rather complex way, on the various surface parameters and the primary molecular oxygen flux. The qualitative consideration above applies to metals and nonmetals. On insulators the electron mobility is greatly reduced and one can expect to find the adsorption sites more localized. This perhaps reduces the loss of atoms due to surface recombination.

As was mentioned earlier, the method of thermal dissociation has been used very successfully for the dissociation of hydrogen molecules, and only very little for the dissociation of molecular oxygen. Because of the strong chemical reactivity of oxygen and because of the high energy (5.08 eV) required for dissociation, not all metals which are successfully used for hydrogen dissociation are also suited for oxygen dissociation. Brennan, using a platinum filament, has obtained a probability of atomization of 0.058 at 1800°K. Noble metals are desirable since oxidation is essentially eliminated. However, large probabilities of atomization are obtained only at temperatures above 2000°K. Only the refractory metals, tungsten, tantalum, and perhaps molybdenum, can be brought to these temperatures without melting or rapid evaporation. The strong reactions of these metals with oxygen lead to a rapid formation of

various oxides. Turner, Compton and McGowen (1966) used a Thoria (ThO_2) oven and obtained more than 90% dissociation of molecular oxygen at 2400°K and 10^{-3} torr oven pressure. Besides its inertness, ThO_2 has a low vapor pressure and a high melting point. The disadvantage is its radioactivity. Even if only small amounts of Thoria are evaporated, they will gradually contaminate the vacuum system and the test instruments.

Experiments on the oxidation of tungsten carried out by Schissel and Trulson (1965) show that tungsten can be a suitable metal for oxygen dissociation provided it is kept at a high temperature. Schissel and Trulson found that at temperatures above 2300°K the oxide formation is exceeded by rapid evaporation of atomic oxygen. At 2800°K nearly all of the impinging molecular oxygen is dissociated and reemitted as atomic oxygen. Preliminary calculations, based on the data of Schissel and Trulson, showed that tungsten could be a useful material for atomic oxygen generation.

After a review of the methods for oxygen dissociation, it was concluded that for our application the method of thermal dissociation presents advantages over the other known methods. The basic experimental requirements are outlined below.

(a) A neutral particle beam shall be produced with an intensity similar to the intensity encountered in mass spectrometer applications in upper atmosphere experiments.

(b) The fraction of atomic oxygen in the beam shall be larger than 50% so that surface effects in the mass spectrometer can be recognized easily.

(c) Chemically active beam contaminants shall be negligible.

(d) The test system must be bakeable to 360°C for clean-up purposes and for simulation of the conditions encountered in the flight preparation of the mass spectrometer.

3.2 GENERATION OF ATOMIC OXYGEN BY THERMAL DISSOCIATION ON A HOT TUNGSTEN SURFACE

A simple way to generate an atomic oxygen beam by thermal dissociation is to cause a molecular oxygen beam to flow against a hot tungsten ribbon so that all molecules must collide with the ribbon at least once. The reemitted particles will have a spatial distribution according to the cosine law. To intercept a large fraction of the flow, the target must be placed close to the tungsten ribbon. This may produce mechanical design problems and the heat radiated by the tungsten ribbon can cause an undesirable temperature change on the target surface. By using the rate constants given by Schissel and Trulson (1965) estimates of the expected partial fluxes were computed as shown in Appendix A. The temperature of the tungsten ribbon was chosen to be 2800°K and all values were normalized to the incoming molecular oxygen flux. The results are shown in Figure 3.1. The relative flux values are plotted as a function of the incoming flux.

A disagreement between these values and those quoted by Schissel and Trulson (1965) was observed. This disagreement results from the different choice of the adsorption model used in the computations (see Appendix A). The values shown by the curves should therefore be considered the lower limit of the expected flux levels.

As can be seen in Figure 3.1, most of the molecular oxygen is dissociated when the incoming flux is less than

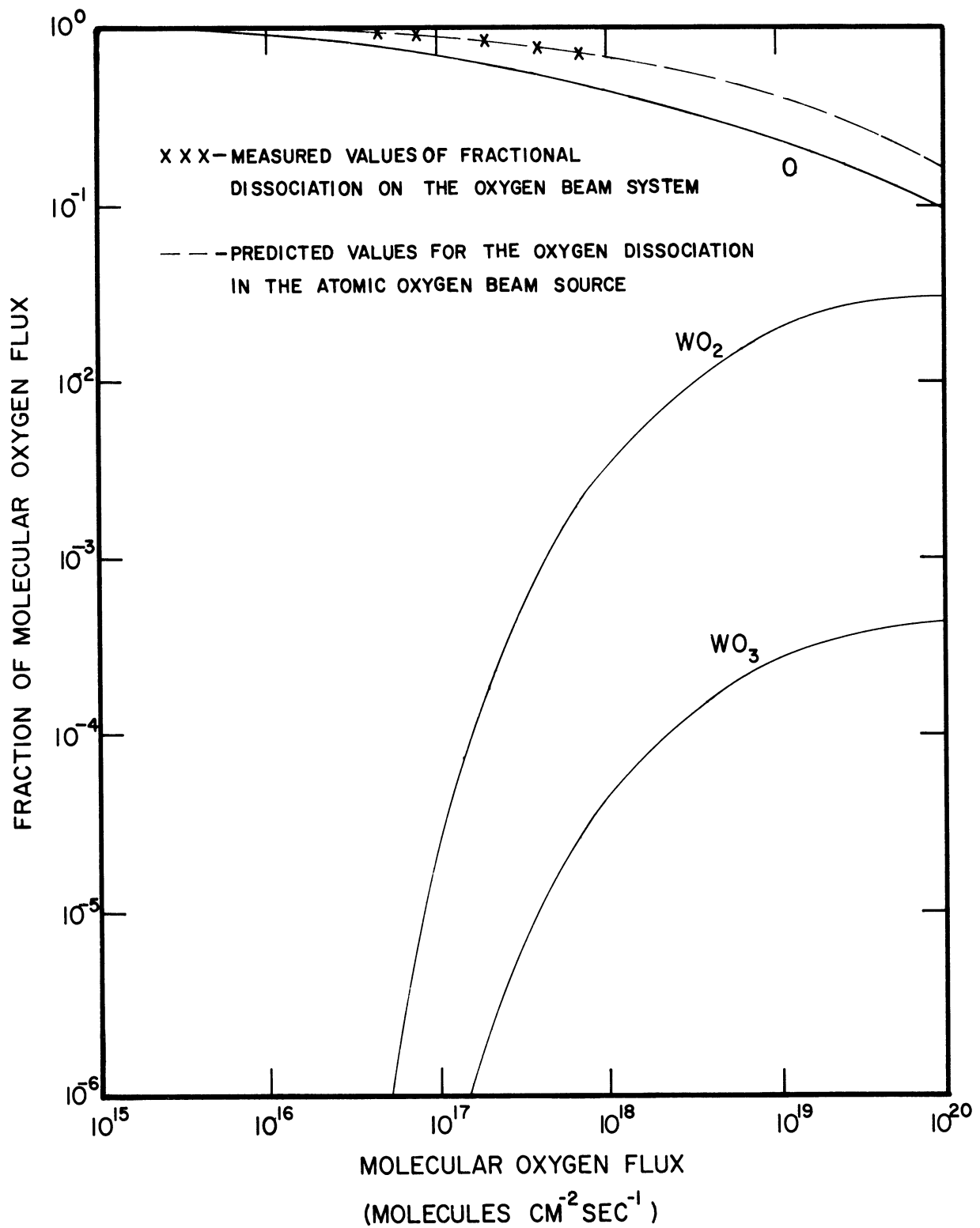


Figure 3.1 Fractional dissociation and oxide formation versus primary molecular oxygen flux on a tungsten surface at 2800°K.

10^{17} molecules/cm²sec, and the contribution of tungsten oxide is still less than one percent at flux levels of 10^{18} molecules/cm²sec. Above this level oxide formation increases very rapidly and the atomic oxygen evaporation decreases. Thus the application of this method is limited to a flux level of the order of 10^{18} molecules/cm²sec.

In the following paragraph several schemes are discussed for forming an atomic oxygen beam, of which the last one, being the most promising, was successfully employed in the design of the beam system.

Consider, as an example, an omegatron chamber with an orifice area of $S_{\Omega} = 1 \text{ cm}^2$ is placed at a distance $\ell_{\Omega} = 10$ cm from the tungsten ribbon and the normal to the orifice faces the ribbon. We find then the flux attenuation at the omegatron orifice to be

$$\frac{\phi_{\Omega}}{\phi_w} = \frac{\Omega}{\pi} = \frac{S_{\Omega}}{\pi \ell_{\Omega}^2} = \frac{1}{100 \pi} = 3.18 \times 10^{-3}. \quad (3.3)$$

Less than one percent of the generated particle flux is actually intercepted by the omegatron orifice. Thus most of the atoms and molecules do not contribute to the signal flux, and they must be removed rapidly in order to reduce the gas background. An improvement can be obtained if the atomic oxygen flux is focused into the target direction. Instead of reflecting the oxygen from a flat ribbon, one can produce a narrow oxygen beam by using a long tungsten tube heated to 2800°K. Oxygen molecules can collide several times with the tungsten walls and therefore a larger

effective dissociation can be expected. The oxide formation is also increased, however, because atomic oxygen reacts strongly with tungsten and tungsten dioxide is expected to be stable at 2800°K. However, a major difficulty arises in the design of the feeding system. To take full advantage of the beam focusing caused by the tungsten tube, the oxygen must be supplied to the tube center without flux leakage. This can be accomplished by extending the tungsten tube to the reservoir; however, since for practical reasons the oxygen reservoir must be kept at moderate temperatures, there will always be a section somewhere between the reservoir and the hot tip of the tube which is at a temperature where oxide formation is very rapid. Thus in moving from the reservoir to the hot tip of the tube, the oxygen always passes through a section where excessive oxide formation occurs and much of the oxygen is used up in the oxidation process before it reaches the part of the tube which is at an optimum temperature for molecular oxygen dissociation. Oxidation can be avoided by using feeder tubes made of SiO_2 or ThO_2 , but they will be destroyed when brought in contact with the hot tungsten tube.

The difficulties of low flux intensity and high background pressure when a flat tungsten ribbon is used for dissociation and the problem of excessive oxidation when a tungsten tube is employed can be overcome if a hot tungsten surface (i.e., a tungsten filament) is placed inside a chamber or tube which is made of nonreacting material, this

tube being kept at a low temperature so that atomic recombination on the walls is very low. The oxygen molecules will then collide once or several times with the tungsten filament and the walls of the envelope before they leave through an appropriately placed exit. Pyrex or titanium would be suitable envelope tube materials because of the low recombination efficiency of pyrex and titanium oxide (Morgan and Schiff, 1965). A titanium envelope would have to be oxidized, a process which can be accomplished in an initial burn-in process. Multiple collision of the molecules with the tungsten filament increases the net dissociation if the envelope is designed so that no significant wall recombination occurs before the atoms leave the chamber. The tungsten oxide formation on the envelope tube wall is also increased as compared with the flat ribbon case. However, most tungsten oxide molecules condense on the cold walls of the envelope. With time this condensation will change the surface properties of the envelope. The effect of such change on the atomic oxygen flux depends on the recombination and thermal accommodation properties of tungsten oxide. In the next section is a description of an atomic oxygen beam system which is designed according to this concept.

3.3 DESIGN OF THE ATOMIC OXYGEN BEAM SYSTEM

3.3.1 General Design Considerations

Meaningful laboratory measurements of the interaction of atomic oxygen with surfaces can be made only if the conditions encountered in the upper atmosphere are properly simulated. The gas composition and the flux intensity should be similar to those of the flight environment. In a typical rocket experiment, data are gathered in an altitude range from 150 km to 350 km. The total particle flux, consisting of nitrogen and oxygen in atomic and molecular form, varies from about 10^{16} particles/cm²sec at 150 km to about 10^{13} particles/cm²sec at 350 km. The relative concentration of the constituents varies with altitude. Each gas is distributed according to its scale height. Accordingly, the atomic oxygen flux varies from about 3×10^{15} atoms/cm²sec at 150 km to 1×10^{13} atoms/cm²sec at 350 km. Above 200 km, atomic oxygen becomes the major constituent in the atmosphere.

The quoted flux intensities are for the condition that the instrument is pointing into the direction of motion. If the instrument tumbles, the flux will vary periodically, decreasing several orders of magnitude when the sensor points away from the direction of motion.

In the laboratory simulation, the upper flux limit is determined by the maximum dissociation rate of the tungsten surface and associated tungsten oxide formation. The signal-to-background ratio is determined by the pumping capacity of the vacuum system. There is no lower flux limit, but the

signal-to-background ratio is determined by the base pressure which can be obtained with the vacuum equipment.

Quantitative measurements of the flux presented an experimental challenge. The calibration methods used in systems with high pressures (0.1 torr) are not applicable here because of the low sensitivities of the sensors. Mass spectrometers similar to the units to be tested by means of the oxygen beam have not been extensively used in laboratory experiments for atomic oxygen. However, their principles are well understood and comparisons are readily made between gases of known kinds. Experience gained in the present experiments has led to confidence in the use made of mass spectrometers for flux calibration and composition determination of the beam.

3.3.2 Technique for Measurements of the Flux Intensity and the Relative Concentration of Atoms in the Oxygen Beam

The most challenging aspect of the use of the oxygen beam system has been that of making quantitative measurements of the concentrations of atomic and molecular oxygen in the beam. A review of the techniques used by previous experimenters for determining atomic oxygen concentration has been given by Kaufman (1961). All the methods he describes give reliable measurements only at higher flux levels than are encountered in this experiment. Even if the detector sensitivities in the methods he describes are extended, adsorption of atomic oxygen on the walls can cause substantial errors. Thus perhaps a permanent and usually imperfectly known

adsorption of atomic oxygen on the walls of the instrument used to measure the atomic oxygen has been a continuing source of difficulty in the atmospheric oxygen measurement that has required the development of new techniques in the measurement and the treatment of the data.

Experience with various instrumental methods gained in the experimentations here reported has shown that the mass spectrometer is well suited to quantitative detection of the atomic oxygen beam, because of its great sensitivity and its mass selectivity. A combined use of an open ion source and a closed ion source mass spectrometer has made it possible to obtain a flux calibration. The relative concentrations of atomic and molecular oxygen are determined with the open ion source (a quadrupole instrument was used) which is designed and placed so that only beam particles are detected. The absolute flux of molecular oxygen is then measured with a closed source instrument for which the sensitivity to molecular oxygen is quantitatively known. Niemann and Kennedy (1966) showed that the omegatron system is well suited as a quantitative closed ion source detector of molecular oxygen in the concentration ranges here employed. As indicated in the introduction, an important objective of the investigation here described is to evaluate the omegatron system for atomic oxygen measurements. Thus the omegatron serves a double purpose, first, as the basic quantitative detector of the molecular oxygen content in the beam, and second, as the instrument to be evaluated as to its capability for measuring atomic oxygen.

Among the instruments available in the laboratory, an ATLAS quadrupole mass spectrometer type AMP 3 was found to be best suited as the open source instrument. The ion source design permitted an easy adaptation to molecular beam studies. A cross-sectional diagram of the ion source is shown in Figure 3.2. Ions are formed by electron impact ionization. A coaxial "Pierce-type" electron beam gun produces the ionizing electrons. The potential difference between the ion extraction electrode and the anode provides an electric field which focuses the ions produced around the center line near the anode so that they pass through the extraction tube into the analyzer section. The analyzer section consists of four rod-shaped electrodes of circular cross section. Opposite pairs of the electrodes are electrically connected. A two dimensional quadrupole electric field is established between the electrodes by applying a dc and an rf voltage to the rod pairs. The motion of the ions injected into the field in the direction parallel to the rods is described by a pair of Mathieu differential equations. The parameters of these equations are functions of the charge to mass ratio of the ions and the electric potentials applied to the rods. The solution of these equations designate oscillations performed by the ions in the direction perpendicular to the analyzer axis. Ions oscillate stably between the rods only when the electrical potential at the rods are chosen so that both solutions of the Mathieu equations are stable. The range of ionic masses which continues

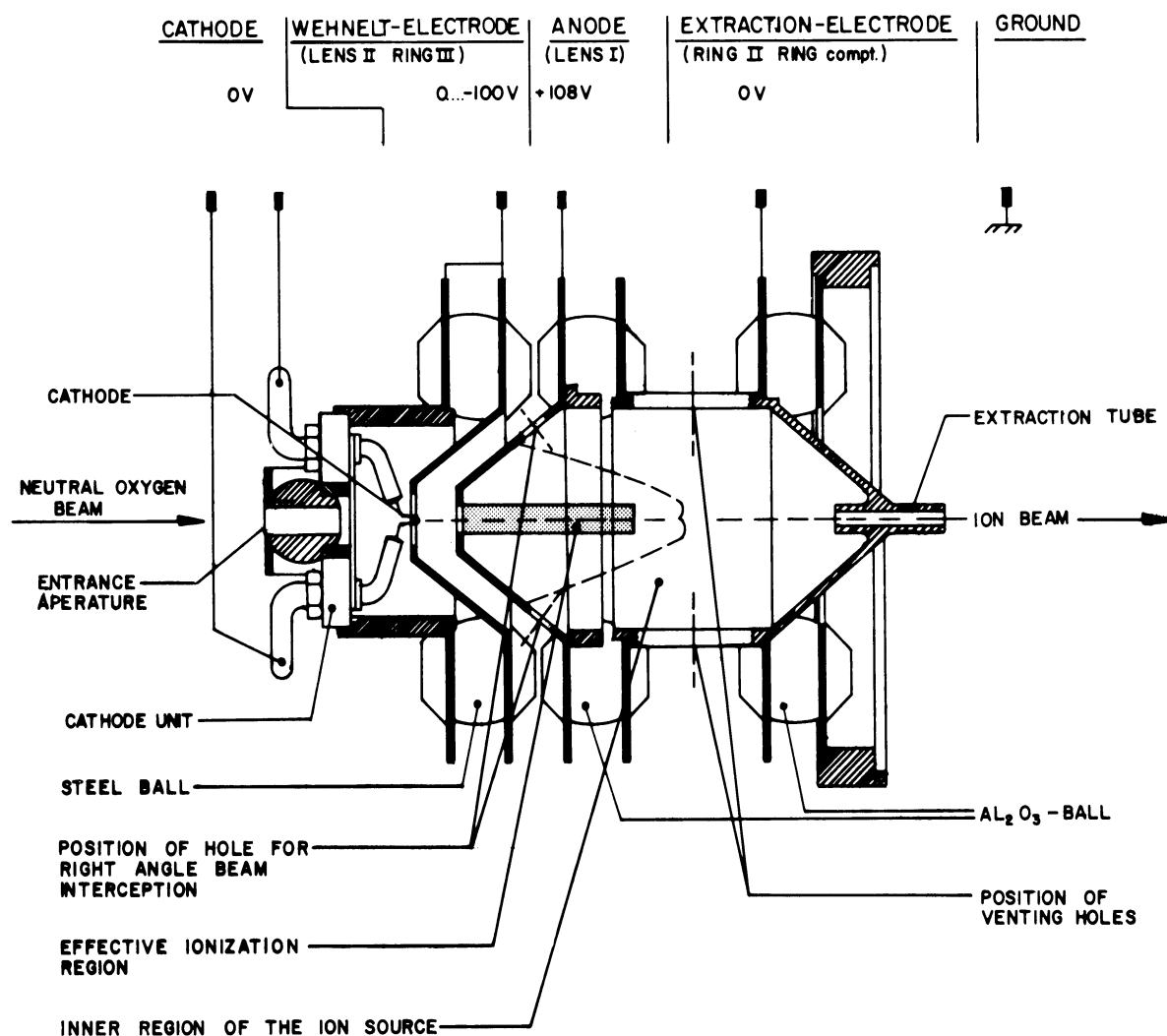


Figure 3.2 Cross-sectional view of the ion source of the ATLAS quadrupole mass spectrometer.

through the field with a stable trajectory is determined by the choice of the voltage applied to the rods. Ideally, the conditions of stability are independent of the initial position and velocity of the ions and of the radio-frequency phase at the time of injection. For an actual quadrupole mass spectrometer, however, mass separation depends not only on whether the oscillation of the ions is stable or unstable, but on whether ions are able or unable to travel through the analyzer without striking an electrode. An important consequence of this practical requirement is that the mass resolution becomes dependent on the lateral position and radial velocities of the ions entering the analyzer. Hence, the ion beam is usually restricted in cross section and angular divergence by a circular aperture placed at the entrance to the analyzer. As an ion detector, a Faraday cup or a secondary electron multiplier is usually placed at the other end of the analyzer. The design of the ATLAS quadrupole permits an alternate use of a Faraday cup or secondary electron multiplier. Because of the large sensitivity required for this experiment, measurements were made only with the secondary electron multiplier. The gain of the multiplier was usually adjusted to be between 10^5 and 10^6 . A detailed description of the ATLAS instrument is given by Brunée, Delgmann, and Kronenberger (1963).

For molecular beam detection of noncondensable gases it was necessary to modify the quadrupole ion source. The molecular beam can pass through the ionizing electron beam

either parallel or at right angles to the axis of the ion source. To avoid unpredictable mass and momentum discrimination among ionized beam particles in the source, it is important that the fraction of ions which is focused into the analyzer section be constant. Tests were carried out for right angle and parallel interception. In both cases a beam of gold vapor was used as a test beam. Gold is well suited for this purpose because it is easily evaporated, it condenses readily so only beam particles can be ionized, and its atomic mass number (197) is similar to the mass number of WO_2 and WO_3 . This allows for mass calibration of the spectrometer at high mass numbers.

For right angle beam interception, a pair of 4 mm diameter holes was drilled into the anode of the ion source to permit the gold beam to pass through the electron beam. No source modification was necessary for parallel beam interception.

The test with the electron beam parallel to the ion source axis was successful, in that relatively large ion currents were detected. With the electron beam intercepting the ion beam at right angles, initially no ion current could be detected. After changing the anode voltage from 130 V to 400 V, it became possible to focus a small number of gold ions. Based on this test, the right angle beam interception design was discarded.

The success of the parallel beam interception system is not surprising, because the gold beam is already directed

toward the analyzer section. Since the ion source is concentric, one can expect that nearly all ions formed in the ionizing region are focusing into the analyzer section.

Note, however, that the intercepted oxygen beam cannot be used simultaneously as a measurement of the relative particle concentration and as a test beam for the omegatron, because the beam which enters the quadrupole terminates in the instrument. Thus, a bidirectional oxygen beam source with symmetric particle flow is needed. The principle is illustrated in Figure 3.3 where the quadrupole, an open ion-source detector of relative magnitudes receives and terminates the beam that goes to the right, and the closed ion source omegatron is an absolute magnitude detector that is a termination target for the beam that goes to the left. Only a narrow particle stream can enter the ionization region of the quadrupole ion source directly through the center aperture. Particles not contained in this stream can still be ionized, but only after they collide once or several times with the source walls. Ion currents resulting from these particles cause an undesirable error in the measurement. To avoid the error, it is necessary to collimate the oxygen beam by reducing the flow with apertures of equal or smaller size than the entrance of the ion source, and by intensive pumping in the source region and the spaces around the apertures. Contributions of beam particles which pass the ionization region more than once as a result of wall collisions can be made negligible by proper venting of the source region. The effect of

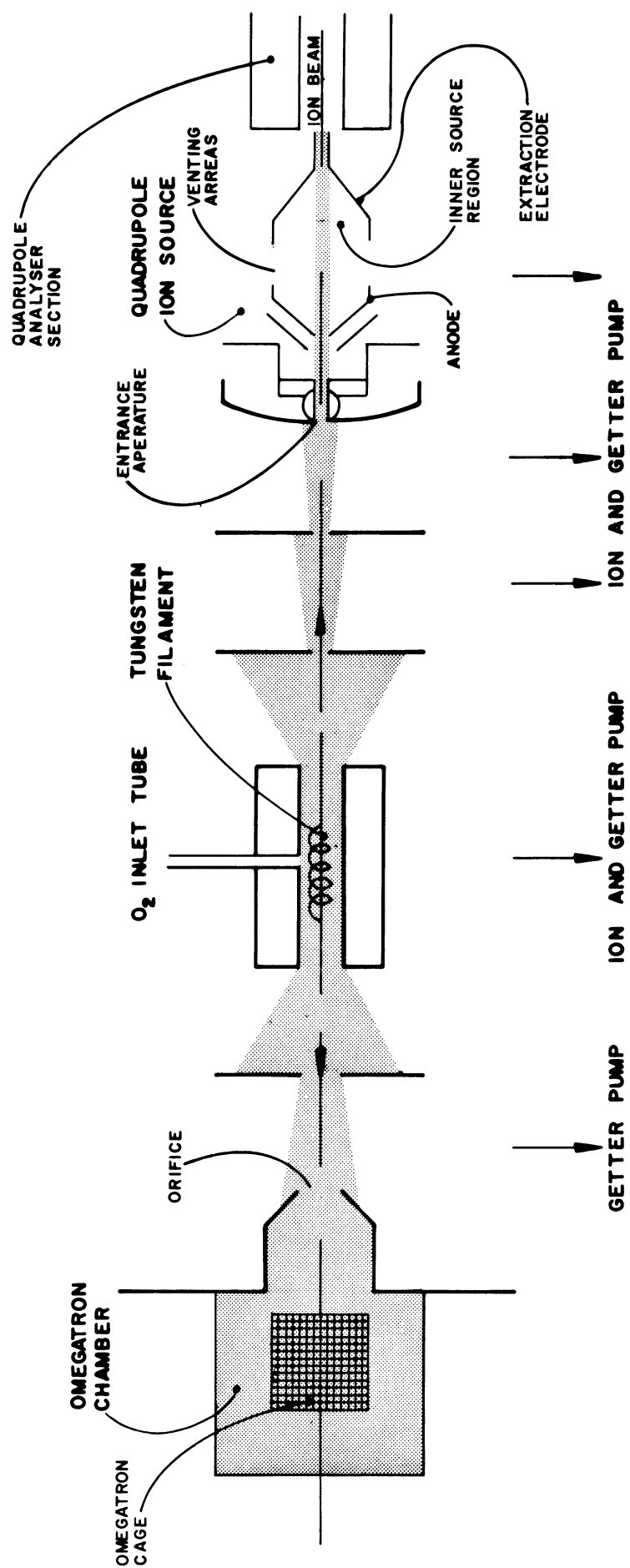


Figure 3.3 Schematic diagram of the bidirectional atomic oxygen beam system.

this backscattering is estimated by considering two cases, with particular reference to Figure 3.2.

First, the net contribution is estimated by computing the average particle density of beam particles in the ion source region, and second, by computing the particle density in the ion source region produced by particles which collide only once with the walls. This distinction is necessary because atomic oxygen may be absorbed or recombined after several wall collisions, but on the average it may not be effected much after only one surface collision.

Assuming that the particle beam is fully collimated when it reaches the ionization region, and that the effective ionization region is smaller than the beam diameter, we find the instantaneous beam particle density in the ion source region to be

$$n_b = \frac{\phi_b}{\bar{v}_b} \quad (3.4)$$

where ϕ_b is the particle flux in the beam, and \bar{v}_b is the average beam velocity. The net particle flux leaving the ion source region is given by

$$\phi_s = \frac{1}{4} n_s \bar{v}_s \quad (3.5)$$

where

n_s is the density of scattered particles in that region, and

\bar{v}_s is the average velocity of these particles.

It is presumed that the particles which comprise n_s have made several scattering collisions with the walls, thus at least partially accommodating to the wall temperature before passing out through the source venting area in the extraction electrode. Equality of flow in through the aperture, with that out through the venting area requires that

$$\phi_b S_b = \phi_s S_s \quad (3.6)$$

where the beam aperture area and the source venting area are S_b and S_s , respectively. Therefore, the ratio of beam-to-scattering particles in the ion source region is

$$\frac{n_b}{n_s} = 4 \frac{\phi_b}{\phi_s} \frac{\bar{v}_s}{\bar{v}_b} = 4 \frac{S_s}{S_b} \frac{\bar{v}_s}{\bar{v}_b} \approx \sqrt{\frac{T_s}{T_b}} \frac{S_s}{S_b} \quad (3.7)$$

where

T_s is the temperature of the scattered particles, and

T_b is the temperature of the beam particles.

Assuming, as a worst case condition, that the beam particles have a kinetic temperature of 2800°K, that the scattered particles are at room temperature, and that the contribution due to scattering should be of the order of 1%, we need an area ratio of

$$\frac{S_s}{S_b} = \sqrt{\frac{2800}{300}} 10^2 \approx 300. \quad (3.8)$$

The cross-sectional area of the beam is 0.0314 cm²; hence a venting area of 10 cm² is required. Such a large venting

area cannot be provided, but if it could, the effective venting would be larger than assumed because the volume of the ionization region is too small to permit the gas inside to reach equilibrium. As a practical compromise, venting was provided by drilling 4 venting holes of 1 cm diameter in the center section of the extraction electrode shown in Figure 3.2. To maintain a symmetric electric field in the center section, the holes were covered with a stainless steel grid of 85% optical transparency. Adding all venting areas in the source yielded 4.40 cm^2 . Thus,

$$\frac{n_b}{n_s} = \frac{1}{3.05} \frac{4.4}{0.0314} = 46, \quad (3.9)$$

and the maximum error is 2.2%. A photograph of the modified ion source is shown in Figure 3.4.

Considering now the particles which are scattered after the first bounce into the region where ionization occurs, we assume that the scattering source is a flat area located at the extraction tube (see Figure 3.2). It is also assumed that the scattering is according to the cosine law. Again, this is a worst case analysis. Some fraction of the beam will actually pass through the extraction tube into the analyzer section and as can be seen from the geometry of the section around the extraction hole (Figure 3.2), more favorable conditions would exist if the particles were reflected specularly. Therefore, the flux scattered from the extraction tube which passes through the region where ionization occurs

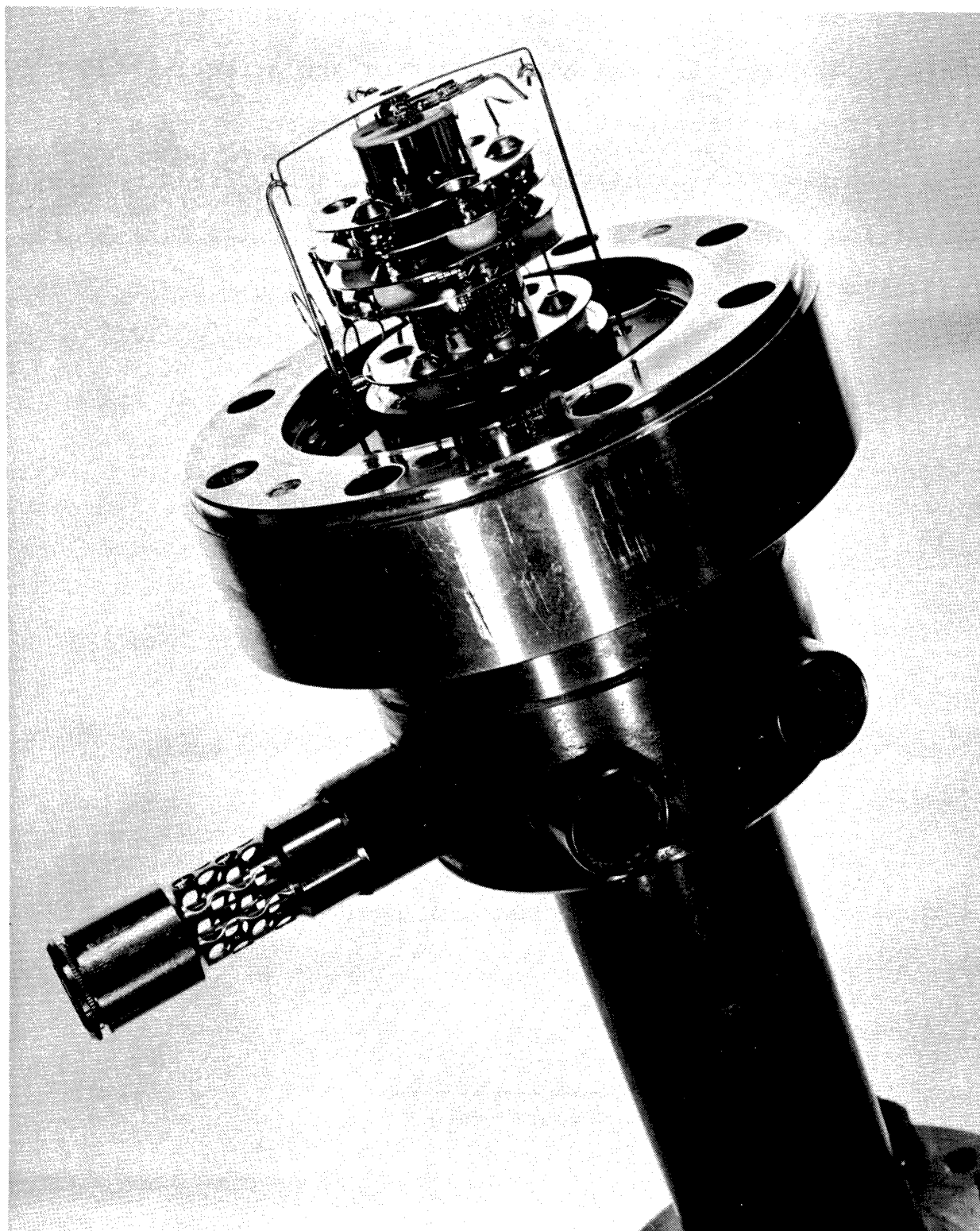


Figure 3.4 Modified ion source of the ATLAS quadrupole mass spectrometer.

(the effective ionization region) is

$$\phi_{sc} = \frac{\Omega_s}{\pi} \phi_b \quad (3.10)$$

where Ω_s is the solid angle subtended by the effective ionization region at the extraction tube entrance. From a retarding potential analysis and an approximate field mapping of the ion source region, it is concluded that the line of ionization starts at the center hole of the anode and extends about 1 cm toward the extraction electrode, shown by the shaded area in Figure 3.2. Most ions are produced in the center section of this line about 0.5 cm from the anode hole. Thus the average distance between the extraction tube and the ionization region is 2.5 cm, and Ω_s is obtained as

$$\Omega_s = \frac{0.0314}{2.5^2} = 5 \times 10^{-3} \quad (3.11)$$

If the one bounce scattered particles assume the surface temperature, and if the kinetic temperature of the beam is 2800°K, the density ratio in the effective ionization region of beam atoms to atoms backscattered from the extraction tube will be

$$\frac{n_b}{n_{sc}} = \frac{\pi}{\Omega_s} \sqrt{\frac{T_s}{T_b}} = \frac{\pi}{5 \times 10^{-3} \times 3.05} \approx 200. \quad (3.12)$$

The situation is actually better than suggested by Equation (3.9) and Equation (3.12) because of the extremely small ion collection efficiency of the ion source for thermal

particles. Computation has shown that in an equilibrium atmosphere only 0.03% of the ions produced by the electron beam are actually focused into the analyzer section. The failure, mentioned above, of the source to focus ions from a right angle beam interception is more evidence in support of this argument. Thus it would be fallacious to argue that the effective electron beam cross section is much wider than the neutral particle beam cross section. It is therefore concluded that only direct beam particles are analyzed in the quadrupole and contributions from scattered particles are negligible.

3.3.3 Determination of the Fractional Dissociation and the Relative Concentration of Atoms from Quadrupole Measurements

The number of ions produced in the ion source is proportional to the instantaneous particle density in the ionization region. To relate the measured density to the flux, it is necessary to know the average beam velocity or, if it is a thermal beam, the kinetic temperature of the beam. Therefore, we have

$$\phi_b = n_b \bar{v}_b \quad . \quad (3.13)$$

The output signal of the quadrupole detector and the particle density are related by

$$U_o = n_b S_{qp} \quad (3.14)$$

where the output voltage of the electrometer amplifier is U_o

and S_{qp} is the sensitivity of the quadrupole. The sensitivity is a function of the ionization cross section of atoms or molecules, the electron beam current, the combined ion extraction efficiency of the source and the mass analyzer section, the gain of the electron multiplier, and the transfer function of the electrometer amplifier. All quantities except the ion extraction efficiency are constant values for a particular species over a wide range of particle densities.

The ion extraction efficiency may depend on the velocity of the particles, but in this particular experiment, where all particles are moving in the desired direction toward the analyzer, the velocity discrimination is assumed to be negligible. The value of the ionization cross section depends on the relative velocity between the electrons and the neutral particles, but the kinetic energy of the electrons is much larger than the kinetic energy of the neutral particles (the effective electron energy is 75 eV) so that the change of the ionization cross section due to the neutral beam velocity change can also be neglected. For the analysis of two different species (i.e., atomic and molecular oxygen), it is necessary to know the ratio of the ionization cross sections, and the differences in transmission efficiency and quantum efficiency at the first dynode of the electron multiplier. The value used here for the ratio of the ionization cross section for atomic and molecular oxygen is the one measured by Fite and Brackmann (1959). The difference in transmission efficiency has been evaluated for argon by observing the

singly and doubly ionized argon atoms at 100% transmission and at the resolution required for the experiment. The ion source design does not simultaneously permit 100% transmission and a mass resolution adequate to separate the atomic masses 28 and 32. However, the ac to dc ratio of the radio-frequency generator which excites the quadrupole rods can be adjusted so that it is voltage-dependent, and permits constant transmission over a wide range of atomic mass numbers. This feature was utilized to set the transmission so that the ion current ratio of mass 20 to 40 was unchanged when the transmission was reduced from 100%. The difference in transmission properties between the mass 20 and 40 ratio and the mass 16 to 32 ratio is negligible.

The difference in the quantum efficiency of the first dynode of the secondary electron multiplier between masses 16 and 32 has not been directly measured. But from results of a study by Aehlig (1968) on an electron multiplier operated under similar conditions, the difference is believed to be negligible.

If the ratio of the sensitivities for atomic to molecular oxygen is known, the fractional dissociation and the partial atomic oxygen flux can be computed. If the primary molecular oxygen flux into the atomic oxygen source is constant independent of the temperature of the tungsten surface, and if no oxygen is lost because of absorption or oxide formation, we can compute the fractional dissociation by observing only the behavior of the molecular oxygen peak in the

quadrupole measurement. When dissociation is started, the molecular oxygen peak height will decrease proportionally to the amount of dissociation. The mass fluxes for no dissociation and for dissociation are

$$\dot{m}_c(O_2) = n_c(O_2) \bar{v}_c(O_2) m(O_2) \quad (3.15)$$

$$\dot{m}_h(O_2) = n_h(O_2) \bar{v}_h(O_2) m(O_2) \quad (3.16)$$

where the subscripts c and h are used to distinguish between no dissociation (cold tungsten) and dissociation (hot tungsten). The atomic oxygen mass flux is the difference of the two flux values

$$\dot{m}_h(O) = \dot{m}_c(O_2) - \dot{m}_h(O_2) \quad (3.17)$$

and the fractional dissociation is

$$\bar{T} = \frac{\dot{m}_h(O)}{\dot{m}_h(O_2) + \dot{m}_h(O)} = 1 - \frac{\dot{m}_h(O_2)}{\dot{m}_c(O_2)}. \quad (3.18)$$

After substitution of Equations (3.15) and (3.16), one obtains

$$\bar{T} = 1 - \frac{v_h(O_2) n_h(O_2)}{\bar{v}_c(O_2) n_c(O_2)}. \quad (3.19)$$

The average particle velocity in a thermal beam is given (Ramsey, 1963) as

$$\bar{v}_b = 1.33 \sqrt{\frac{2kT}{m}}. \quad (3.20)$$

Therefore,

$$\bar{T} = 1 - \sqrt{\frac{T_h(O_2)}{T_c(O_2)}} \frac{n_h(O_2)}{n_c(O_2)} = 1 - \sqrt{\frac{T_h(O_2)}{T_c(O_2)}} \frac{U_h(O_2)}{U_c(O_2)}. \quad (3.21)$$

When the tungsten surface is at ambient temperature or heated, T_c and T_h are the temperatures of the molecular oxygen and $U_c(O_2)$ and $U_h(O_2)$ are the corresponding signal levels of the quadrupole electrometer.

While the fractional dissociation is an important quantity for the evaluation of the functioning of atomic oxygen source, the relative particle flux is of more interest for gas surface interaction studies. We have for the cold-filament flux of molecular oxygen,

$$\phi_c(O_2) = n_c(O_2) \bar{v}_c(O_2), \quad (3.22)$$

for the hot-filament flux of molecular oxygen,

$$\phi_h(O_2) = n_h(O_2) \bar{v}_h(O_2), \quad (3.23)$$

for the hot-filament flux of atomic oxygen,

$$\phi_h(O) = 2 \left(\phi_c(O_2) - \phi_h(O_2) \right), \quad (3.24)$$

and the relative particle flux is

$$\bar{\eta} = \frac{\phi_h(O)}{\phi_h(O) + \phi_h(O_2)} = \frac{2 \left(\frac{\phi_c(O_2)}{\phi_h(O_2)} - 1 \right)}{2 \left(\frac{\phi_c(O_2)}{\phi_h(O_2)} - 1 \right) + 1}. \quad (3.25)$$

After substitution of Equations (3.22) and (3.23), one obtains

$$\bar{\eta} = \frac{2 \left(\sqrt{\frac{T_c(O_2)}{T_h(O_2)}} \frac{U_c(O_2)}{U_h(O_2)} - 1 \right)}{2 \left(\sqrt{\frac{T_c(O_2)}{T_h(O_2)}} \frac{U_c(O_2)}{U_h(O_2)} - 1 \right) + 1} \quad (3.26)$$

or, in terms of \bar{T}

$$\bar{\eta} = \frac{2 \bar{T}}{1 + \bar{T}}. \quad (3.27)$$

As an alternative, the fractional dissociation can be computed from the heights of the atomic and molecular oxygen peaks.

The atomic mass flux is given by

$$\Phi_h(O) = n_h(O) \bar{v}_h(O) m(O) \quad (3.28)$$

and the output signal is

$$U_h(O) = n_h(O) S_{qp}(O). \quad (3.29)$$

Therefore, the fractional dissociation is

$$T = \frac{1}{1 + \frac{\Phi_h(O_2)}{\Phi_h(O)}} = \frac{1}{1 + \sqrt{\frac{T_h(O_2)}{T_h(O)}} \sqrt{2} \frac{n_h(O_2)}{n_h(O)}} \quad (3.30)$$

and since the sensitivity ratio is equal to the ionization cross section ratios,

$$\frac{S_{qp}(O)}{S_{qp}(O_2)} = \frac{\sigma(O)}{\sigma(O_2)} \quad (3.31)$$

where $\sigma(O)$ and $\sigma(O_2)$ are the ionization cross sections for atomic and molecular oxygen. Thus the fractional dissociation

can be expressed as

$$T = \frac{1}{1 + \frac{1}{2} \frac{T_h(O_2)}{T_h(O)} \frac{\sigma(O)}{\sigma(O_2)} \frac{U_h(O_2)}{U_h(O)}}. \quad (3.32)$$

Similarly, the particle flux is

$$\phi_h(O) = n_h(O) \bar{v}_h(O) \quad (3.33)$$

and the relative particle flux is

$$\eta = \frac{1}{1 + \frac{\phi_h(O_2)}{\phi_h(O)}} = \frac{1}{1 + \frac{1}{2} \frac{T_h(O_2)}{T_h(O)} \frac{\sigma(O)}{\sigma(O_2)} \frac{U_h(O_2)}{U_h(O)}}. \quad (3.34)$$

The energy of the ionizing electron beam in the quadrupole ion source was obtained by a retarding potential analysis. A retarding potential curve, Figure 3.5, was obtained by changing the potential between the ion source and the quadrupole analyzer while observing the output signal of the electrometer while the instrument was tuned to mass 32. The average energy value was found to be 75 eV. The corresponding ratio of the ionization cross sections is

$$\frac{\sigma(O)}{\sigma(O_2)_{75 \text{ eV}}} = 0.77 \text{ (Fite and Brackmann, 1959)}. \quad (3.35)$$

It is noted that the mass 16 output signal $U_h^*(O)$ is the sum of $U_h(O)$ and the contribution of doubly ionized and dissociatively ionized molecular oxygen. Hence

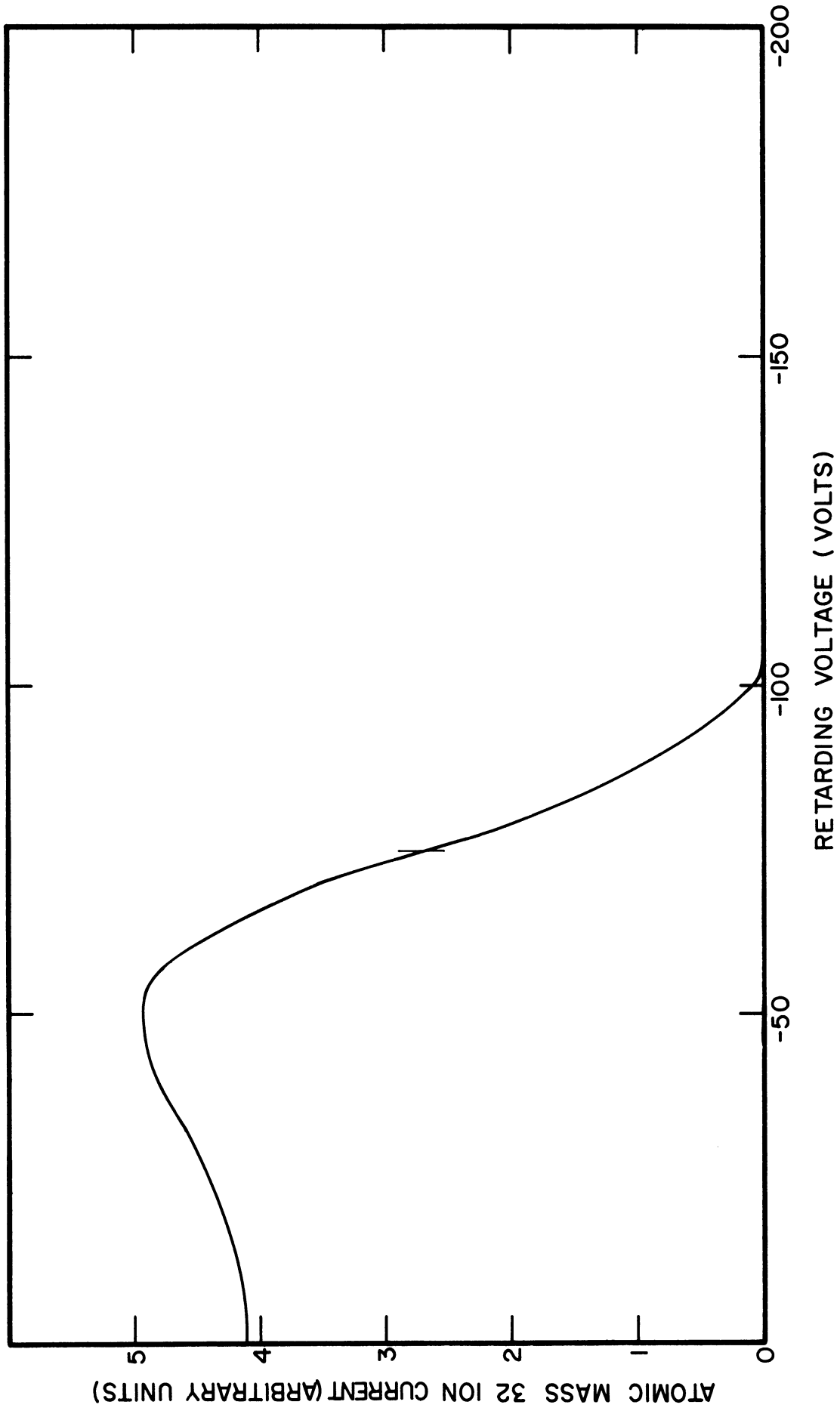


Figure 3.5 Retarding potential curve of the quadrupole mass spectrometer.

$$U_h(O) = U_h^*(O) - \frac{U_c(O)}{U_c(O_2)} U_h(O_2). \quad (3.36)$$

Agreement between the results of these two methods for computing the dissociation rate can be expected only if no oxygen is lost because of oxidation or adsorption. Since there is always some oxide formation, the rate obtained from the molecular oxygen disappearance measurement will always be larger than the rate obtained from comparing the mass 16 and 32 ion currents.

3.3.4 Determination of the Absolute Particle Flux

The absolute particle flux can be measured on the omegatron side of the beam source. Beam particles which enter the omegatron orifice collide many times with the walls of the chamber and the gauge electrodes before they enter the ionization region. Hence it can be assumed that all particles are thermally accommodated and the outgoing particle flux has an average velocity which is determined by the wall temperature. The particle density in the omegatron chamber is, therefore, proportional to the incoming flux. This is true provided that the gas is nonreactive and the pumping capacity of the vacuum system is large enough to prevent scattered particles from entering the chamber. By assuming that the condition for adequate pumping can be satisfied and that the sensitivity of the omegatron for molecular oxygen can be determined by standard calibration methods, it is possible to determine the absolute flux into the omegatron orifice for the case of

no dissociation (cold filament), as follows

$$\phi_{\Omega C}(O_2) = \frac{1}{4} n_{\Omega C}(O_2) \bar{v}_{\Omega}(O_2) \quad (3.37)$$

and

$$n_{\Omega C}(O_2) = \frac{1}{S_{\Omega}(O_2)} I_{\Omega C}(O_2). \quad (3.38)$$

Here

$\phi_{\Omega C}(O_2)$ is the cold-filament flux into and out of the omegatron,

$n_{\Omega C}(O_2)$ is the molecular oxygen density in the omegatron chamber when no dissociation occurs,

$I_{\Omega C}(O_2)$ is the ion current of the mass 32,

$S_{\Omega}(O_2)$ is the sensitivity of the omegatron for molecular oxygen, and

$\bar{v}_{\Omega}(O_2)$ is the average velocity of molecular oxygen in the omegatron chamber with characteristic temperature equal to the wall temperature.

Because of apparatus symmetry, there is a one-to-one relationship between the quadrupole and the omegatron measurement; therefore, a complete oxygen flux calibration can be obtained. When atomic oxygen is contained in the beam, it will be measurable on the quadrupole side; and unless the quadrupole sensitivity changes with time, any atom-to-molecule ratio in the beam can be determined. Hence the absolute flux at the omegatron is known for all cases.

There are several possible sources of error in this

technique. By far the largest possible error source is caused by the uncertainty of the temperature of the beam particles. Its effect on the measurement will be discussed in Section 3.5. Errors also result from any uncertainty in the relative sensitivities of the quadrupole for atomic and molecular oxygen. There are some uncertainties in the ionization cross sections (Kieffer and Dunn, 1966); the atom-to-molecule flux ratio measurement is affected by these uncertainties. The accuracy of the absolute flux measurements depends on the previous calibration and the repeatability of the omegatron system. The absolute omegatron calibration uncertainty is $\pm 25\%$ (Spencer, et al., 1965). The repeatability is better than $\pm 5\%$ (Niemann and Kennedy, 1966). The error caused by the oxygen reaction on the hot filament of the omegatron is eliminated by the pressure calibration. In any case, as shown in the next paragraph, the error so caused is negligible.

If one assumes unity dissociation efficiency on the omegatron filament surface and absorption on surfaces of all oxygen dissociated by the omegatron filament, the filament surface can be considered a perfect sink. The flow equation which relates the incoming and outgoing flux and the loss flux due to dissociation on the omegatron filament is then

$$\begin{aligned} \phi_{\Omega C}(O_2) S_{\Omega} &= \frac{1}{4} n_{\Omega C}'(O_2) \bar{v}_{\Omega}(O_2) S_{\Omega} \\ &+ \frac{1}{4} n_{\Omega C}'(O_2) \bar{v}_{\Omega}(O_2) S_{fil} \end{aligned} \quad (3.39)$$

where S_{Ω} is the orifice area of the omegatron, and

S_{fil} is the omegatron filament surface area.

The first term on the right side of Equation (3.39) is the outgoing molecular oxygen flow and the second term is the flow which forms the loss due to dissociation. The prime on the density $n_{\Omega C}'(O_2)$ is chosen to indicate that the particle density in the omegatron chamber differs from the ideal value of Equation (3.37) because of the loss term in Equation (3.39). Dividing Equation (3.39) by S_{Ω} and comparing it with Equation (3.37) above, we obtain a relation between $n_{\Omega C}(O_2)$ and $n_{\Omega C}'(O_2)$

$$n_{\Omega C}(O_2) = n_{\Omega C}'(O_2) \left(1 + \frac{S_{fil}}{S_{\Omega}}\right). \quad (3.40)$$

The filament of the omegatron is a 10-turn spiral of 0.0762 mm diameter rhenium wire wound on a 0.1 mm diameter mandril. The geometric surface area is therefore 0.0134 cm². The orifice area of the omegatron is 1.0 cm². Hence, the maximum difference between $n_{\Omega C}(O_2)$ and $n_{\Omega C}'(O_2)$ is less than 1.4%. The difference is actually considerably smaller since the filament is shielded by the surrounding electrodes which reduce the particle flux to the filament. Moreover, 100% dissociation on the omegatron filament surface is unlikely because the filament temperature is only about 2100°K.

3.3.5 Electronic Instrumentation

An electronic control unit supplied by the ATLAS Company was used with the quadrupole. The output voltage of the electrometer amplifier was recorded on an x-y recorder type Moseley 135, or for quick inspection of the mass spectra, it was displayed on a Tektronix oscilloscope type 531A. The

large gain obtained from the secondary electron multiplier permitted a scan rate of 2 scans per second. The omegatron was operated with standard test electronics. The omegatron ion current was measured with a Keithley electrometer type 417. The output voltage of the electrometer was displayed on an Electro Instruments series 500 x-y recorder. Both the quadrupole and the omegatron electrometer output voltages were recorded continuously on a two-channel Sanborn recorder type 322. All recording systems were calibrated with a Cubic V-45 digital voltmeter which was also used for direct output readings when large measurement accuracy was required.

3.3.6 The Atomic Oxygen Beam Source

It is important from all considerations to design an atomic oxygen beam source which will permit the target to intercept a large fraction of the emitted flux. The relatively large size of the target area (the orifice size of the omegatron is 1 cm^2) requires also a large cross-sectional area of the beam. Hence, the beam should be short and stubby rather than long and thin as in conventional atomic beam equipment.

A cross-sectional view of the system is shown in Figure 3.6. A filament of high purity tungsten, commercially available from the R. D. Mathis Company, is placed in the center of a double-walled titanium tube. Titanium was selected because of the low catalytic efficiency of its oxide. Cooling water flows between the tube walls to keep the surfaces at about 300°K while the tungsten filament is at 2800°K . Detailed computations of the thermal condition

are given in Appendix B. The tungsten filament is supported at each tube end by heavy copper rods. These are extensions of high current ultrahigh vacuum feedthroughs which are mounted on a standard 1½ inch Varian flange. The filament is heated with alternating current. Typical current and voltage levels for 2800°K filament temperature are 75A and 6.8V. Molecular oxygen is fed through the narrow tube in the center of the double-wall tube. The feeder tube is welded into the Varian flange on which the high current feedthroughs are mounted, and it is terminated with a Granville-Phillips variable leak. Molecular oxygen is supplied from a container via a two-stage inlet system. A liquid nitrogen cold finger in the first stage of the inlet system is used for further purification of the molecular oxygen. The assembled source is shown in Figure 3.7, and the tungsten filament position is shown in Figure 3.8. All titanium parts of the double-wall system were arc-welded in an argon atmosphere. The tube assembly was vacuum-brazed to a standard 4-inch Varian flange.

As is seen, the source is symmetric. Oxygen which enters through the narrow feeding tube in the center will collide with the hot tungsten filament and escape at one of the ends of the titanium tube. The return flux into the feeding tube is negligible because of the large difference between the inlet and exit tube diameter. Provided that the tungsten filament is kept at a high temperature ($\geq 2800^{\circ}\text{K}$) and the molecular oxygen flux is kept below 10^{18}

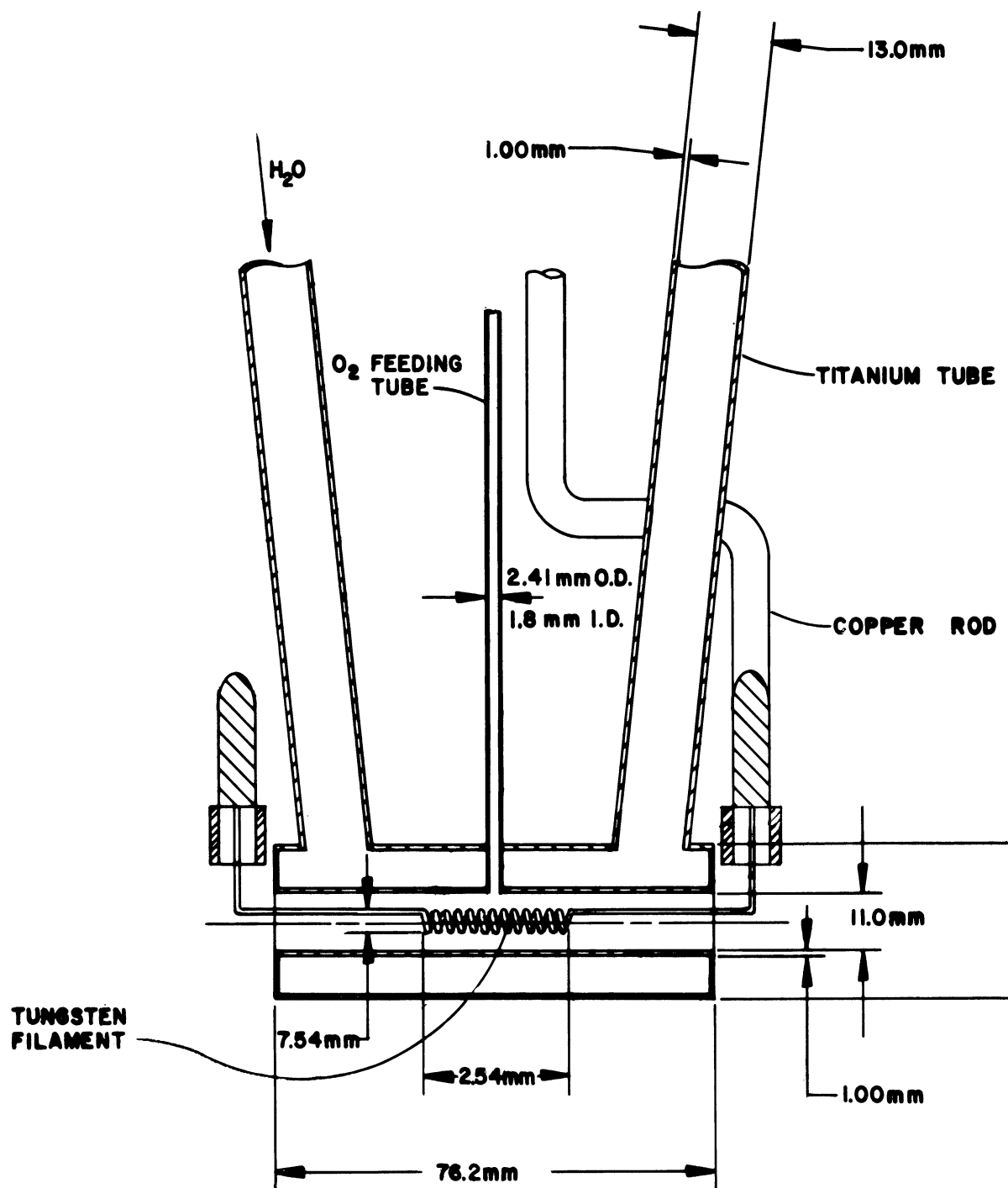


Figure 3.6 Cross-sectional view of the atomic oxygen source.

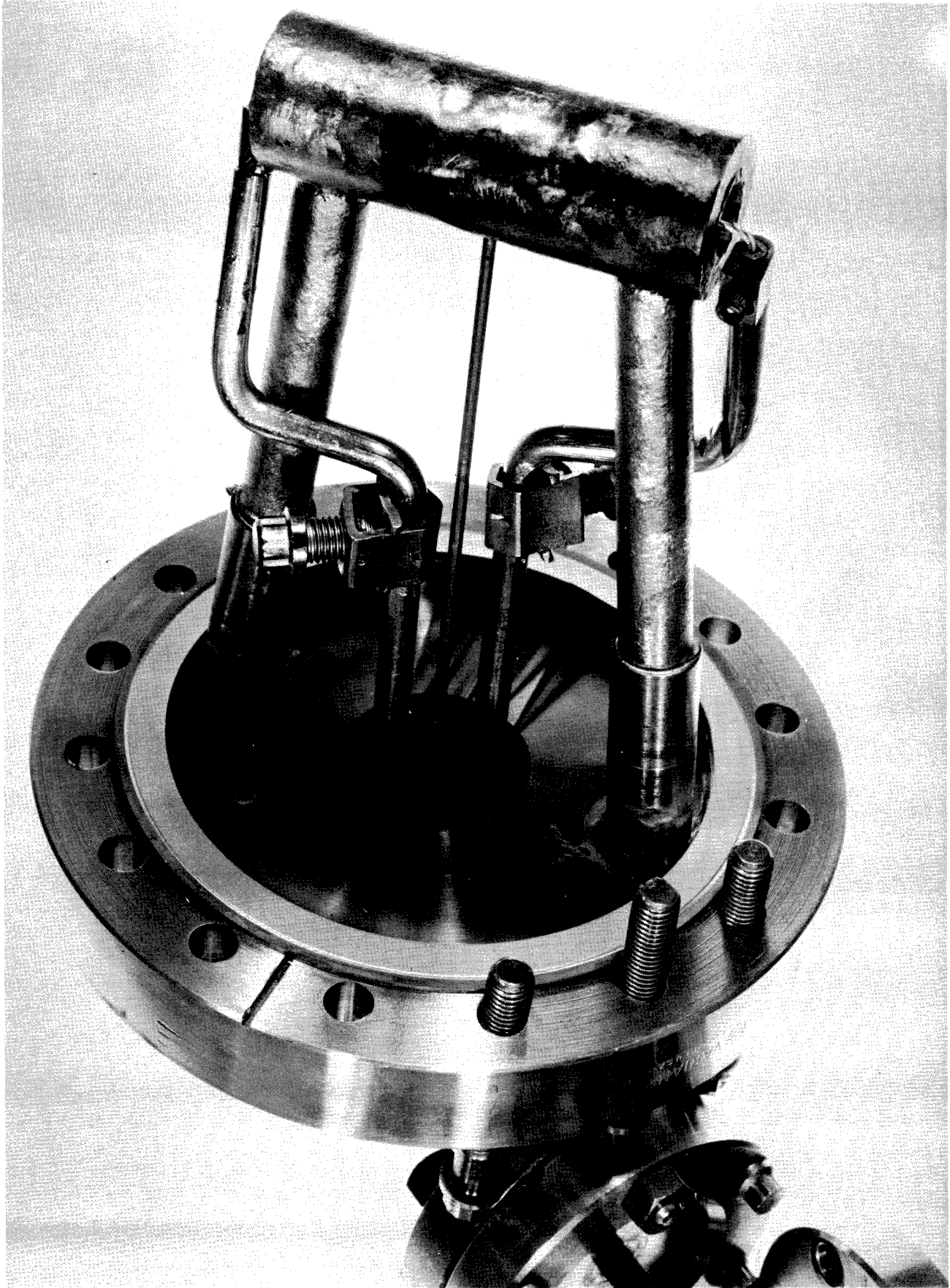


Figure 3.7 Atomic oxygen source assembly.

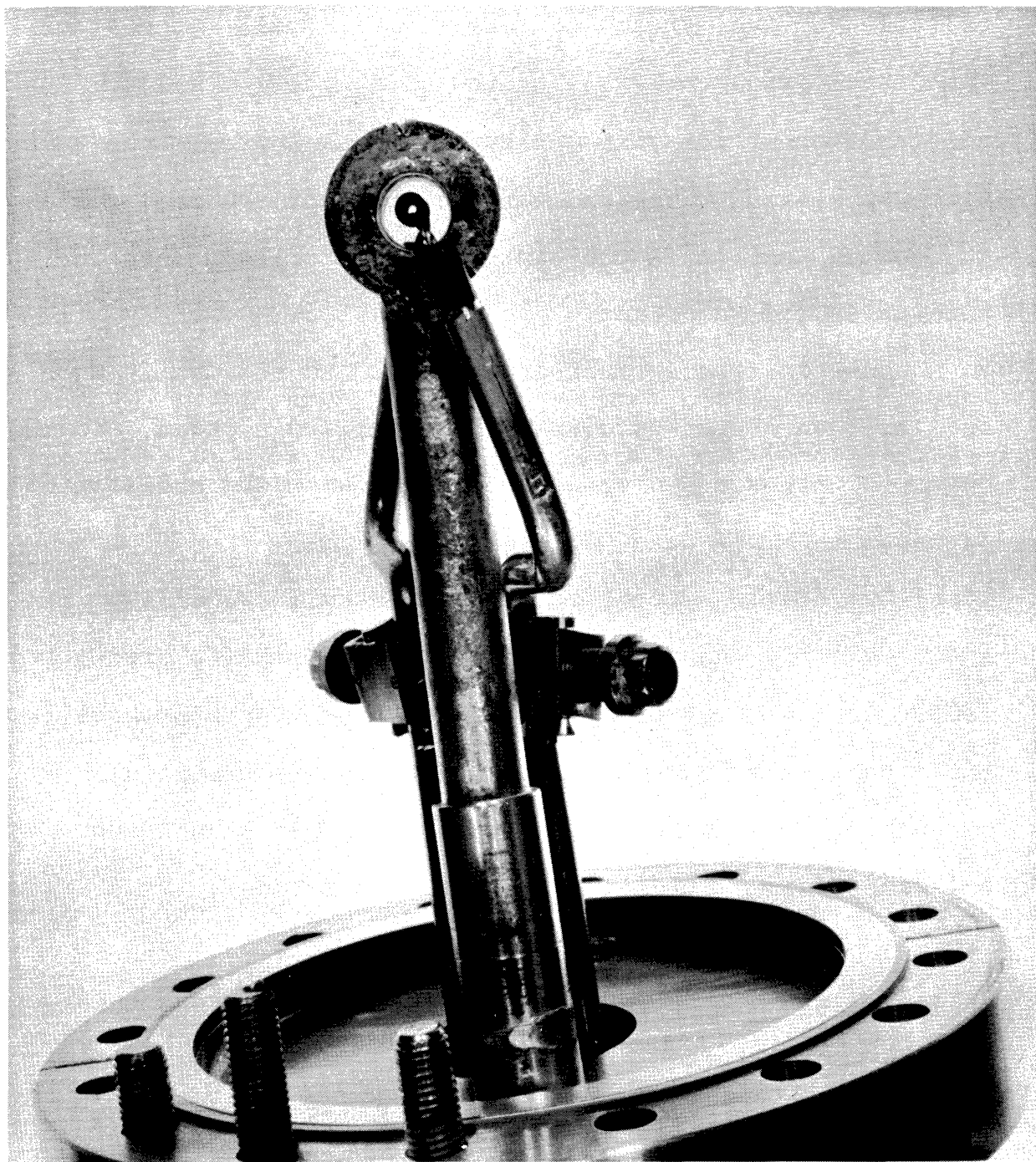


Figure 3.8 Front view of the atomic oxygen source assembly. The position of the tungsten filament is shown in the center of the double wall titanium tube.

molecules/cm²sec, the oxide formation is small and most of the formed oxide condenses on the cold titanium walls. The construction of the filament support does not permit a uniform filament heating. The ends of the filament are cooler than the coiled section in the center because of heat loss due to conduction and radiation.

However, the surface area of the end section is much smaller than the surface area of the coiled section, and the chance of atoms or molecules colliding with the end section is very small.

The beaming effect caused by the cylindrical tube is estimated from the Clausing factor. The Clausing correction factor is the ratio of the particle transmission probability for a particular geometry (i.e., a tube or a rectangular channel) to the transmission probability for an orifice with the same cross-sectional area. For short tubes, the Clausing factors are tabulated by Dushman (1962). If we think of the atomic oxygen source as a pair of independent short tubes, each having half the length of the source tube, we obtain a length to radius ratio of 6.7. The associated Clausing factor is found (Dushman, 1962, Table 2.2, p. 94) to be approximately 0.26. Clausing (1932) showed that the flux normal to the tube exit does not change with increasing tube length. The flow reduction results only from the increased collimation. Hence, the Clausing factor can be interpreted as a measure of the beam collimation factor G which is simply the inverse of the Clausing factor. Therefore we find

$$G = \frac{1}{0.26} = 3.85 \approx 3.5. \quad (3.41)$$

The collimation factor was rounded off to 3.5 because most of the particles contained in the beam originate from the tube walls and none originate directly in the tube center.

3.3.7 The Vacuum System

It was pointed out earlier that in order to reduce the flux which results from background gases, it is necessary to provide for fast gas pumping and a low ultimate pressure. The system should be free of hydrocarbons, and it should be bakeable at about 350°C. This suggests a getter ion pump system, and since it was necessary to perform the experiment with equipment already available in the laboratory, the choice was limited to a Varian 50 liter/sec ion pump supported by a Varian 400 liter/sec titanium sublimation pump.

As was discussed in Section 3.3.2, the oxygen beam must be bidirectional, one side providing the oxygen flux for the quadrupole and the other side supplying the oxygen to the omegatron system. To make all measurements meaningful, the contribution of particle flux which does not directly originate in the oxygen beam source must be negligible.

In the following discussion it is shown that, in order to obtain an adequate signal-to-background flux ratio in the omegatron and the quadrupole, a multiple stage vacuum system with a very large pumping capacity is needed.

The omegatron side is considered first. The background flux at the omegatron orifice is produced by three basic

groups of particles:

- (1) Particles which originate in the atomic oxygen source but enter the omegatron chamber only after one or more collisions with the walls of the vacuum chamber.
- (2) Particles which leave the omegatron chamber and after one or more collisions with the walls of the vacuum system reenter the omegatron chamber.
- (3) Particles which constitute a general background pressure in the vacuum system due to outgassing of the chamber walls and to small gas leaks at vacuum seals or in the walls.

Contribution of particles of the third category can be made negligible by a proper choice of the wall material and the vacuum seals. The contribution of the first category is determined by the focusing properties of the oxygen source and by the pumping speed of the vacuum system. The contribution of the second group is determined only by the pumping speed of the vacuum system.

In considering first a single stage vacuum system it is assumed that the pumping speed of 400 liter/sec of the titanium sublimation pump can be maintained and that the omegatron chamber is located 10 cm from the source. The signal-to-background flux ratio can be computed as follows. The signal flux into the omegatron is given by

$$\phi_{\Omega} = \phi_s G \frac{\Omega}{\pi} \quad (3.42)$$

where ϕ_s is the flux at the atomic oxygen source exit, and
 G is the gain due to the focusing effect of the titanium tube.

The background flux into the omegatron chamber which consists of contributions of particles from groups 1 and 2 mentioned on page 104 is

$$\phi_{bg} = \frac{1}{4} n_{bg} \bar{v}_{bg} \quad (3.43)$$

where n_{bg} is the particle density in the vacuum chamber surrounding the source and

\bar{v}_{bg} is the average velocity of these particles.

The condition of continuity requires that all particles which leave the source ultimately be removed by the vacuum pump.

Hence we have

$$2 \phi_s S_o = n_{bg} P \quad (3.44)$$

where S_o is the area of the source, and

P is the pumping speed of the vacuum pump.

The factor two on the left side results from the fact that the source is bidirectional. The signal-to-background flux ratio is now obtained as

$$\frac{\phi_\Omega}{\phi_{bg}} = \frac{\phi_s G \frac{\Omega}{\pi}}{\frac{1}{4} n_{bg} \bar{v}_{bg}} = \frac{1}{2} G \frac{\Omega}{\pi} \frac{P}{\frac{1}{4} S_o \bar{v}_{bg}}. \quad (3.45)$$

For numerical values to be employed in the system as first conceived, we have

$$G = 3.5 \quad (3.46)$$

$$\frac{\Omega}{\pi} = 3.18 \times 10^{-3} \quad (3.47)$$

$$P = 400 \text{ liter sec}^{-1} = 4 \times 10^5 \text{ cm}^2 \text{sec}^{-1} \quad (3.48)$$

$$S_O = 1 \text{ cm}^2 \quad (3.49)$$

and at 300°K

$$\bar{v}_{bg} \approx 4 \times 10^4 \text{ cm sec}^{-1}. \quad (3.50)$$

Therefore

$$\frac{\phi_{\Omega}}{\phi_b} = \frac{1}{2} 3.5 \times 3.18 \times 10^{-3} \times \frac{400}{10} = 0.223. \quad (3.51)$$

This ratio is too low so that changes from the first conception were necessary.

Mechanically it is difficult to place the omegatron chamber closer to the source exit. Improvement could be obtained only by increasing the effective pumping speed. Since the system is to be operated only in oxygen and nitrogen, increased titanium getter pumping should be adequate. Therefore, the oxygen source was placed directly in the titanium sublimation pump housing. Active titanium can be deposited in the source-surrounding walls. Most of the oxygen emitted from the source will strike titanium-activated surfaces directly; the pumping speed is now limited only by the sticking probability of oxygen on these activated walls. At room temperature the sticking probability of oxygen on continuously deposited titanium is approximately 0.65. It increases to near unity at liquid nitrogen temperatures (Clausing, 1962).

Theoretical calculations of the effective pumping speed of the system as so modified are not very meaningful because of complex geometry and the uncertainty in the knowledge of the particle collision distribution. Consequently, the signal-to-background flux ratio was measured. An omegatron chamber was mounted opposite one side of the source face at a distance of approximately 10 cm. A small mechanical shutter was placed so that the direct particle flow from the source to the omegatron chamber could be intercepted, and only particles which contribute to a background flux from group 1 mentioned on page 104, can enter the omegatron chamber. After a constant oxygen flux was established (molecular oxygen only) and after the pump was operated at its maximum capacity by continuous evaporation of titanium, the oxygen density in the omegatron system was measured with the shutter in open and closed position. The measured density ratio was approximately 10. During the test the outside walls of the titanium pump were kept at room temperature. A considerable improvement can be expected if the walls are cooled to liquid nitrogen temperature. However, mechanical difficulties make this impractical. Thus this modification was not adequate.

To improve the signal-to-background flux ratio required a second pumping stage with high pumping capacity. A titanium sublimation pump with liquid nitrogen cooled walls served this purpose. An ion pump was not available for removal of the nonreactive gases, but no serious problem arose because the major contaminants in the molecular oxygen

which cannot be removed by chemical pumping are helium, argon, and methane. Argon and methane condense easily on liquid nitrogen cooled surfaces and small amounts of helium do not interfere with the adsorption measurements.

A cross-sectional view of the stainless steel getter pump is shown in Figure 3.9. A double-walled design with 0.64 cm spacing between the walls was chosen to permit effective cooling by flowing liquid nitrogen through the space between the inner and the outer walls. Titanium is evaporated from a tungsten-titanium filament. The filament is wound into a spiral and mounted on a standard 1.5 inch Varian high-current feedthrough. It is necessary to build the pump short and stubby in order to keep the omegatron close to the source. The total pump length is 8.26 cm. The inside diameter is 14.0 cm and the wall material is 0.08 cm stainless steel type 304. All parts are arc-welded in an argon atmosphere. Entrance and exit parts are terminated with standard 1.5 inch Varian flanges. In order to reduce the conductance between the pump and the source and to collimate the flux, a 1.0 cm^2 orifice was placed between the flanges on the source side of the pump. A Bayard-Alpert type ionization gauge was mounted on the pump to permit a measurement of the background pressure in the pump space.

Since all pump surfaces are cooled to liquid nitrogen temperatures and most of the inside surfaces are in line of sight with the titanium filament, it is expected that the gas particles in the pump will condense after the first or

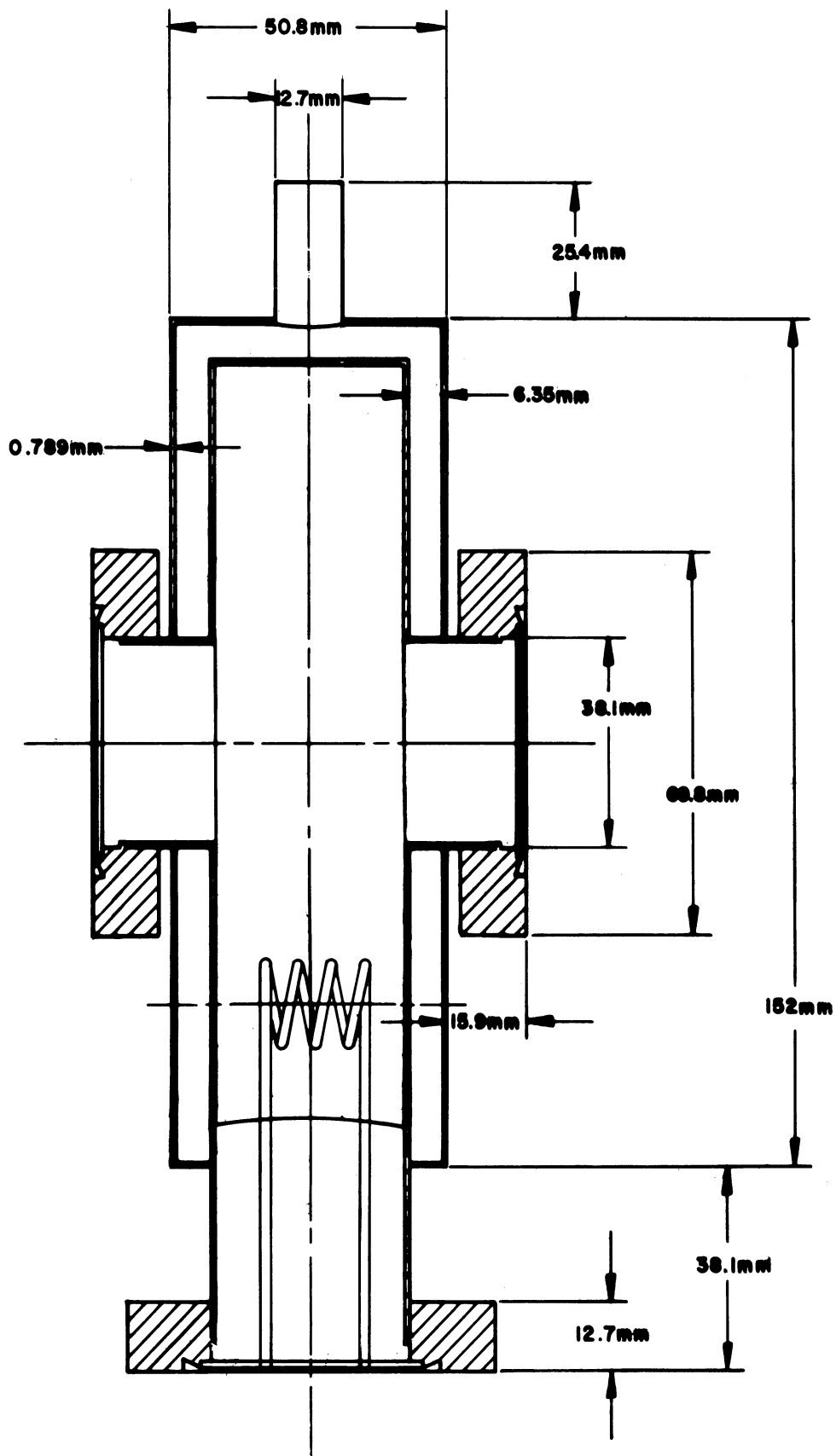


Figure 3.9 Cross-sectional view of the titanium getter pump.

second collision with the cold walls, and thus provide a very low background flux for the omegatron. This was confirmed in the experiment. Starting with a background pressure in the vacuum system of approximately 5×10^{-10} torr, a molecular oxygen flow was produced so that the measured molecular oxygen density in the omegatron corresponded to 2×10^{-6} torr. At the same time the pressure in the ionization gauge rose to 7×10^{-10} torr. Although it is not possible to make accurate measurements of molecular oxygen pressure with Bayard-Alpert ionization gauges, an order-of-magnitude measurement can easily be obtained.

Having established that the contribution to the flux into the omegatron caused by all background gases (groups 1, 2, and 3) in the getter pump are negligible, we still must consider the contribution of the background gas of group 1 in the source chamber to the particle flux into the omegatron. The signal flux is lower now than the flux calculated previously because the distance between the source and the omegatron orifice has increased from 10 cm to 19 cm. Therefore the signal flux attenuation between the source exit and the omegatron orifice is

$$G \frac{\Omega}{\pi} = 3.5 \frac{1}{19^2 \pi} = 3.09 \times 10^{-3}. \quad (3.52)$$

The distance from the source to the first orifice at the getter pump entrance is 9.0 cm. Hence the fraction of the source flux which enters the getter pump is

$$G \frac{\Omega_P}{\pi} = 3.5 \frac{1}{9^2} = 1.38 \times 10^{-2}. \quad (3.53)$$

If one assumes that the signal-to-background flux into the getter pump is again 10 as measured before with the omegatron, and the spatial background flux distribution follows the cosine law, the background flux into the omegatron chamber is

$$\phi_{bg}' = \frac{1}{10} 1.38 \times 10^{-2} \frac{1}{10^2 \pi} \phi_S = 4.4 \times 10^{-6} \phi_S. \quad (3.54)$$

The signal-to-background ratio is therefore

$$\frac{\phi_{\Omega}}{\phi_{bg}'} = \frac{3.09 \times 10^{-3}}{4.4 \times 10^{-6}} = 7 \times 10^2 \quad (3.55)$$

which is adequate.

The quadrupole side was arranged similarly to the omegatron side. A getter pump identical to the pump on the omegatron side was placed between the source and the quadrupole. As mentioned before, a narrow collimated particle beam must be formed and directed through the center hole of the quadrupole ion source. It is important that only beam particles be ionized in the quadrupole; since the ion source does not strictly discriminate between direct beam particles and particles which have made collisions with the walls of the ion source, a large signal-to-background ratio is required. The largest acceptable beam diameter is determined by the size of the center opening of the quadrupole ion source which is 0.0314 cm^2 . Thus two apertures of the same size were placed

between the beam source and the quadrupole ion source. The first aperture was mounted between the flanges which connect the beam source and the getter pump. The second aperture was mounted in the center of the getter pump. The first aperture provides a clear separation between the source and the detection system.

The position of the second aperture permitted efficient pumping on both sides by the evaporated titanium. Oxygen-free copper was used instead of stainless steel to assure more efficient cooling of the aperture surface. Both aperture hole positions were adjustable to permit exact lineup with the ion source center. The getter pump with the separation orifice mounted in the Varian flange is shown in Figure 3.10. A third pump, needed to evacuate the ion source and analyzer section of the quadrupole, was connected to the system through a conductance of about 10 liter/sec. The pump was identical to the pump used for evacuation of the oxygen source region. The reduction in speed due to the small conductance of the connecting tube was dictated by the geometry of the quadrupole housing. The effect of scattered particles in the quadrupole ion source was discussed in Section 3.3.2. Contributions of background particles from the getter pump and the beam source chamber are negligible. Pressure measurements with the ionization gauge on the getter pump showed no pressure change when the oxygen flux was changed from zero to a level equivalent to an omegatron pressure of 5×10^{-6} torr. The indicated ionization gauge pressure was 8×10^{-10} torr.

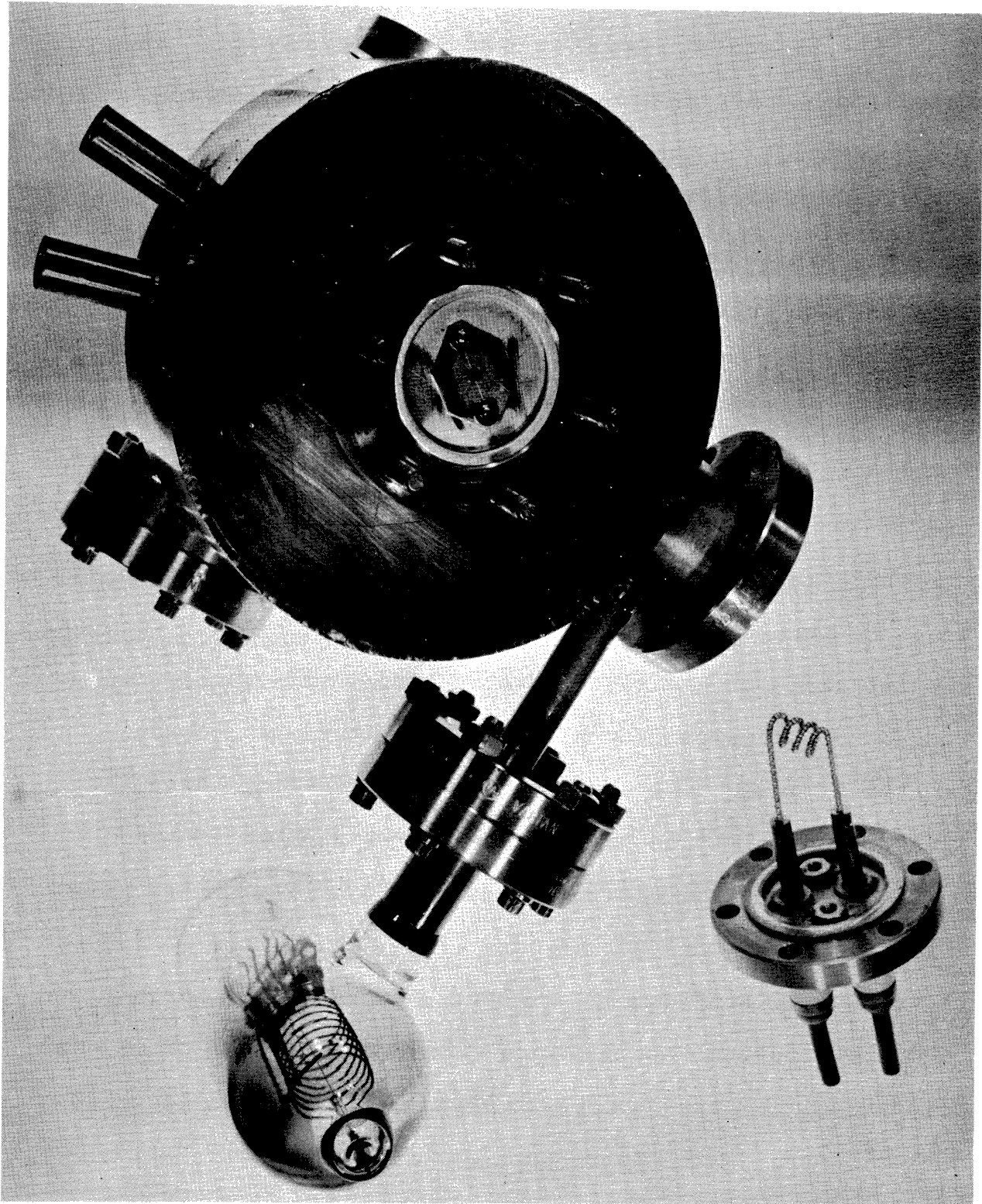


Figure 3.10 Double wall titanium getter pump with ionization gauge and disassembled titanium filament.

3.3.8 System Assembly and Preparation

The assembled system is shown in Figure 3.11. The omegatron and its getter pump are shown on the right side and the quadrupole on the left. The quadrupole getter pump block is connected to the source chamber via a short stainless steel bellows. This construction allows the movement of the quadrupole section relative to the oxygen source and permits a measurement of the oxygen beam shape. AC power is supplied to the tungsten filament at the center top flange on which the high current feedthroughs are mounted. The double-wall source is cooled with ordinary tap water. The shutter is controlled mechanically with a Varian rotary feedthrough and it is designed to intercept alternately the particle flow on the two sides of the source exit. Liquid nitrogen is fed to the getter pumps from a 25-liter Dewar flask. Conducting the overflow from the pump to the surface of the 400 liter/sec sublimation pump of the source chamber improved the pumping capacity of the pump considerably. The getter pumps were thermally isolated with styrofoam. With this configuration, 20 liters of liquid nitrogen permitted one hour of continuous operation. There is a potential danger of oxygen condensing from the atmosphere onto the outside walls of the getter pumps. With the reduced air flow and the relative short operating time, this possibility was not considered serious.

For initial testing of the oxygen system the omegatron with its getter pump was removed and a pyrex window was

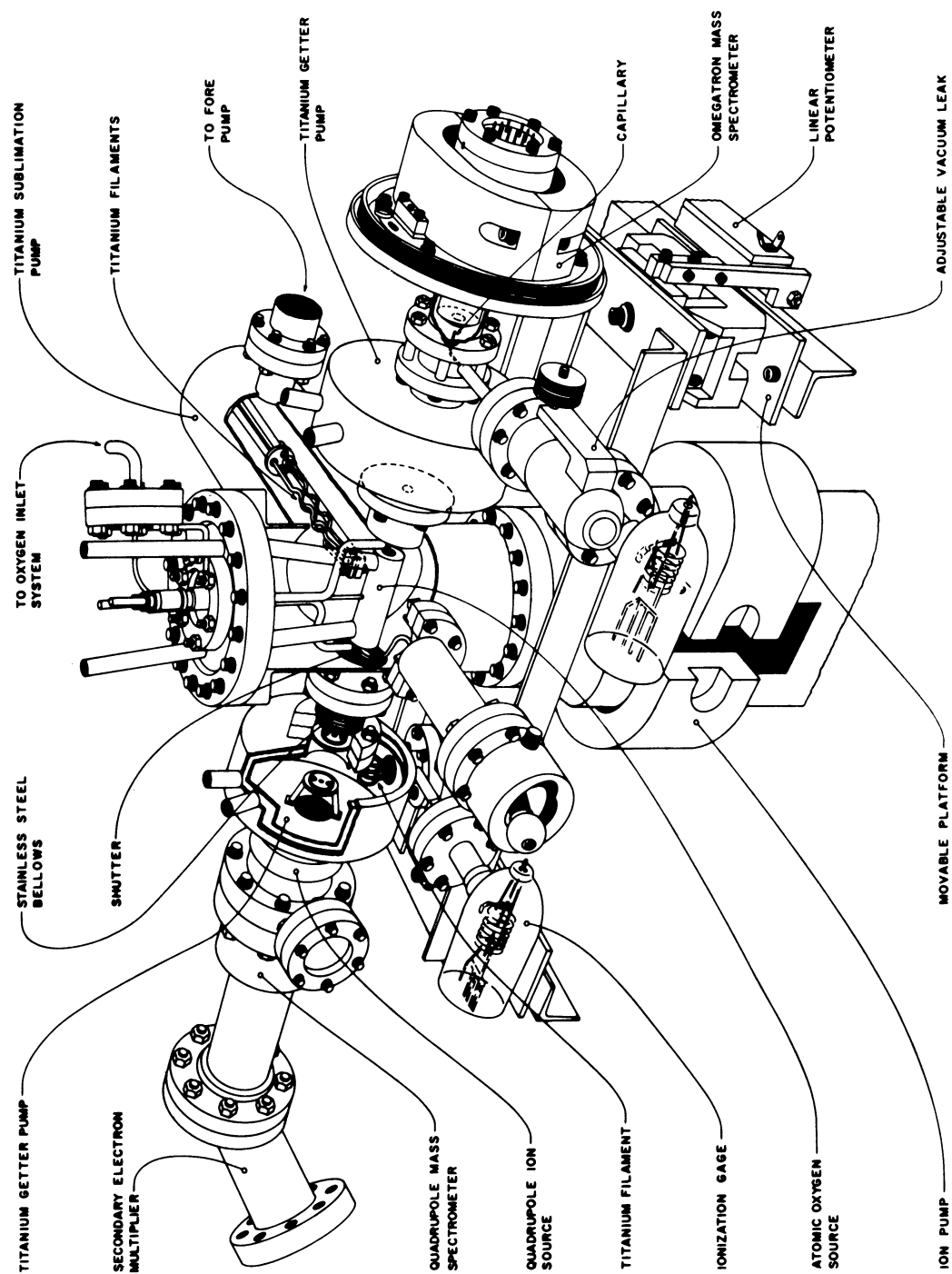


Figure 3.11 Atomic oxygen beam system (complete assembly).

mounted on the flange to allow direct optical inspection of the tungsten filament and the source chamber. After the initial heating of the filament for outgassing and settling, a calibration was performed to relate the filament temperature to the applied ac voltage and current. The temperature was measured with an optical pyrometer (Leeds and Northrup Model 8632-C). Temperature readings were obtained from the inside surface of the filament. The inside area was assumed to be a true hohlraum with unity emissivity. No temperature corrections were made for the transmission of the pyrex window. The filament voltage was measured with a voltmeter (B and K Model 120). The results are plotted and shown in Figure 3.12. The absolute accuracy of the calibration is estimated to be about $\pm 5\%$. This does not take into account the thermal gradient due to conduction cooling near the ends of the filament. At an operating temperature of 2800°K the temperature difference between the center and the end of the filament was about 100°K . This should be a maximum value since the end section of the filament cannot be considered a true hohlraum.

Repeatability of the voltage temperature calibration was good. Several calibrations yielded identical data. The calibration was repeated after several weeks of operation and a temperature change of approximately 5% was observed, which called for use of a larger filament voltage and indicates an increased filament resistance. A gradual increase of the filament resistance with time can be expected because small

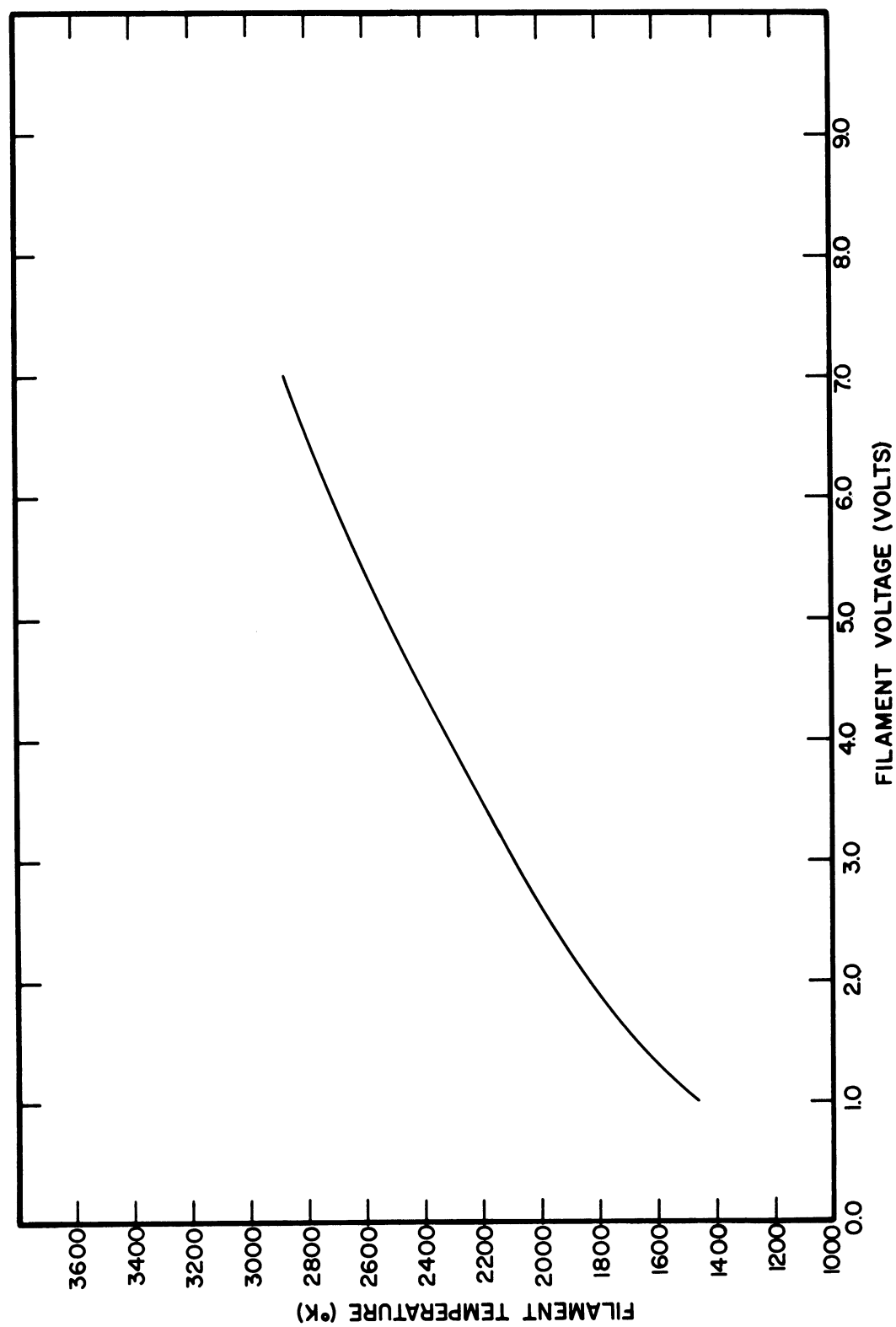


Figure 3.12 Tungsten filament temperature versus filament voltage.

amounts of tungsten are continuously carried away from the filament by the tungsten oxide which forms on the surface of the filament. However, the measured voltage change was so small during the time interval of several weeks, that quantitative determinations of the amount of tungsten lost were masked by other uncertainties of the measurement.

Since no optical inspection is possible when the omega-tron and the quadrupole are mounted on the system, all quoted filament temperatures are obtained from the temperature-voltage calibration curve. It should be noted that the exact value of the filament temperature need not be known, because it serves merely as an aid to check the measured data with those theoretically predicted. The oxygen flux and the ratio of atomic to molecular oxygen in the beam were measured directly during each test.

To condition the surface of the titanium tube and to decarbonize the tungsten filament, oxygen was admitted to the system and then the tungsten filament heated to 2800°K. The oxygen flux was adjusted so that the ionization gauge monitor on the main vacuum system indicated a pressure of 1×10^{-6} torr. Titanium pumping and liquid nitrogen pumping were not employed. Under this condition the system was operated for several hours; it was expected that after this the titanium tube wall would be covered with several layers of titanium and tungsten oxides when the conditioning was terminated. Optical inspection of the tube walls showed a change in the surface color from a silver grey appearance

to a milky grey color. No direct surface analysis was performed. Mass spectra which were taken with the quadrupole during this time showed argon, carbon monoxide, and methane. The carbon monoxide and carbon dioxide were probably formed by the carbon contained in the tungsten. Argon and some methane entered the vacuum system as contaminants in the molecular oxygen. Since argon can only be pumped by the ion pump with a reduced efficiency, the argon background will be considerably higher than the small impurities in the oxygen would suggest. Large amounts of methane and hydrogen are released by the titanium filament during the initial outgassing. Hydrogen is rapidly pumped by the getter action of the subsequently evaporated titanium, but methane is removed only by the ion pump.

After the initial tests and temperature calibration the omegatron was reinstalled, and after a 48-hour bakeout at 350°C, with subsequent outgassing of all filaments and ionization gauges, the system was operational. The indicated system pressure was 5×10^{-10} torr. This value decreased to 3×10^{-10} torr after the getter pumps were cooled with liquid nitrogen and the titanium getter activated.

3.4 BEAM STUDIES

3.4.1 Flux Dependence of the Fractional Dissociation

After the initial preparation of the system, a number of atomic oxygen flux measurements were made over several decades of flux levels in the manner described in the next few sentences. A desired molecular oxygen level was set by means of the variable leak at the oxygen inlet system. The absolute value was obtained from the omegatron reading. Data were recorded from both mass spectrometers for atomic and molecular oxygen. Then the tungsten filament was heated to 2800°K and the decrease in the molecular oxygen was observed. After the flow stabilized, which required approximately 10 sec, a second sequence of mass 16 and 32 measurements were made. The tungsten filament was then cooled again and the initial flux measurement was repeated. During the measurements the shutter was alternately opened and closed to avoid errors resulting from zero-drift of the electrometer amplifiers. All output signals were recorded for at least 20 sec per data point. This sequence of measurements was repeated for several flux values, and the fractional dissociation was computed as outlined in Section 3.3.3.

The results are shown in Figure 3.13. The fractional dissociation due to the hot tungsten filament surface is plotted versus the molecular oxygen flux measured at the omegatron when the tungsten filament is cold. The dashed line is the apparent dissociation computed from the disappearance of the molecules. The solid lines are the fractional

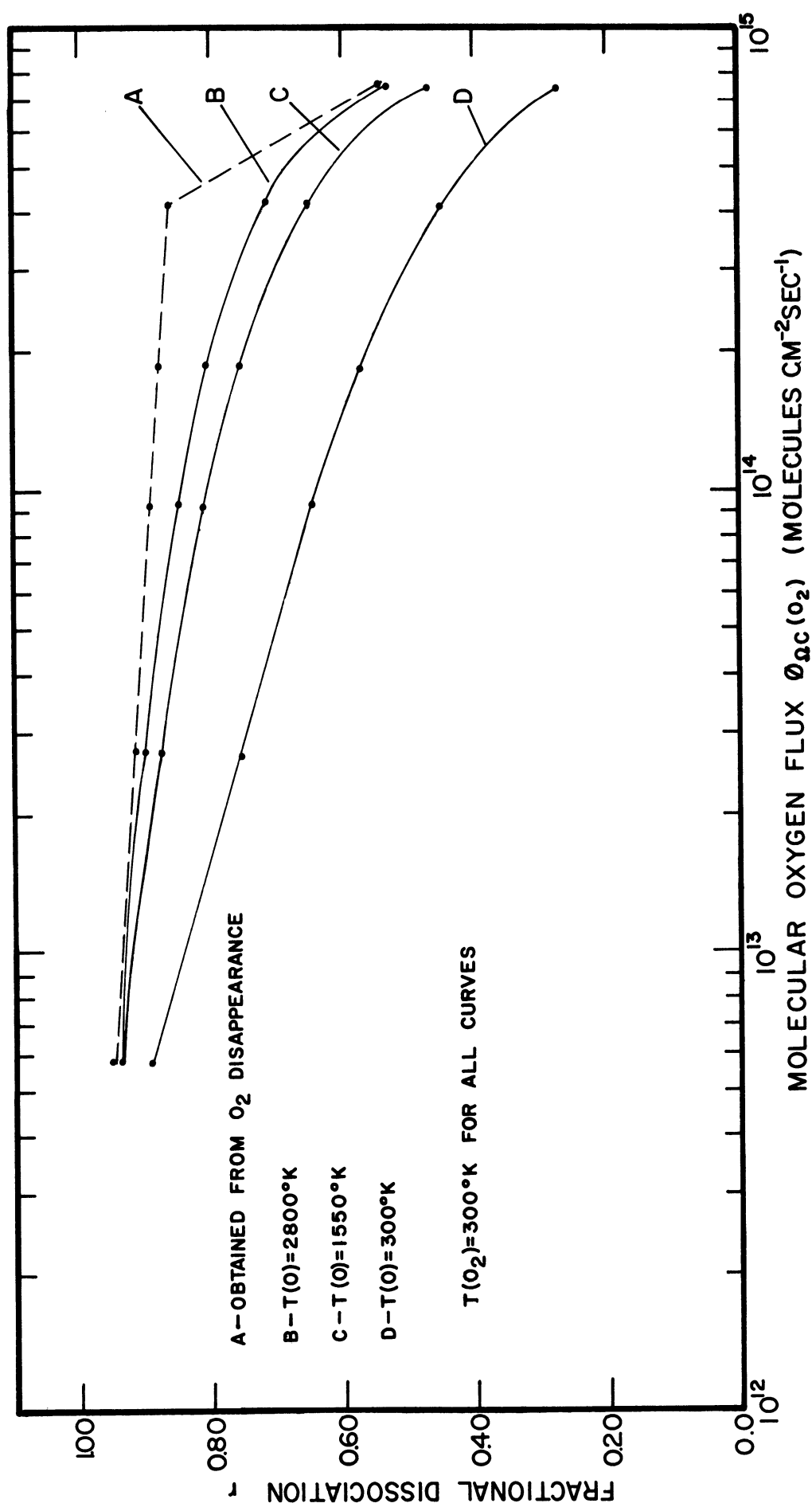


Figure 3.13 Fractional dissociation versus molecular oxygen flux as measured at the omegatron orifice.

dissociation computed according to Equation (3.32) of Section 3.3.3. Curve B applies for an assumed atomic oxygen temperature of 2800°K; curve C was obtained by assuming that the kinetic temperature of the atomic oxygen is equal to the arithmetic average of the filament temperature and the wall temperature of the surrounding tube. The wall temperature is assumed to be 300°K, so that the assumed kinetic temperature is 1550°K. Curve D is computed by assuming that the kinetic temperature of the atomic oxygen is equal to the wall temperature of the titanium tube. In all cases the kinetic temperature of the molecular oxygen is assumed to be 300°K.

As is seen from the curves of Figure 3.13, a major difficulty is caused by the uncertainty in the kinetic temperature of the beam particles. Curves B and D represent the extreme cases.

The difference between the value obtained from the molecular oxygen disappearance and the atomic and molecular oxygen ion current ratios indicates a loss of oxygen with increasing flux. This is in accord with the theory which predicts an increase in relative oxide formation with increasing oxygen flux.

3.4.2 Demonstration from Mass Spectra of Production of a Beam Primarily Consisting of Oxygen Atoms

Most of the presented data were obtained by tuning the quadrupole spectrometer and the omegatron sequentially to molecular and atomic oxygen, each for a relatively long time interval (20 sec). It was also important to take

continuous mass spectra to check the gas composition in the beam. A fast survey scan is normally obtained by displaying the output of the quadrupole electrometer amplifier on an oscilloscope and by scanning the spectrometer at a rate of 50 atomic mass units/sec. For permanent recordings the scan rate is reduced to 0.5 mass units/sec and the output of the electrometer amplifier is recorded with an x-y recorder.

A typical set of quadrupole mass spectra taken with the tungsten filament at room temperature, thus without dissociation, is shown in Figures 3.14a, 3.14b, and 3.14c. This is a control set of data, for comparison with data under dissociative conditions. The first spectrum in the sequence (Figure 3.14a) is the background spectrum. The second spectrum (Figure 3.14b) was obtained when molecular oxygen was introduced into the system, and the third scan (Figure 3.14c) was obtained with the shutter closed. It can be seen by comparing Figures 3.14a and 3.14b that the background does not change when molecular oxygen is introduced. The small mass 16 peak in Figure 3.14b is caused by doubly ionized and dissociatively ionized molecular oxygen. The ratio of the mass 16 to 32 peak heights is constant for a fixed set of quadrupole operating parameters. The apparent large height of the hydrogen peak is a result of interference of the background noise with the signal. Because the width of the hydrogen peak is very small, allowing only a short time for measurement, constructive and destructive interference with background noise occurs and results in a large fluctuation of the output signal.

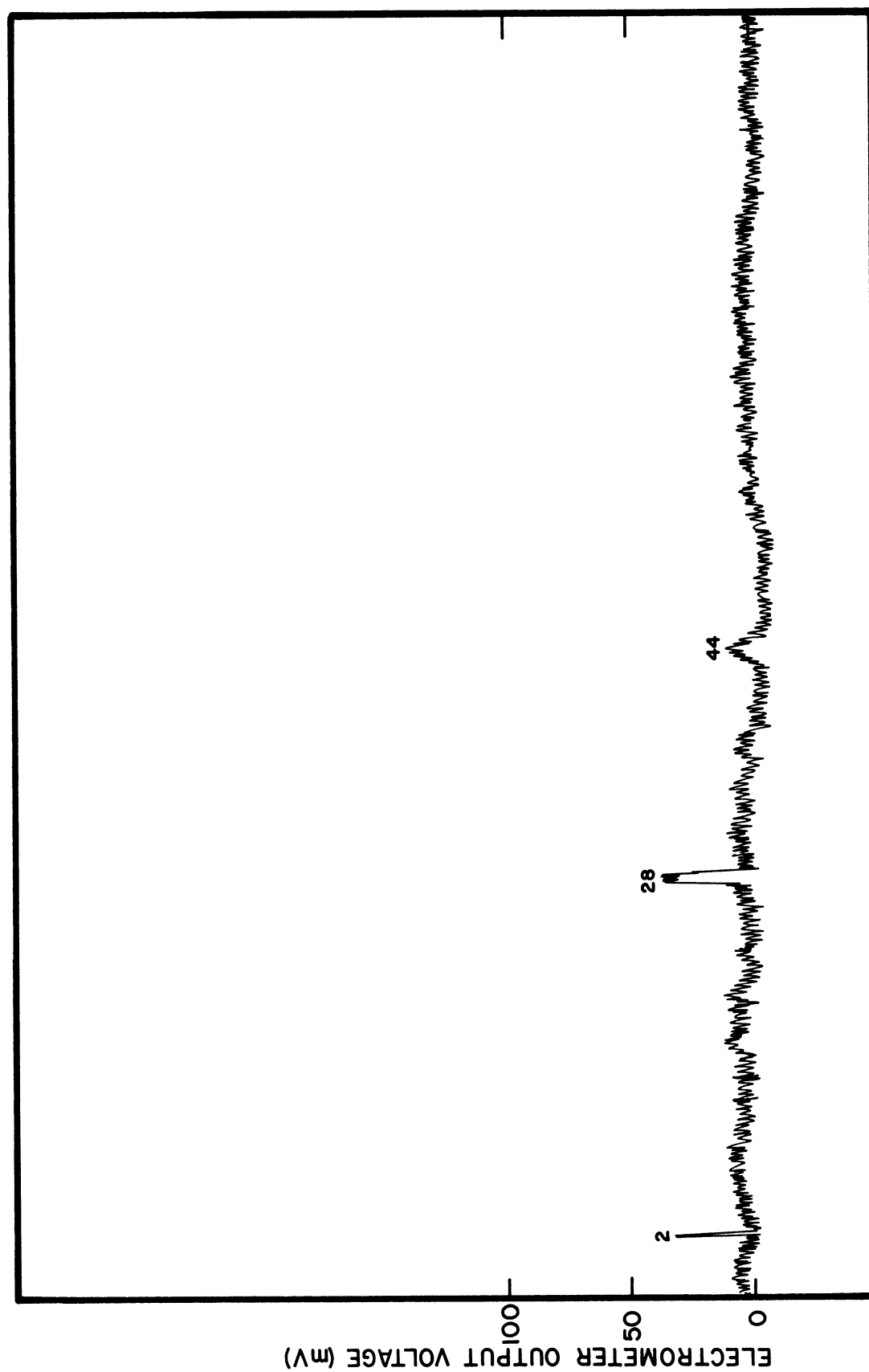


Figure 3.14a Quadrupole mass spectra, tungsten filament at room temperature with background gases only.

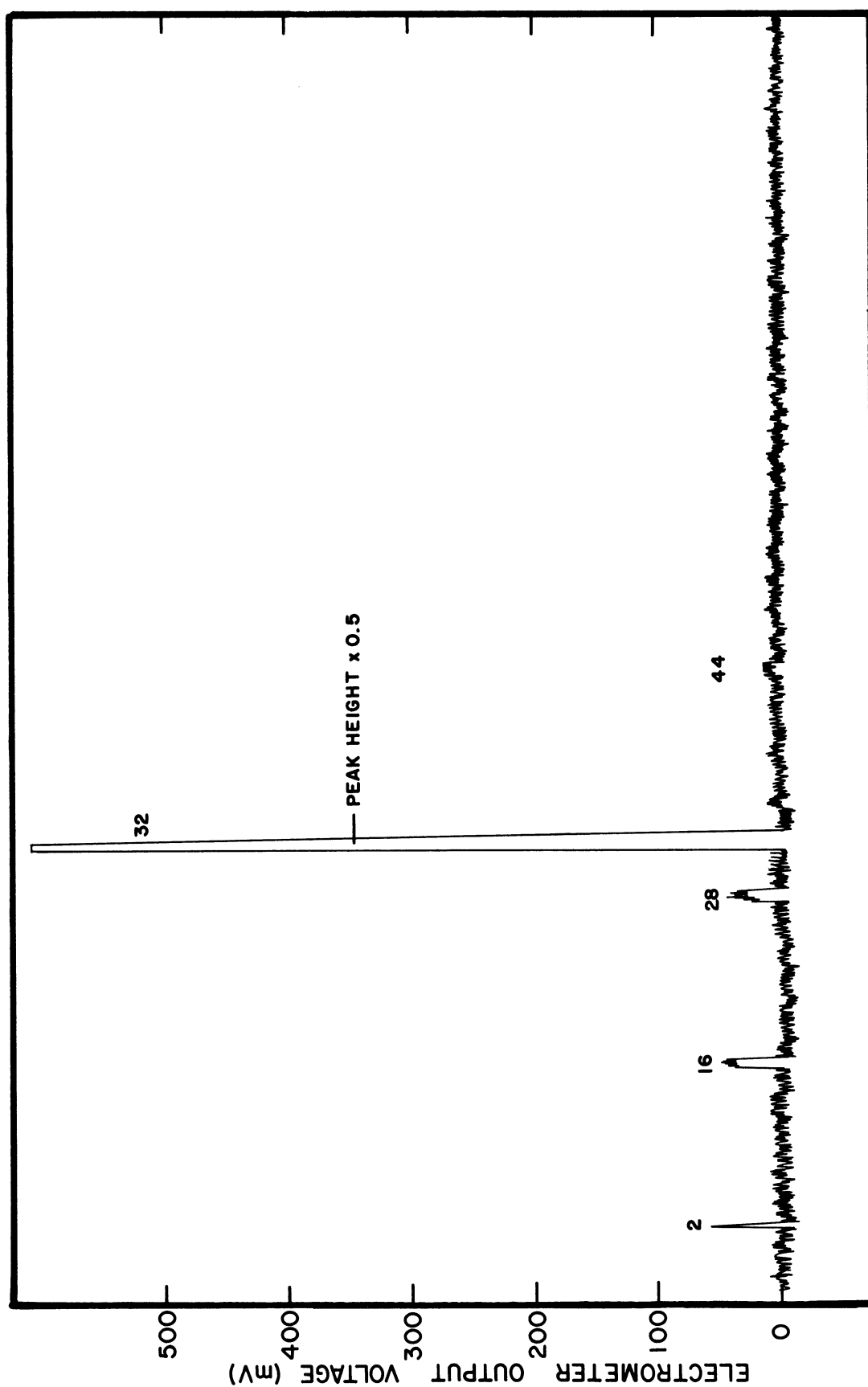


Figure 3.14b Quadrupole mass spectra, tungsten filament at room temperature with a molecular oxygen flux of 10^{14} molecules $\text{cm}^{-2}\text{sec}^{-1}$ at the omegatron orifice, and with the shutter open.

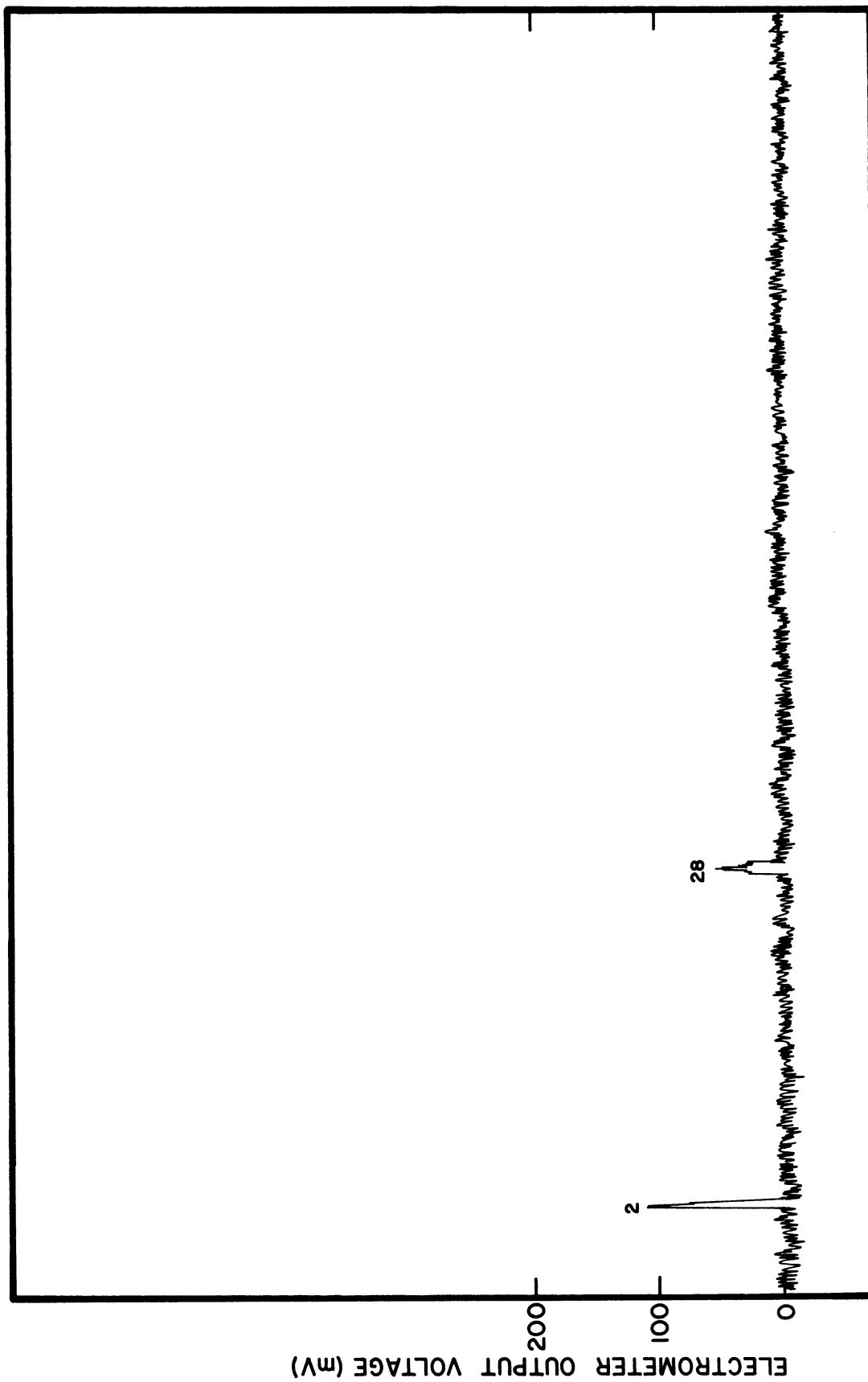


Figure 3.14c Quadrupole mass spectra, tungsten filament at room temperature with a molecular oxygen flux of 10^{14} molecules $\text{cm}^{-2}\text{sec}^{-1}$ at the omegatron orifice, and with the shutter closed.

A typical set of quadrupole mass spectra taken when the tungsten filament was heated to about 2800°K is shown in Figures 3.15a and 3.15b. The trace in Figure 3.15a was obtained when the shutter was open and the trace in Figure 3.15b when the shutter was closed. In comparing both spectra the presence of a beam consisting primarily of atomic oxygen is clearly indicated in Figure 3.15a. As expected in going from the cold filament spectrum of Figure 3.14b to the hot filament spectrum of Figure 3.15a, the molecular oxygen peak is very markedly lowered and the atomic oxygen peak greatly heightened. The fact that the height of the atomic oxygen peak when the filament is heated, is substantially lower than that of the molecular oxygen peak when the filament is cold, although the molecular oxygen leak rate was kept constant in the test sequence, is due to the fact that only beam particles are ionized in the quadrupole source and that the kinetic temperature of the oxygen atoms is expected to be near the temperature of the tungsten filament. Thus the oxygen atoms move through the ionization region with a much higher speed than the oxygen molecules in the case when the tungsten filament is cold. Consequently the instantaneous atomic oxygen particle density is much less when the filament is heated than the instantaneous molecular oxygen particle density when the filament is cold. Two offsetting factors are that the ionization cross section ratio of atomic to molecular oxygen for 75 eV electron energy is 0.77, and that each molecule produces two atoms. Again in Figure 3.15b as in Figure 3.14c

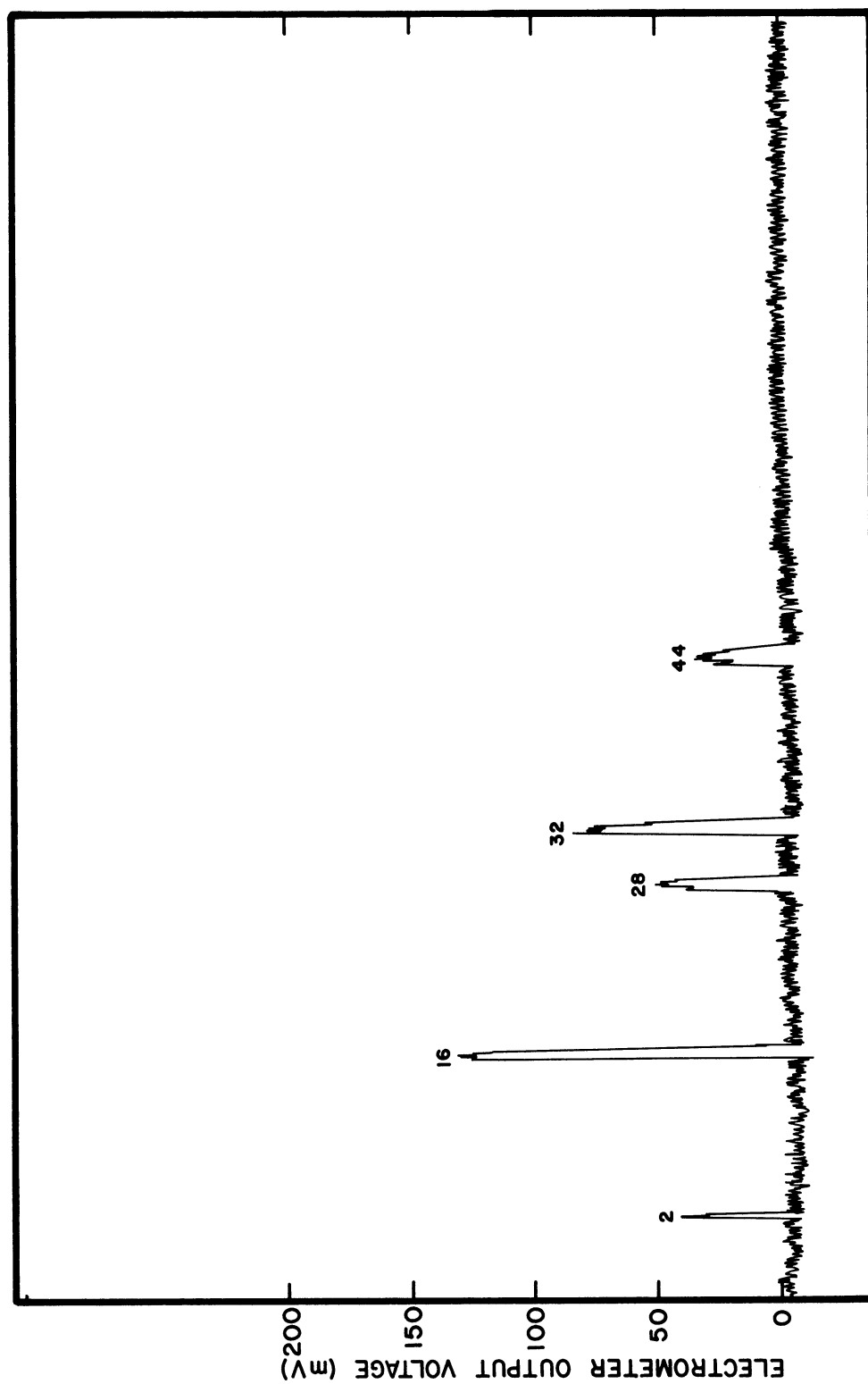


Figure 3.15a Quadrupole mass spectra, tungsten filament at 2800°K with a molecular oxygen flux of 10^{14} molecules $\text{cm}^{-2}\text{sec}^{-1}$ at the omegatron orifice and with the shutter open.

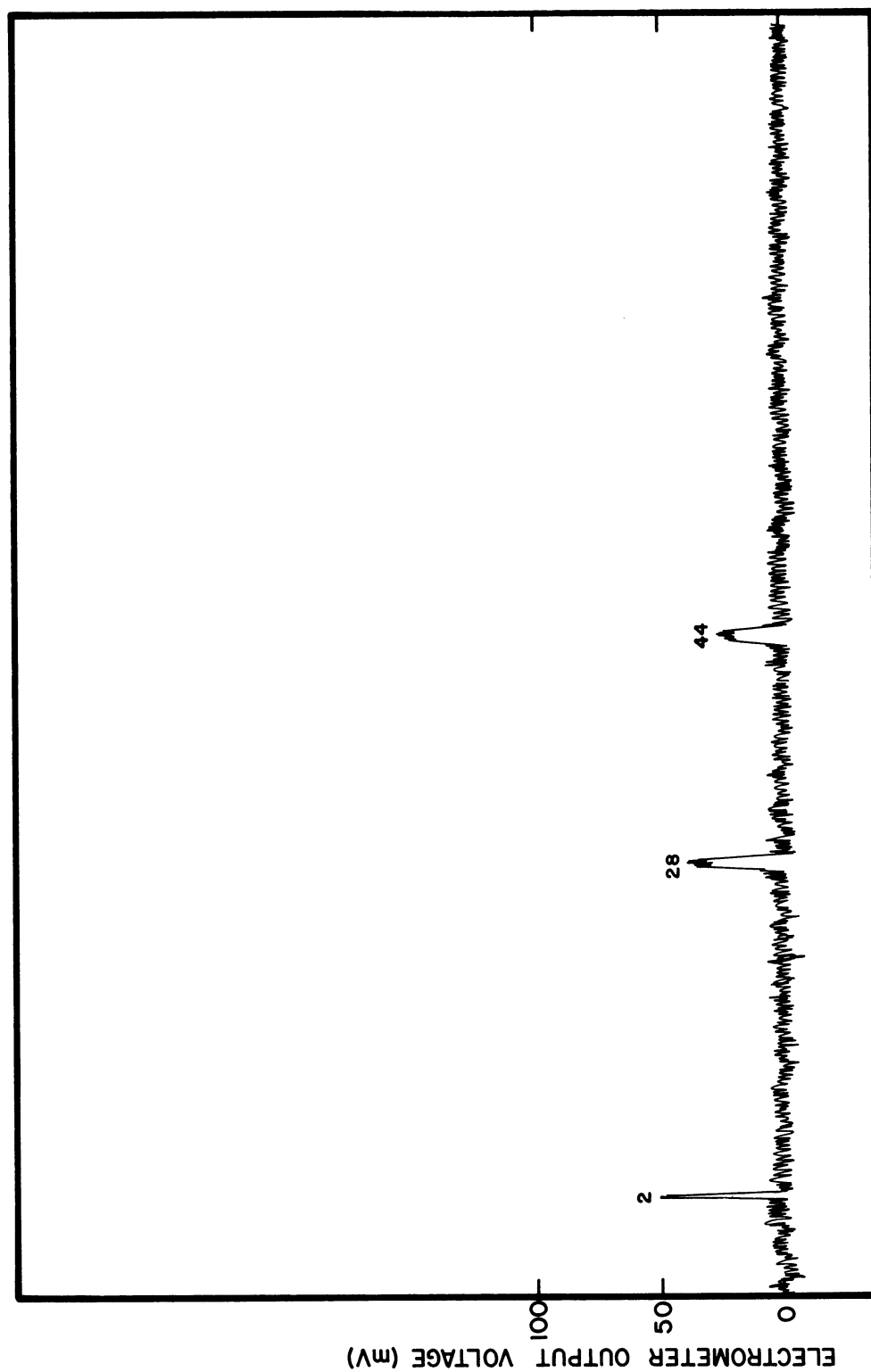


Figure 3.15b Quadrupole mass spectra, tungsten filament at 2800°K with a molecular oxygen flux of 10^{14} molecules $\text{cm}^{-2}\text{sec}^{-1}$ at the omegatron orifice and with the shutter closed.

there is no evidence of a molecular or atomic oxygen background with the shutter closed. However, in Figure 3.15a and in Figure 3.15b, the mass 28 and 44 peaks are heightened as compared to the peak height of Figure 3.14a. This is due to the presence of carbon monoxide and carbon dioxide. Carbon monoxide and carbon dioxide might be formed directly on the hot tungsten from carbon impurities which diffuse to the surface and react with the oxygen. They might also be formed on the stainless steel walls of the vacuum chamber. It became evident, however, that those contaminants originate directly in the ion source region, because it was observed that after closing the shutter, the mass 28 and 44 peak heights decreased slowly over a period of about two minutes to the initial values before atomic oxygen was generated. If the carbon monoxide and carbon dioxide had been formed on the tungsten filament, these peak heights should have returned to the original values immediately after shutter closing.

If these contaminants were formed on the walls of the main vacuum system, the contaminating flux into the quadrupole ion source would be essentially independent of the shutter position. If, however, some of the atomic oxygen which enters the ion source region is adsorbed on the walls of the ion source electrodes or on the vacuum housing of the quadrupole, and is gradually released after reacting with carbon atoms on the metal surfaces, the contaminant flux would disappear in a short time after the closing of the shutter as observed. Similarly, we would expect a gradual

buildup of these peaks after the atomic oxygen flow is started, and this was also observed. There was no observable change in the height of the hydrogen peak with changes between hot and cold filament conditions.

Finally, mass spectra were taken between atomic mass units of 160 and 250 in order to measure the tungsten dioxide and tungsten trioxide contamination in the oxygen beam. The results were negative. Even when the spectra were taken with decreased mass resolution and corresponding increase in sensitivity, the amount of tungsten dioxide and tungsten trioxide was below the detection limit of the quadrupole system.

On the omegatron side, a similar sequence of spectra was taken. Figure 3.16a corresponds to the quadrupole spectra shown in Figure 3.14b with the tungsten filament at room temperature. The effect of the shutter is demonstrated in Figure 3.16b. The last spectra, Figure 3.16c, which correspond to the trace of Figure 3.15a on the quadrupole side, were obtained when the filament was heated to 2800°K. Comparison of Figure 3.16a and 3.16c with Figure 3.14b and 3.15a shows that heating the tungsten filament has a considerably different effect on the omegatron measurement than on the quadrupole measurement. When the filament is heated, the peak height of the mass 32 peak in the omegatron decreases approximately to one-third of its height when the filament is cold, while the mass 32 peak height in the quadrupole measurement decreases to approximately one-tenth of its original height. Moreover, the ratio of the peak heights of mass

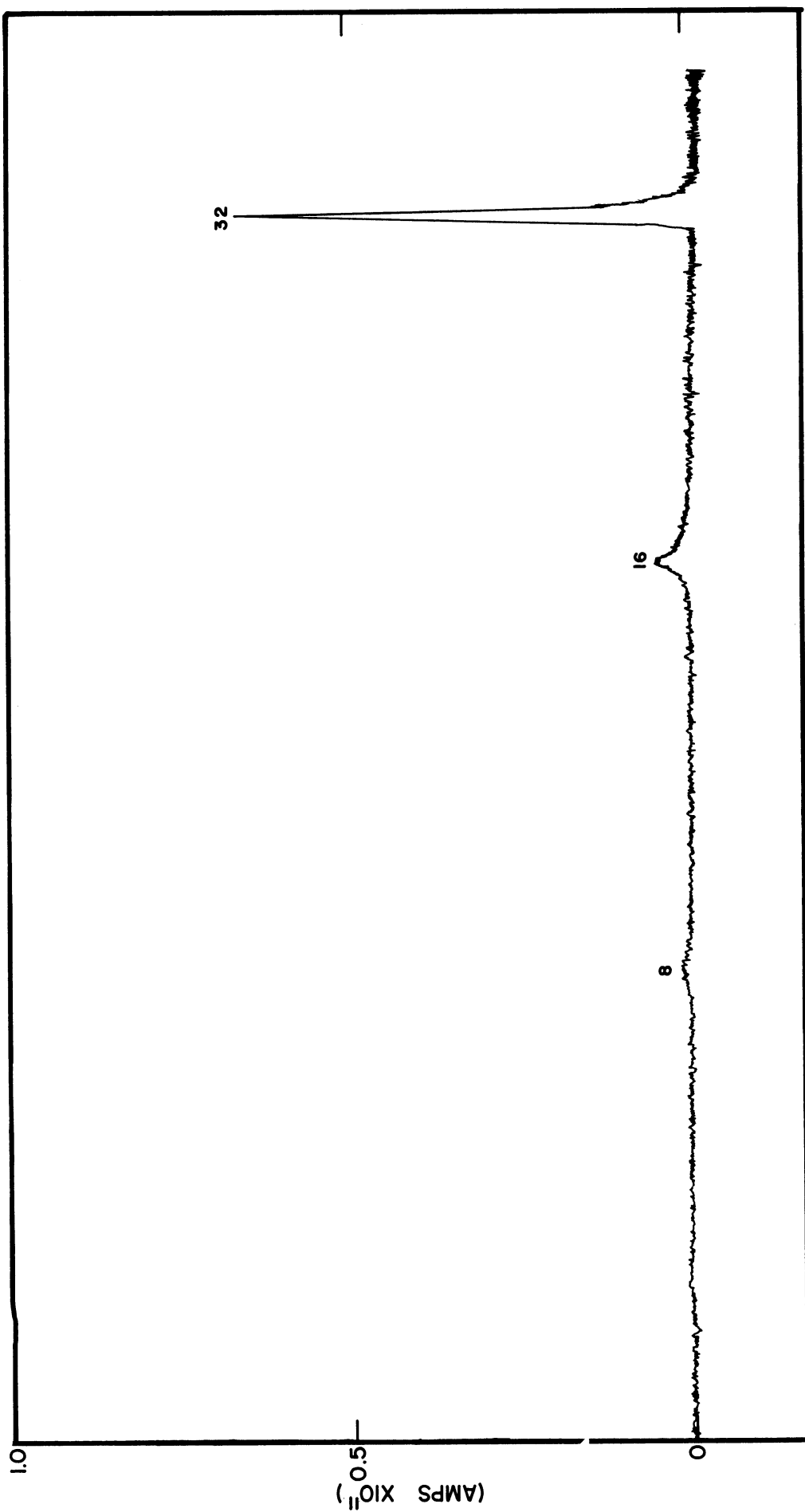


Figure 3.16a Omegatron mass spectra, tungsten filament at room temperature with a molecular oxygen flux of 10^{14} molecules $\text{cm}^{-2}\text{sec}^{-1}$ and with the shutter open.

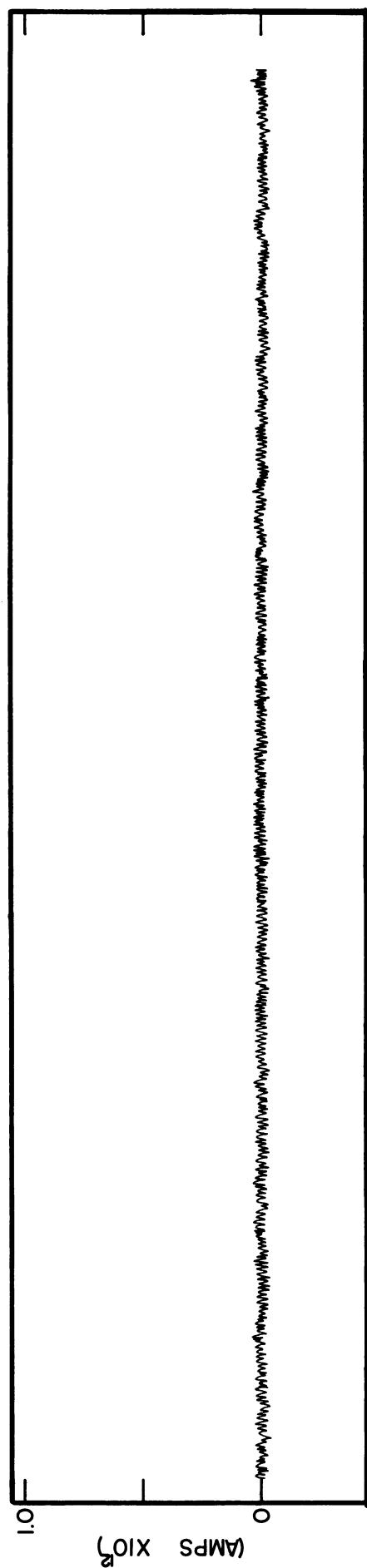


Figure 3.16b Omegatron mass spectra, tungsten filament at room temperature with a molecular oxygen flux of 10^{14} molecules $\text{cm}^{-2}\text{sec}^{-1}$ and with the shutter closed.

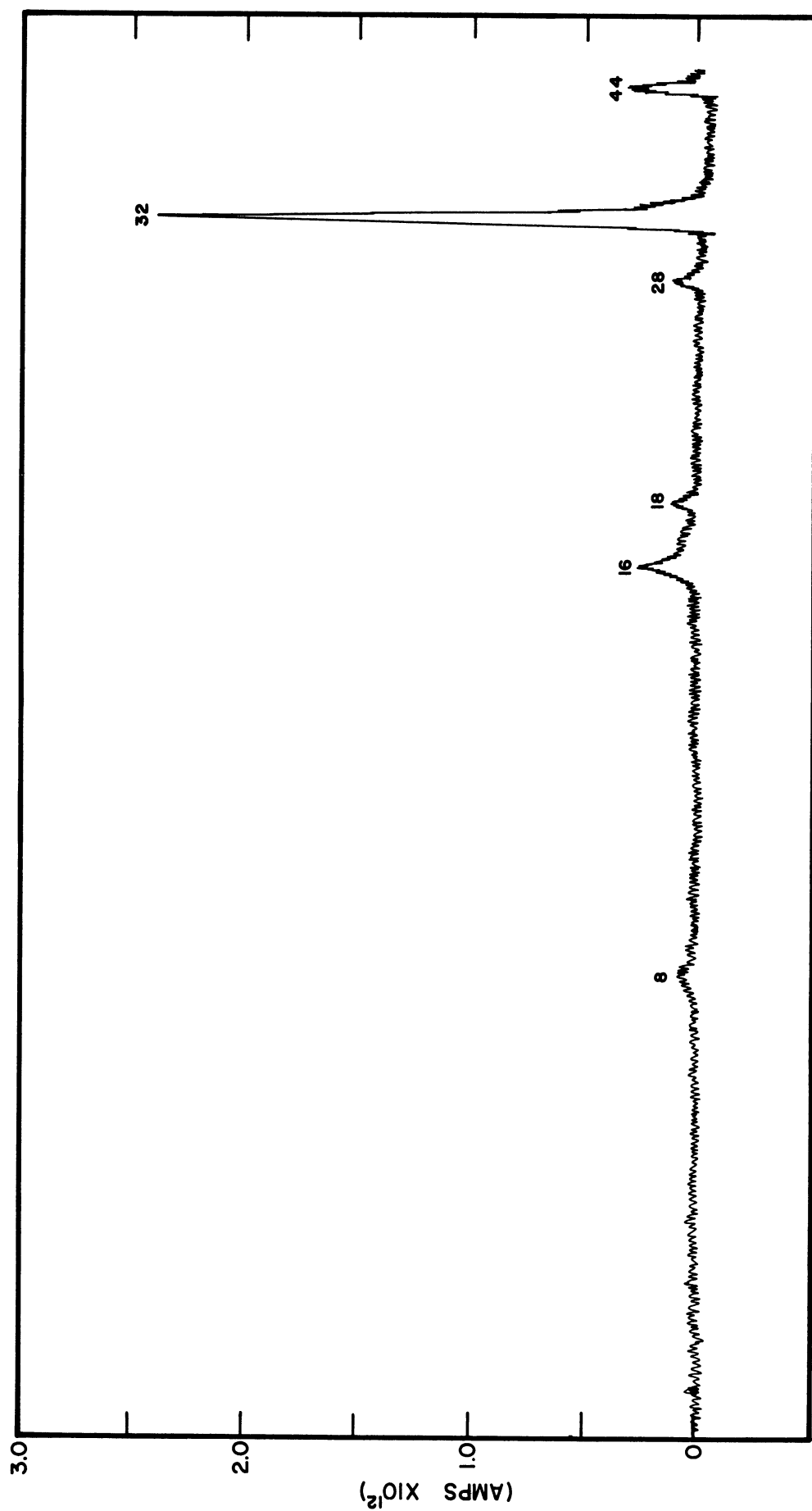


Figure 3.16c Omegatron mass spectra, tungsten filament at 2800°K with a molecular oxygen flux of 10^{14} molecules $\text{cm}^{-2}\text{sec}^{-1}$ and with the shutter open.

16 to mass 32 remains essentially unchanged in the omegatron, but a considerable increase in the ratio is noted in the quadrupole when the filament is heated. The relatively small decrease in the mass 32 peak height in the omegatron measurement is a result of atomic recombination in the omegatron chamber. The mass 16 and mass 8 peaks are caused by oxygen ions which are produced by dissociative and double ionization. The fact that the ratio of the mass 16 and mass 32 peak heights remain unchanged indicates that essentially no oxygen remained in atomic form in the omegatron chamber where ionization occurs. The mass 18, 28, and 44 peaks are water vapor, carbon monoxide, and carbon dioxide. These components are formed by surface reaction of atomic oxygen with adsorbed hydrogen and carbon. The recombination and the absorption of the atomic oxygen in the omegatron chamber are discussed in detail in Chapter IV.

3.4.3 The Strong Dependence of the Fractional Dissociation on the Temperature of the Tungsten Filament

To test the dependence of the oxygen dissociation on filament temperature, a series of peak height measurements, using the quadrupole, were made for molecular and atomic oxygen for various values of filament temperatures. The results are shown in Figure 3.17. The output voltages of the quadrupole electrometer are plotted versus filament temperature for a constant oxygen leak rate which corresponds to a flux of 8.4×10^{13} molecules/cm²sec at the omegatron orifice. Above 1000°K the molecular oxygen signal decreases rapidly,

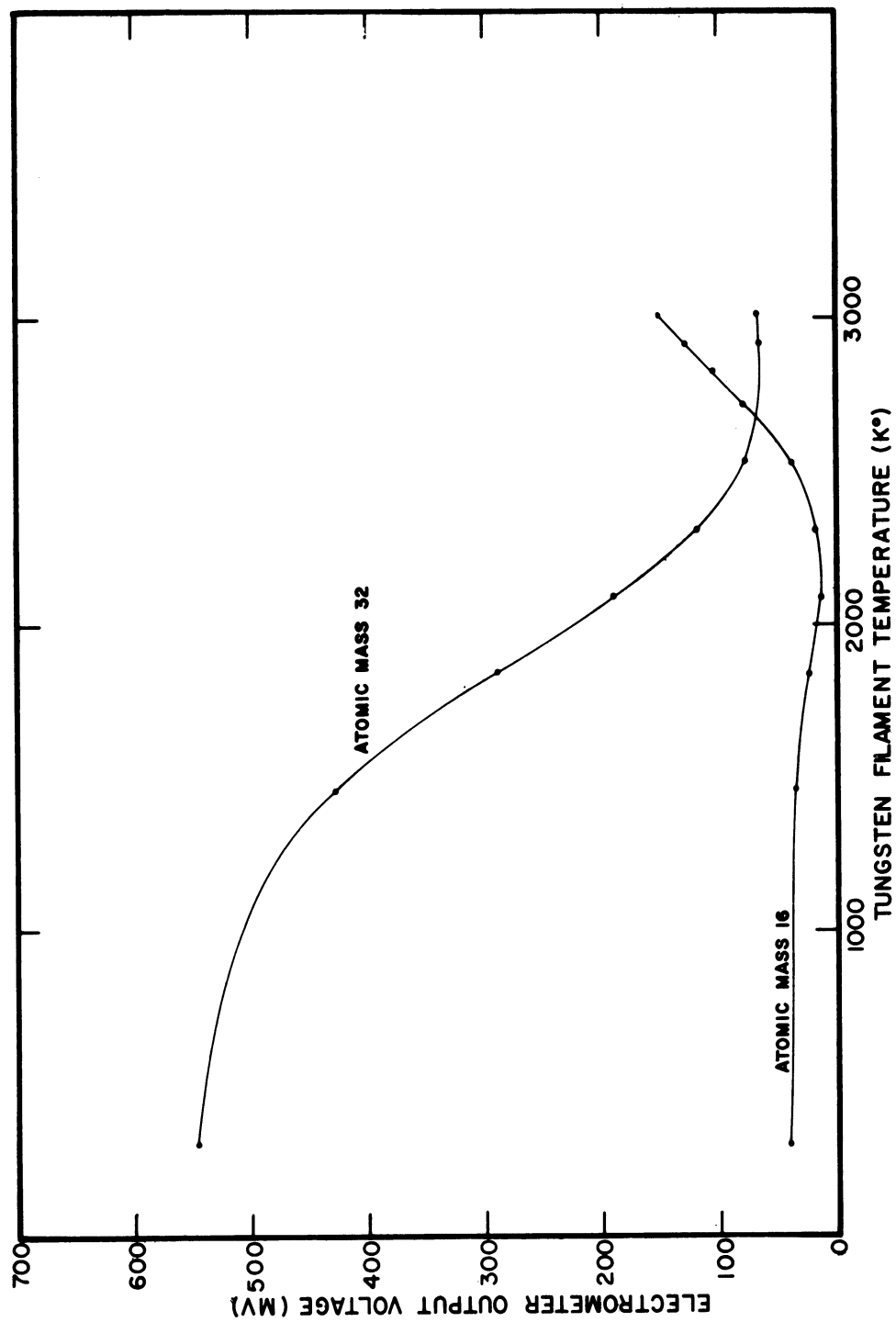


Figure 3.17 Dependence of the mass 32 and mass 16 output signal on the temperature of the tungsten filament.

reaching a plateau at about 2600°K. The mass 16 signal, which is the sum of the doubly ionized and dissociatively ionized molecular oxygen and atomic oxygen produced by the hot filament, decreases with increasing temperatures until a minimum is reached at about 2200°K. Above 2200°K, it increases rapidly, approaching a constant slope at the highest observed temperature. One would expect that this mass 16 curve should reach a plateau at the temperature where 100% dissociation occurs. This plateau was not yet reached at 3000°K. It is noted, however, that the quoted temperature values are upper limits. The end sections of the tungsten filament are still at lower temperatures, and therefore a gradual increase in the effective dissociation can be expected.

At very low temperatures, the mass 16 ion current consists only of dissociatively and doubly ionized molecular oxygen. It follows the decrease of the molecular oxygen signal until the atomic oxygen generated by the tungsten filament dominates and causes the mass 16 ion current to increase. The fractional oxygen disappearance and the fractional dissociation are again computed by using Equation (3.21) and Equation (3.32). The results are plotted in Figure 3.18. Curve A represents the fractional disappearance of molecular oxygen and curves B, C, and D represent the fractional dissociation for three different kinetic gas temperatures. It can be seen from the disappearance values, and those based on fractional dissociation that significant

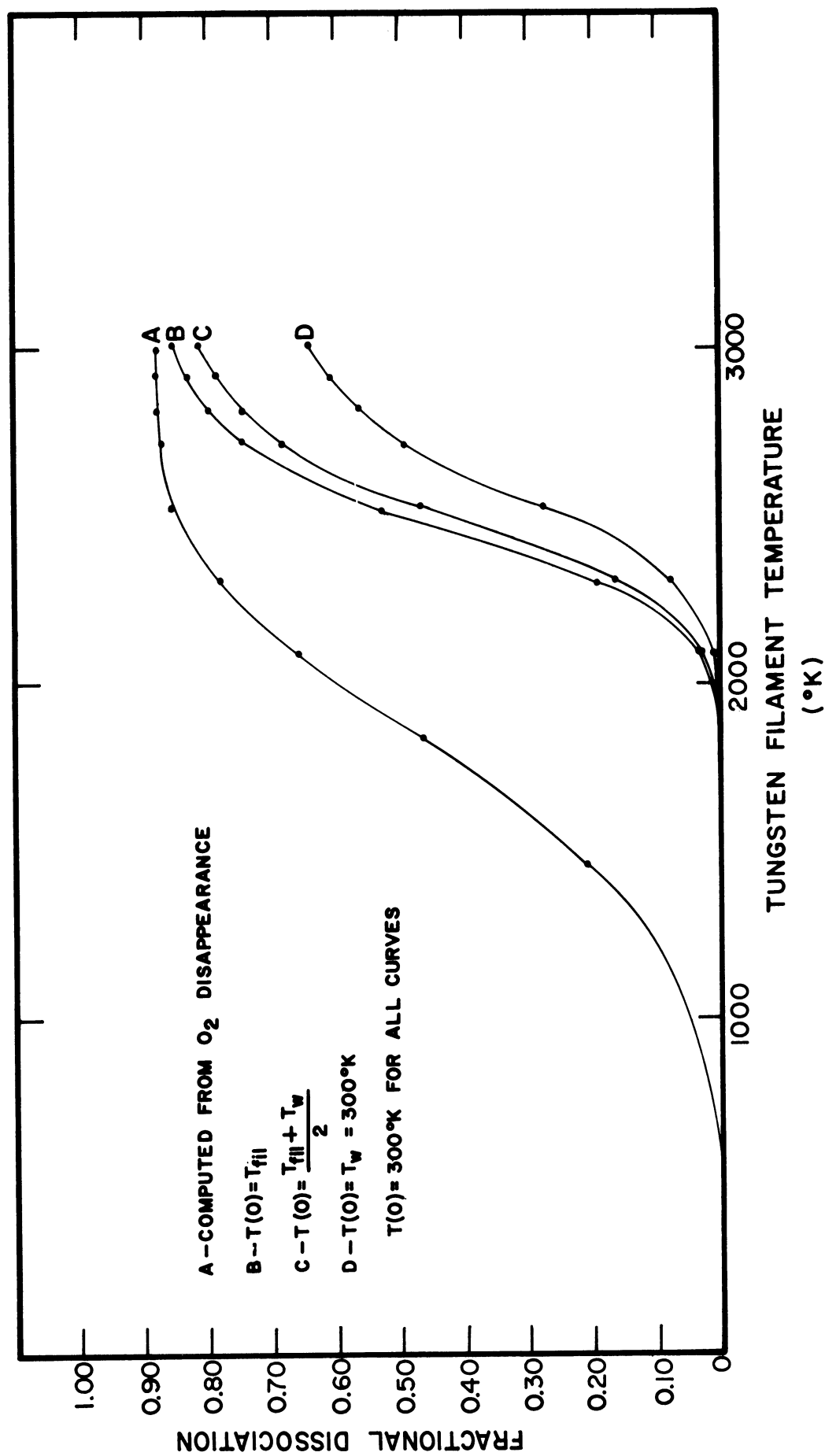


Figure 3.18 Dependence of the fractional dissociation on the temperature of the tungsten filament.

oxidation is occurring at temperatures below 1000°K , reaching a maximum value at about 2100°K . This is in general agreement with the results obtained by Schissel and Trulson (1965).

3.4.4 Flux Intensity Profile of the Oxygen Beam

The particular design of the quadrupole ion source required a narrow particle beam, if only direct streaming particles were to be ionized. Thus only a narrow column of the oxygen beam can be analyzed at a given instant. In contrast, the omegatron orifice intercepts a much wider column, and the total flux into the orifice is an average value of the angular flux intensity. The particular geometry of the oxygen source does not suggest a uniform flux pattern.

To measure the flux pattern, the vacuum system was mounted on two aluminum angle bars whose ends rested on a moveable platform (Figure 3.11), so that the vacuum system could be either moved parallel or rotated relative to the target. A quasi-angular scan is obtained by fixing the quadrupole to the reference frame and by moving the platform on the omegatron side. The maximum angular excursion is ± 3 degrees. It is limited by the travel of the platform and the size of the stainless steel bellows between the beam source and the quadrupole system. Because of the small separation of the source from the first aperture, a true angular scan cannot be obtained. Hence the measured flux patterns are a combination of parallel scan and angular scan results. Figures 3.19, 3.20, and 3.21 show the pattern obtained for

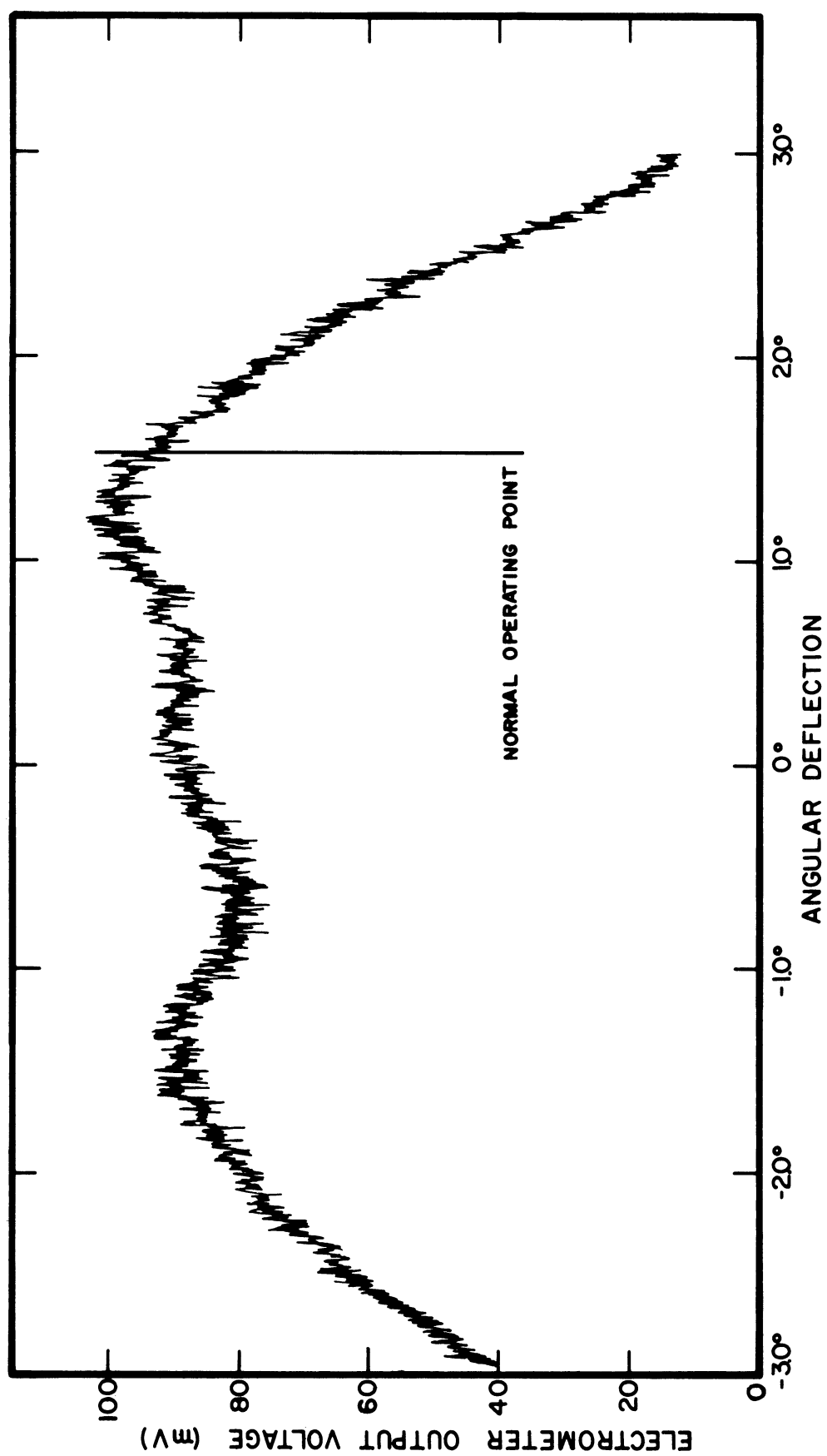


Figure 3.19 Angular flux profile of the oxygen beam when the tungsten filament is at room temperature (molecular oxygen).

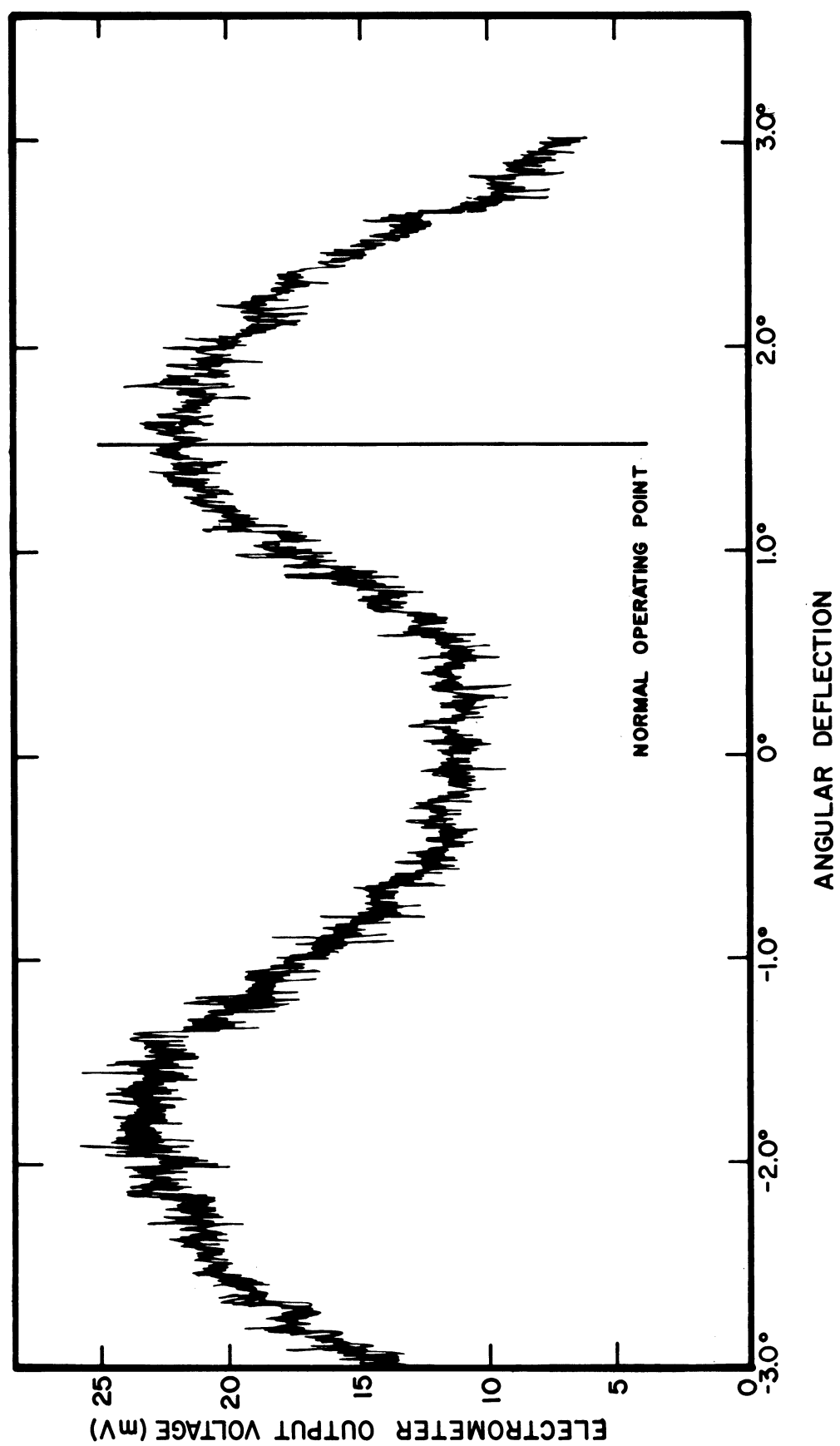
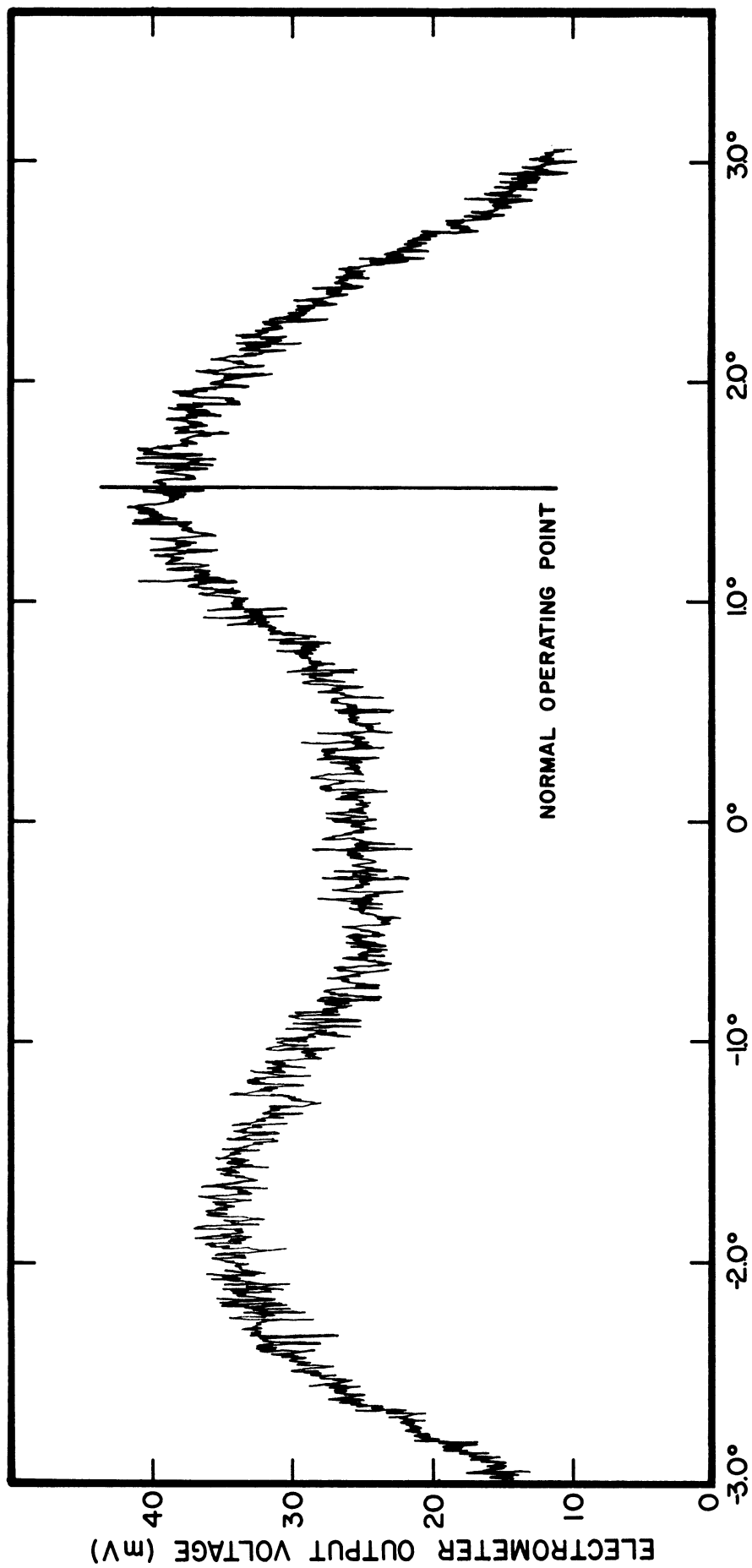


Figure 3.20 Angular flux profile of the oxygen beam when the tungsten filament is at 2800°K (molecular oxygen).



ANGULAR DEFLECTION

Figure 3.21 Angular flux profile of the oxygen beam when the tungsten filament is at 2800°K (atomic oxygen).

molecular oxygen and no dissociation, molecular oxygen with atomic oxygen present, and atomic oxygen, respectively.

The platform displacement was measured with a linear potentiometer whose output was used to drive the x-axis amplifier of the x-y recorder. All curves have the same pattern showing a maximum at the points where the flux originates from the titanium walls in the center between the tungsten filament and the outer edge of the titanium tube. The filament causes some obstruction in the center, and when the line of interception moves toward the edge of the titanium tube, the signal level approaches zero. In normal operation the quadrupole is so oriented that the ion source intercepts a maximum flow. The operating point is marked on the curves.

3.5 DISCUSSION OF THE RESULTS

Two fundamental problems exist in the described method of generating atomic oxygen. These are the formation of undesirable tungsten oxides and the uncertainty in the flux calibrations.

The oxide content in the beam is largely reduced with the double-wall tube design which allows most of the oxide to condense on the cold walls of the titanium tube. As long as the oxide buildup on the tube surface does not change the wall properties drastically, the problem is not critical. If, for example, the recombination efficiency on the walls is changed by the oxide, the atom-to-molecule ratio in the beam will change accordingly. But this ratio is measured during each test and difficulties arise only if the recombination coefficient approaches unity. A similar situation arises if the adsorption probability approaches unity on the tungsten oxide. Finally, the thermal accommodation could be changed because of the tungsten oxide, and therefore the kinetic temperature of the oxygen would change. This change relates to the second problem, the uncertainty in the flux calibration. It arises from insufficient knowledge of the particle velocities.

In the present experimental arrangement, there is no direct way to determine the particle velocity. Thus the possible values for the relative atomic oxygen concentration in the beam fall between curves B and D of Figure 3.13. This

uncertainty is reduced at low flux intensities where we can assume that nearly all primary molecular oxygen is dissociated. The situation is more complex at high flux levels where significant wall recombination may occur.

Without experimental proof the following argument is presented. The dissociated oxygen leaves the tungsten surface with a velocity characteristic to the temperature of the tungsten filament. The geometry of the source permits that some atoms leave the source directly without any further collisions. Most of the atoms, however, will experience one or several collisions with the titanium walls and with the tungsten filament. If we assume that the atoms collide with the walls on the average 3.5 times (this is the numerical value of the collimation factor), we can expect an effective accommodation of $\alpha_{\text{eff}} = 1 - (1-\alpha)^{3.5}$ where α is the thermal accommodation coefficient after one collision. If α is 0.1,

$$\alpha_{\text{eff}} = 1 - 0.9^{3.5} = 0.3. \quad (3.56)$$

Expressing α_{eff} in terms of temperature

$$\alpha_{\text{eff}} = \frac{T_{\text{fil}} - T}{T_{\text{fil}} - T_w} \quad (3.57)$$

where T_{fil} is the temperature of the filament, and

T_w is the wall temperature.

By solving for T , the temperature of the leaving atomic oxygen,

$$T = (1-\alpha_{\text{eff}}) T_{\text{fil}} + \alpha_{\text{eff}} T_w \quad (3.58)$$

and with $T_{\text{fil}} = 2800^{\circ}\text{K}$ and $T_{\text{w}} = 300^{\circ}\text{K}$

$$T = 0.7 \times 2800 + 0.3 \times 300 = 2050^{\circ}\text{K}. \quad (3.59)$$

Since the average velocity is proportional to the square root of the temperature, we find a change in the ratio of atomic to molecular oxygen by a factor of

$$\sqrt{\frac{2800}{2050}} = 1.17. \quad (3.60)$$

This changes the values for the fractional dissociation only by 4% at the high flux level shown in Figure 3.13. No data are available for the thermal accommodation coefficient on titanium oxide and tungsten oxide. Wise, et al. (1966) suggest a thermal accommodation coefficient for atomic oxygen on silicon oxide (SiO) of 0.01. One would expect a low accommodation coefficient for atomic oxygen from the following consideration. Atomic oxygen can stay on the surface for a short time interval only without either recombining with another atom or chemically reacting with the surface to form an oxide. Those atoms which do not recombine or react with the surface have spent little time on the surface, in accord with the concept of small thermal accommodation.

Conditions are different for molecular oxygen. Molecular oxygen which comes in contact with the hot tungsten surface and remains long enough to accommodate to the surface temperature will dissociate. Only those oxygen molecules which do not collide with the tungsten filament or which do not thermally accommodate to the surface do contribute the

molecular oxygen flux. The temperature of the fraction which results from atom recombination on the surface of the titanium tube is more difficult to predict, but this fraction should be small because of the low recombination coefficients of the titanium oxide and the small number of surface collisions of the atoms before emission from the tube. It can also be expected that the thermal accommodation coefficient for molecular oxygen on titanium oxide is significantly higher than for atomic oxygen. Wise, et al. (1966) measured a value of 0.17 on SiO.

The assumptions are made, therefore, that the atomic oxygen is emitted with a kinetic temperature equal to the temperature of the tungsten filament and the kinetic temperature of the emitted molecular oxygen is equal to the wall temperature of the titanium tube.

Inspection of Figure 3.13 shows that the value of the fractional dissociation computed from the mass 16 to 32 ion current ratios decreases more rapidly with incoming flux than the values computed from the molecular oxygen disappearance. This indicates a loss of oxygen which can result either from permanent adsorption on the surface of the titanium oxide walls or from oxidation of the tungsten filament. If the oxygen disappears because of adsorption on the titanium oxide walls, one would expect the adsorption to be more effective at low flux levels where saturation does not occur rapidly. However, the trend is just the opposite. Moreover, saturation or at least a reduction in adsorption should occur after several

hours of operation. This was not observed.

If oxidation of the tungsten is assumed to be the cause for the oxygen loss, it is useful to make a comparison of the measured values with the oxidation rates predicted in Appendix A. For a meaningful comparison, it is necessary to relate the measured molecular oxygen flux at the omegatron orifice to the primary flux to the tungsten filament. The relation between the signal flux at the omegatron orifice and the exit flux at the titanium tube is given by Equation (3.42). Under steady state conditions the net particle flux inside the titanium tube must be constant across any plane normal to the tube axis. However, the impact rate will be higher in the tube center than at the ends because particles may return close to their point of origin several times before they escape at the tube exit. This, in fact, is the mechanism which reduces the flow through the tube. Since the flux intensity does not change in the direction normal to the tube axis, independent of the tube length, (Clausing, 1932), only the angular spread is reduced. Hence it is assumed as a first approximation that the impact rate at the center of the tube is increased by a factor equal to the collimation factor. The relation between the flux at the omegatron orifice and the primary flux to the tungsten filament is then

$$\frac{\phi_{\Omega}}{\phi_w} = \frac{\Omega}{\pi} = 8.83 \times 10^{-4} \approx 10^{-3}. \quad (3.61)$$

The measured dissociation rates are indicated in Figure 3.1

along with the theoretically predicted values. In this figure, the cross marks indicate measured dissociation rates and the dashed line represents theoretically predicted values. The reference flux levels for the measured results were obtained by multiplying the corresponding flux at the omegatron orifice by 1000. The values chosen for the measured fractional dissociation correspond to curve B in Figure 3.13 (2800°K kinetic temperature of the atomic oxygen).

As is seen from the curves of Figure 3.1 the measured values of the fractional dissociation are higher than the predicted values for a clean tungsten ribbon. Also the predicted oxide fractions do not account for the loss of oxygen in the experiment. However, as mentioned above, each molecule will, on the average, collide more than once with the surface. Thus the probability of dissociation and oxidation is increased to

$$\mu_1' = 1 - (1 - \mu_1)^v \quad (3.62)$$

where μ_1 is the fraction of O, WO₂, and WO₃ computed for the tungsten ribbon and v is the average number of collisions with the tungsten filament. As an example, new values for the expected dissociation are computed for $v = 2$ and shown by a dashed line in Figure 3.1.

It should be noted that the values computed from the Schissel and Trulson (1965) model can give only order-of-magnitude results because, as shown in Appendix A, the model is not adequate at high temperatures, i.e., 2800°K.

Attributing, then, the difference between the computed fractional dissociation for the O_2 disappearance and the mass 16 and 32 ion current ratio to loss of oxygen due to oxidation, we find the correct total particle flux at the omegatron orifice by subtracting the amount lost from the values measured when the tungsten filament was at room temperature. We define the loss factor K by the equation

$$\phi_c'(O_2) = K \phi_c(O_2) \quad (3.63)$$

with

$$K = \frac{\phi_h(O_2) + \frac{1}{2} \phi_h(O)}{\phi_c(O_2)}. \quad (3.64)$$

Expressing K in terms of the flux ratio defined in Section 3.3.3 we have

$$K = \frac{1 + \frac{1}{2} \eta}{1 + \frac{1}{2} \bar{\eta}}. \quad (3.65)$$

New values for the relative concentration of atoms were computed for $T_h(O) = 2800^\circ K$. The data which are an accumulation of all measured values are shown in Figure 3.22 for the case in which the kinetic temperature of the atomic oxygen is equal to the filament temperature.

It is of interest to compare the velocity distribution of the oxygen atoms in the beam to the distribution encountered in a rocket experiment. In Figure 3.23 such a comparison is given. The kinetic temperature of the atomic oxygen in the beam is assumed to be $2800^\circ K$. The rocket velocity

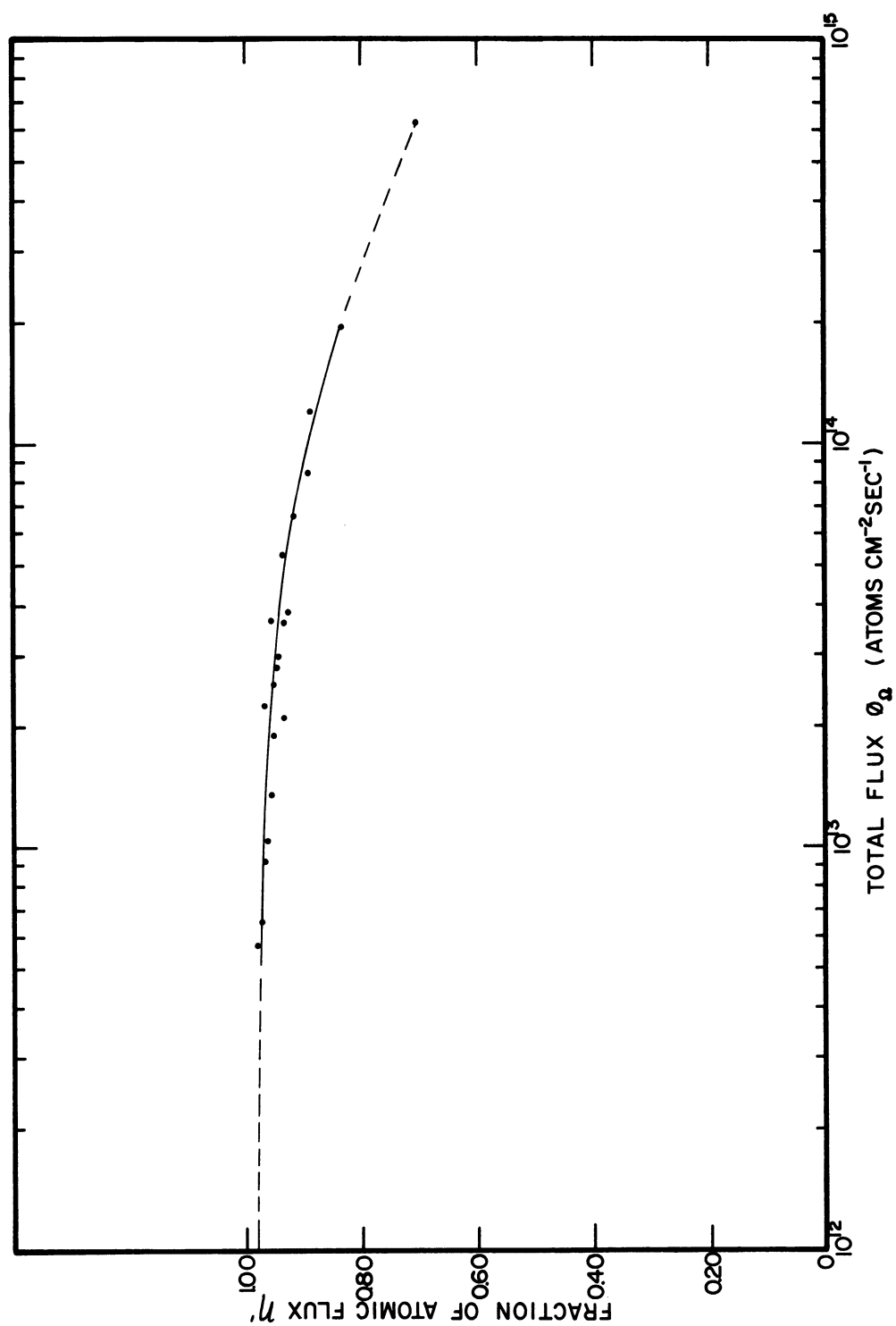


Figure 3.22 Relative atomic oxygen flux versus total particle flux at the omegatron orifice, $T(O) = 2800^\circ K$, $T(O_2) = 300^\circ K$.

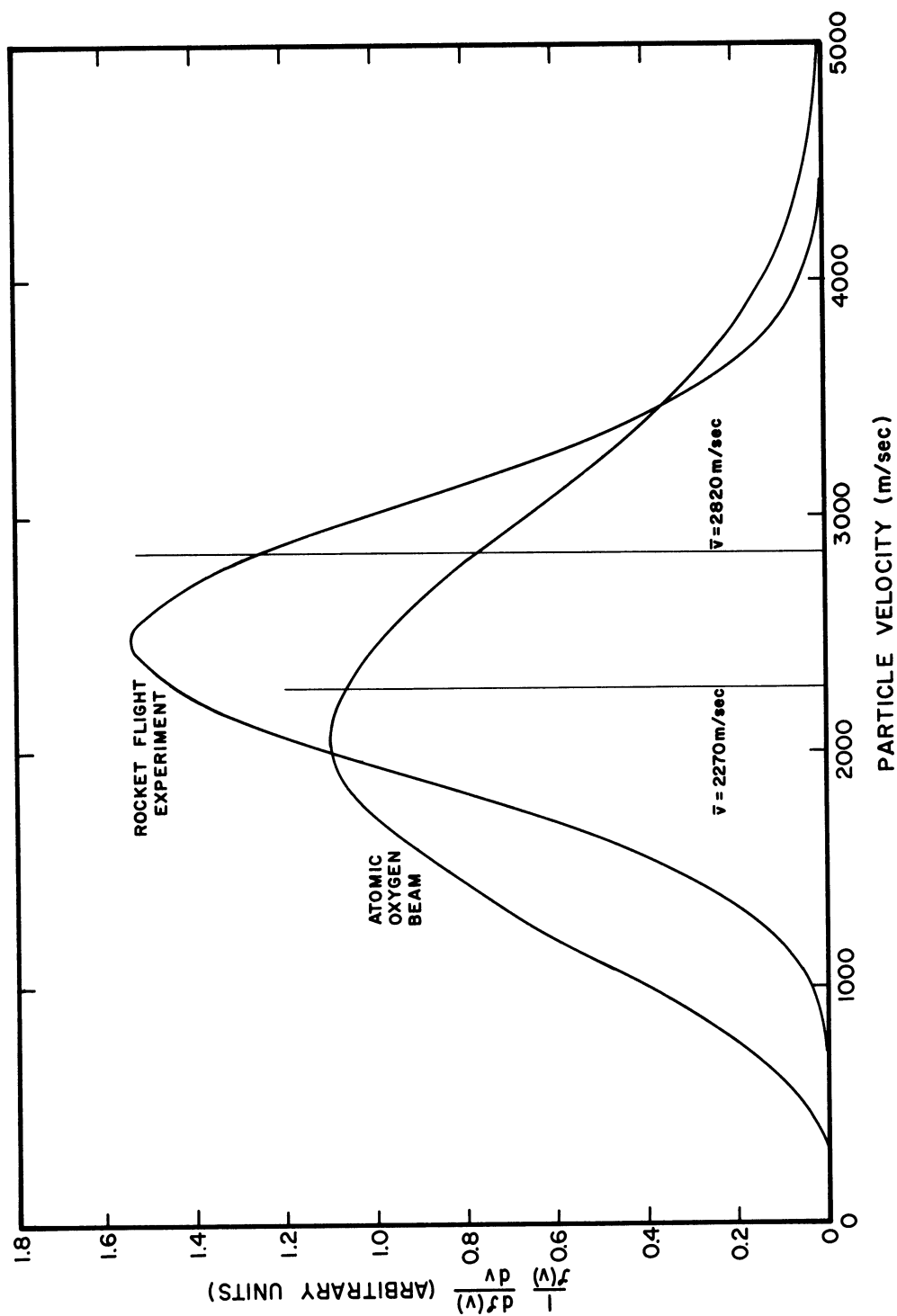


Figure 3.23 Comparison of the atomic oxygen velocity distribution in the beam with the distribution encountered during a typical rocket flight at normal incidence.

is assumed to be 2000 m/sec and the temperature of the ambient atomic oxygen is assumed to be 750°K. The curves shown in Figure 3.23 are normalized so that they enclose equal areas. The equations for the average velocities and the angular flux distribution are derived in Appendix E.

It can be suggested that oxygen molecules and atoms are converted to more active species by the hot tungsten filament. This could lead to surface reactions which are considerably different from reactions of the unexcited atoms and molecules. The lowest electronically excited state of atomic oxygen is the 'D state which is 2 eV above the ground state 3P (Herzberg, 1944), and the lowest electronically excited state of molecular oxygen is the ' Δ_g state which is 0.977 eV above the ground state $^3\Sigma_g^-$ of the oxygen molecule (Lighthill, 1957). The energy of dissociation of molecular oxygen is 5.07 eV (Lighthill, 1957). Therefore only significant proportions of excited molecular oxygen can be expected. By following Lighthill (1957) the ratio of excited to ground state molecular oxygen in a gas at equilibrium at temperature T is

$$\frac{n^*(O_2)}{n(O_2)} = \frac{2}{3} \exp \left(-\frac{E^*}{kT} \right) \quad (3.66)$$

where the excited state is of weight 2 and the ground state of weight 3. Hence for $T = 2800^\circ K$

$$\frac{n^*(O_2)}{n(O_2)} = \frac{2}{3} \exp \left(-\frac{11300}{2800} \right) = 1.17 \times 10^{-2}. \quad (3.67)$$

The filament acting as a catalyst cannot emit a gas which is more enriched in the excited species than a gas in an equilibrium composition at the same temperature without violating the second law of thermodynamics. The fraction of excited species in the beam will be considerably smaller since most molecules will be deexcited because they collide once or several times with the walls of the titanium tube before emission.

CHAPTER IV

EXPERIMENTAL STUDIES

4.1 ATOM RECOMBINATION AND ABSORPTION IN THE OMEGATRON SYSTEM

With the experimental arrangement described in the previous chapter, a number of recombination and absorption measurements have been obtained. Measurements were made on two omegatron systems which were distinguished only by their different surface materials. Both units were constructed of stainless steel, but the surface of one unit was chemically plated with pure gold. The instruments are identical to the units which were used in rocket flight experiments. A disassembled instrument is shown in Figure 4.1 and the omegatron cage is shown in Figure 4.2.

In the evaluation of the omegatron systems the net absorption and recombination will be computed from the measured value of flux, atom concentration in the beam, and the measured value of the omegatron ion currents for the atomic masses 16 and 32. As is seen from the mass spectrum of Figure 3.16, several other mass peaks occur when atomic oxygen is introduced into the omegatron system. Carbon monoxide, carbon dioxide, and water are formed on the surfaces of the omegatron chamber. The atomic oxygen which

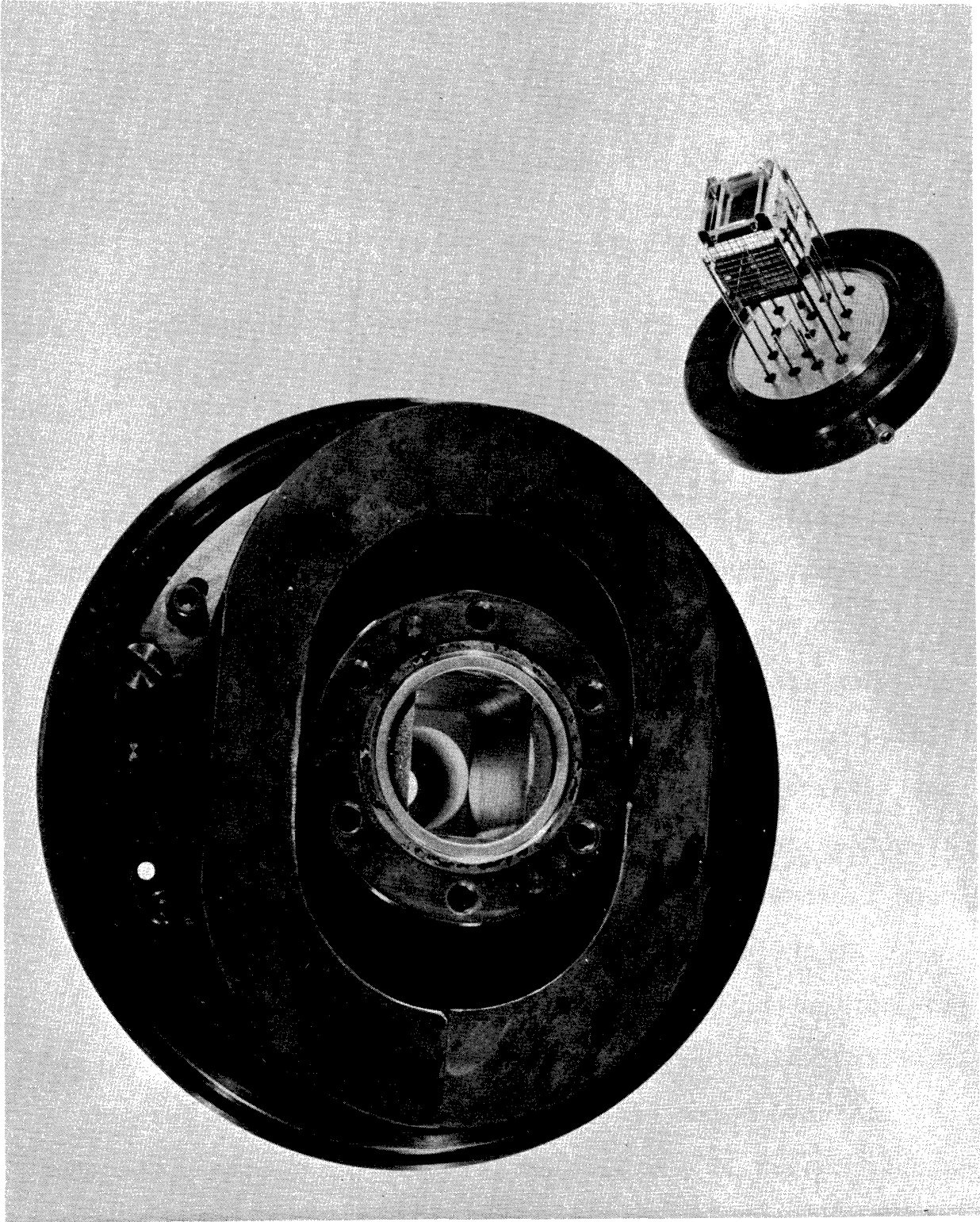


Figure 4.1 Omegatron envelope with magnet and omegatron cage.

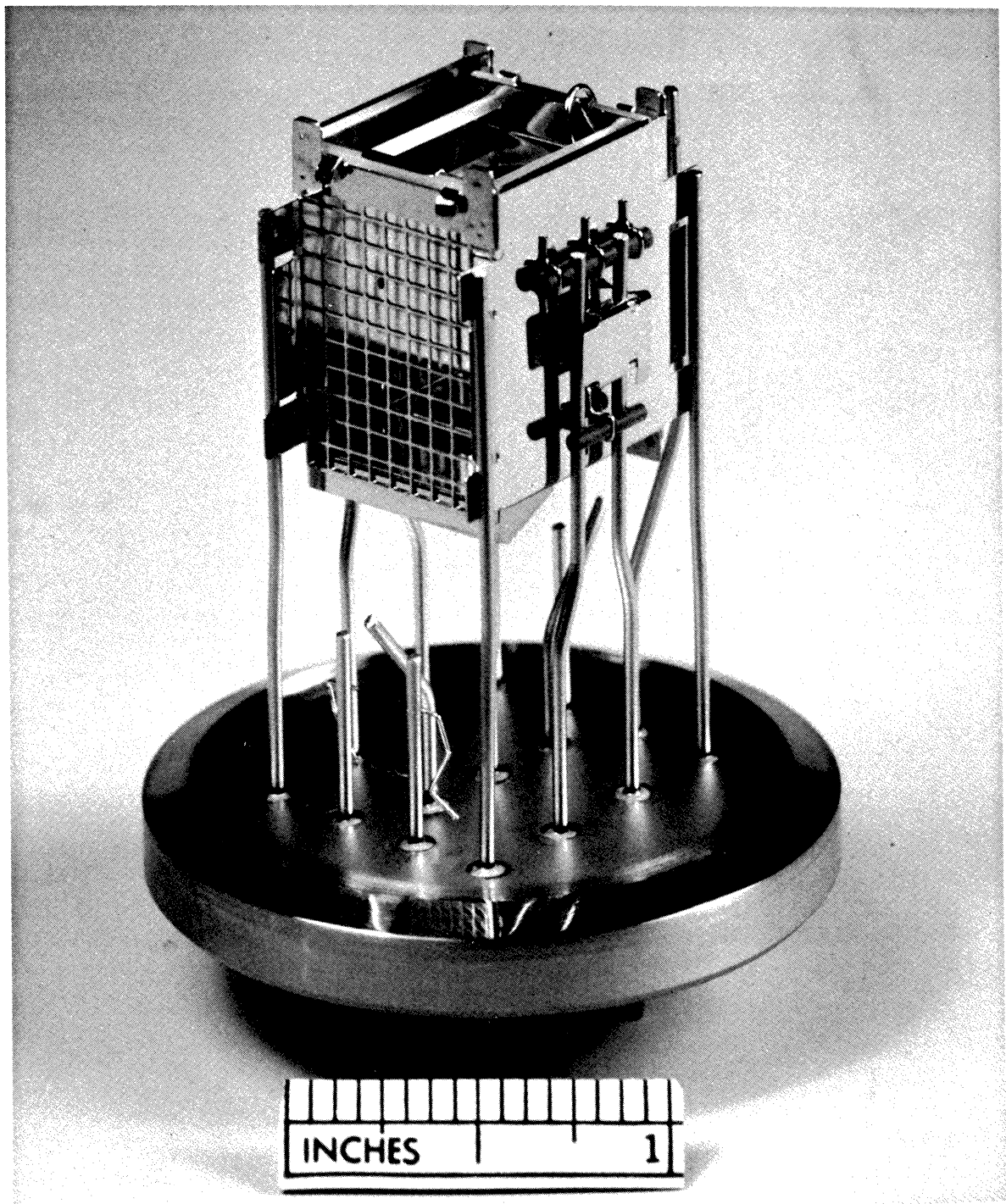


Figure 4.2 Omegatron cage.

combines with surface species such as carbon and hydrogen is in principle detectable during a flight experiment provided continuous mass scans are obtained or the mass numbers of the occurring peaks are known so that the spectrometer can be tuned alternatively to these masses. For the present evaluation, these products are included in the net absorption. The equation relating the net absorption, C , and the net recombination, R , in the omegatron to the measured parameters is derived in Appendix C. To simplify the computation it is useful to express R and C in terms of the measured density ratios or current ratios rather than in terms of the measured current or particle densities directly. Arbitrary units can then be used for the ion currents, i.e., length of deflection on the x-y recorder.

The net recombination is defined as the ratio of the flux of recombined oxygen atoms emitted from the omegatron orifice $\phi_{\Omega R}(O_2)$ to the atomic oxygen flux which enters through the orifice $\phi_{\Omega}(O)$.

$$R = \frac{2 \phi_{\Omega R}(O_2)}{\phi_{\Omega}(O)}. \quad (4.1)$$

In terms of the measured quantities and with the assumption of complete thermal accommodation of all species inside the omegatron chamber

$$R = \frac{I_{\Omega T}(O_2)}{K I_{\Omega C}(O_2)} \frac{1}{T} - \frac{1 - T}{T} \quad (4.2)$$

where K is defined by Equation (3.64), $I_{\Omega T}(O_2)$ is the value

of the omegatron mass 32 ion current during dissociation, and $I_{\Omega C}(O_2)$ is the value of the current without dissociation. Similarly, the net absorption is

$$C = \frac{1}{T} \left[1 - \frac{I_{\Omega T}(O_2)}{K I_{\Omega C}(O_2)} + \frac{1}{\sqrt{2}} \frac{I_{\Omega}(O)}{K I_{\Omega C}(O_2)} \frac{\sigma(O_2)}{\sigma(O)} \right]. \quad (4.3)$$

$I_{\Omega}(O)$ is the ion current resulting from the atomic oxygen; $\sigma(O)$ and $\sigma(O_2)$ are the ionization cross sections for O and O_2 . The energy of the ionizing electrons in the omegatron is 90 eV. The cross section ratio is obtained from Fite and Brackmann (1959).

$$\left. \frac{\sigma(O)}{\sigma(O_2)} \right|_{90 \text{ eV}} = 0.78 \quad (4.4)$$

It is noted that the mass 16 ion current in the omegatron is the sum of the currents which are produced by atomic oxygen ions formed directly by electron impact and ions which are formed from dissociatively and doubly ionized molecular oxygen. The latter quantities can be determined by measuring the mass 32 to 16 ion current ratio without dissociation. The same fraction of the mass 32 ion current has to be subtracted from the mass 16 ion current during dissociation.

4.2 EVALUATION OF A GOLD-PLATED OMEGATRON SYSTEM

The omegatron system is identical to the system used in previous rocket flight experiments (Taeusch and Carignan, June, 1967; October, 1967; January, 1968). The construction material is stainless steel. All exposed surfaces were gold-plated in a chemical plating process. The plating was performed by the Michigan Chrome Company of Detroit. A continuously filtered cyanide plating solution was used and the average plating thickness was 8 μm . Better plating methods were known at the time this instrument was prepared, but because of the intended close simulation of the conditions of the previous experiment, this method was chosen.

Initially the instrument preparation included a 48-hour bakeout at 350°C and a thorough evaluation of the omegatron operating parameters. For this evaluation molecular oxygen was introduced into the vacuum system, causing a pressure of approximately 5×10^{-8} torr. Neither liquid nitrogen cooling nor titanium gettering was needed.

After the initial evaluation, tests with atomic oxygen were made at several different flux levels. The results are tabulated in Table 4.1. Test number 1 showed a net recombination of 0.285 and a net absorption of 0.764. The ratio of currents for the atomic oxygen ions to the molecular oxygen ions is 2.26×10^{-2} . Thus, very little of the incoming atomic oxygen remains in atomic form. It either recombines or absorbs on the chamber walls.

TABLE 4.1

RESULTS OF MEASUREMENTS OF RECOMBINATION AND ABSORPTION IN THE OMEGATRON SYSTEMS

QUADRUPOLE		OMEGATRON							
T	η	$I_{\Omega C}(O_2)$	$I_{\Omega T}(O_2)$	$I_{\Omega}(O)$	**pressure	K	$\phi_{\Omega C}(O_2)$	R	C
		(A)	(A)	(A)	(torr)		(molecules/cm ² sec)		
1	0.850	3.60 x 10 ⁻¹²	1.02 x 10 ⁻¹²	2.30 x 10 ⁻¹⁴	1.50 x 10 ⁻⁷	0.720	5.35 x 10 ¹³	0.285	0.764
2	0.913	9.16 x 10 ⁻¹³	3.55 x 10 ⁻¹³	5.90 x 10 ⁻¹⁵	3.82 x 10 ⁻⁸	1.000	1.36 x 10 ¹³	0.330	0.663
3	0.887	2.50 x 10 ⁻¹²	9.16 x 10 ⁻¹³	3.05 x 10 ⁻¹⁴	1.04 x 10 ⁻⁷	0.803	3.72 x 10 ¹³	0.388	0.598
4	0.802	9.00 x 10 ⁻¹²	3.10 x 10 ⁻¹²	1.40 x 10 ⁻¹⁴	3.75 x 10 ⁻⁷	0.634	1.34 x 10 ¹⁴	0.434	0.563
5	0.931	1.50 x 10 ⁻¹²	3.60 x 10 ⁻¹³	1.12 x 10 ⁻¹⁴	6.25 x 10 ⁻⁸	1.000	2.23 x 10 ¹³	0.183	0.823
6	0.886	4.34 x 10 ⁻¹²	1.20 x 10 ⁻¹²	1.65 x 10 ⁻¹⁴	1.81 x 10 ⁻⁷	0.834	6.46 x 10 ¹³	0.248	0.798
7*	0.922	2.50 x 10 ⁻¹²	6.66 x 10 ⁻¹³		1.04 x 10 ⁻⁷	1.000	3.73 x 10 ¹³	0.212	0.758
8	0.912	7.34 x 10 ⁻¹³	2.00 x 10 ⁻¹³	2.50 x 10 ⁻¹⁵	3.06 x 10 ⁻⁸	0.940	1.09 x 10 ¹³	0.222	0.775
9	0.875	1.75 x 10 ⁻¹²	5.00 x 10 ⁻¹³	8.60 x 10 ⁻¹⁵	7.30 x 10 ⁻⁸	0.806	2.61 x 10 ¹³	0.263	0.733
10	0.936	4.50 x 10 ⁻¹³	1.00 x 10 ⁻¹³	4.20 x 10 ⁻¹⁵	1.88 x 10 ⁻⁸	0.940	6.70 x 10 ¹²	0.184	0.806
11	0.934	7.00 x 10 ⁻¹³	1.85 x 10 ⁻¹³	1.07 x 10 ⁻¹⁴	2.92 x 10 ⁻⁸	0.926	1.04 x 10 ¹³	0.235	0.765
12	0.885	2.40 x 10 ⁻¹²	6.75 x 10 ⁻¹³	1.64 x 10 ⁻¹⁴	1.00 x 10 ⁻⁷	0.790	3.57 x 10 ¹³	0.269	0.736
13	0.904	1.30 x 10 ⁻¹²	3.83 x 10 ⁻¹³		5.42 x 10 ⁻⁸	1.000	1.94 x 10 ¹³	0.220	0.780
14	0.850	4.50 x 10 ⁻¹²	1.47 x 10 ⁻¹²		1.58 x 10 ⁻⁷	0.796	6.70 x 10 ¹³	0.305	0.695

* $I_{\Omega C}(N_2) = I_{\Omega h}(N_2) = 1.35 \times 10^{-12}$ A $\phi_{\Omega}(N_2) = 2.01 \times 10^{13}$ molecules/cm²sec** pressure computed from $I_{\Omega C}(O_2)$

Since it was expected that the surfaces would saturate gradually after a long exposure to atomic oxygen, the system was then exposed to atomic oxygen for 2 hours at a flux level of about 4×10^{13} atoms/cm²sec. The tests were then repeated and the results are shown in rows 2, 3, and 4 of Table 4.1. There is indeed a reduced absorption at all three flux levels. The net recombination has increased, however, and again no significant amounts of atomic oxygen have been detected. When the results are compared with rocket flight results, agreement is found only in the fact that no atomic oxygen could be measured directly by observing the mass 16 ion current. The finite net recombination measured in the laboratory was not observed in the flight experiment. No measurable atom recombination occurred in the flight experiment.

Although the laboratory experiments were designed to closely simulate flight conditions, there are numerous differences. The omegatron envelope used in the laboratory was baked only one time, while the flight instruments are subjected to five or six bake-cycles before data are collected. Several days before the rocket is launched, the omegatron system is pinched off from a vacuum system and assembled with the flight instrumentation. The chamber pressure at pinch-off is usually in the 10^{-8} torr range. The major peak height occurs at mass 28. Small air leaks or virtual leaks in the omegatron chamber and continuous outgassing of the surfaces cause the pressure to rise gradually. The system used for the rocket flight with which data the laboratory

results were compared, reached a background pressure of about 10^{-5} torr at the time of launch. Yet another difference exists between the atmospheric conditions and the laboratory conditions. In the altitude range where oxygen measurements were made (210 km to 240 km), a substantial amount of molecular nitrogen is also streaming into the spectrometer chamber. It may be suggested that the walls of the chamber act as a catalyst for the atmospheric molecular nitrogen and atomic oxygen to form nitrous oxide, N_2O , (von Zahn, 1967). A relatively large mass 44 peak height has actually been observed in flight by several experimenters, (Nier, et al., November, 1964; Pokhunkov, 1962; Mauersberger, Müller, Offerman and von Zahn, 1968; and Schaefer and Nichols, 1964). The mass 44 peak height measured during the flights was considerably larger than in laboratory simulation with molecular oxygen. Moreover, the slope of the mass 44 altitude profile followed closely the slope of the atomic oxygen profile. Nier, et al. (1964) observed a peak height ratio 44/16 of 0.55 at 209 km and Gross, Offerman and von Zahn (1967) observed a ratio of 0.43 at 155 km. Since the spectrometers had stainless steel surfaces, it was assumed that the mass 44 peaks resulted from carbon dioxide which was formed from atmospheric atomic oxygen and the carbon contained in the stainless steel. It is interesting to note, however, that the peak height of mass 28 changed according to the expected scale height of the atmospheric molecular nitrogen, indicating that relatively little carbon monoxide was formed on the surface.

Inspection of the mass spectra of Figure 3.16 shows that the laboratory results (mass 44 to 28 peak heights) are in qualitative agreement with these flight results. To investigate these phenomena further, a capillary gas leak was mounted between the getter pump and the omegatron (Figure 3.11) through which molecular nitrogen could be introduced into the omegatron chamber. The capillary had a 0.039 cm inside diameter and it was pointed directly into the direction of the omegatron orifice. Its small size produced little obstruction for the oxygen beam. Since the installation required venting of the vacuum system, it was necessary to bake the system again at 350°C for 24 hours. A pure oxygen test was made first and the results are listed in rows 5 and 6 of Table 4.1. It is noted that the value of the net recombination decreased from the previously measured value. However, the basic characteristics of increased recombination with increased particle flux remained.

Molecular nitrogen was introduced into the omegatron during the next test. The test procedure was as follows. Constant flows of molecular nitrogen (2.01×10^{13} molecules/cm²sec) and molecular oxygen (3.73×10^{13} molecules/cm²sec) were produced and an initial flux measurement was made. Then dissociation was initiated and during that time the mass 28 peak height in the omegatron was recorded. The results are listed in row 7 of Table 4.1. Within the accuracy of the measurement no change in the molecular nitrogen peak height was observed during the test. The oxygen and the molecular

nitrogen did not mutually interact. As a result, the nitrous oxide formation had to be discarded as an explanation for the absence of atom recombination in the flight experiment. It should be noted that a nitrous oxide formation in the chamber would produce considerable distortion in the molecular nitrogen measurement, since both atmospheric atomic oxygen and molecular nitrogen are required for the process. In Appendix D a modified gas dynamic model is generalized to include nitrous oxide formation.

The decrease in effective recombination and corresponding increase in adsorption after the 48-hour bakeout suggests that a gradual deterioration of the gold-plating with increased heat treatment may be the explanation. To test this hypothesis the omegatron was baked again for 48 hours at 380°C and then a pure oxygen test was repeated (see rows 8 and 9 of Table 4.1). Again the results were negative. As is seen from the tabulated values, the net recombination rate did not change significantly from the previously measured value (row 7). The preliminary investigations on the gold-plated omegatron were discontinued and a stainless steel omegatron was mounted on the system.

4.3 EVALUATION OF A STAINLESS STEEL OMEGATRON SYSTEM

The same initial procedure as for the evaluation of the gold-plated omegatron was followed for the preparation of the stainless steel system. However, to avoid exposure of the omegatron to oxygen before the atomic oxygen test, the operating characteristics of the gauge were obtained with molecular nitrogen as test gas. Pure oxygen was then used to measure the absorption and net recombination. As is seen from the results in Table 4.1, rows 10, 11 and 12, there is a close correlation between results obtained from the gold-plated omegatron and the stainless steel omegatron.

Because of a failure in the quadrupole electronics, which resulted in a reduction in sensitivity, no more measurements were made in this particular state of the system. In the process of problem-finding, the system was dismantled and reassembled. The cause of the failure was finally located in the secondary electron multiplier electronics.

After repair of the system, another test with pure oxygen was performed (see rows 13 and 14 of Table 4.1). Again there is agreement with the previously measured value of recombination and adsorption. It is noted that the fractional dissociation is lower than that of the earlier tests. During the problem-hunt, the oxygen source was removed from the vacuum system for inspection. It was suspected that the oxygen feeding tube had been disconnected from the double-wall titanium tube. During the removal, the

oxide layer on the inside of the titanium tube was damaged at several points. The resulting change in surface properties is believed to be the reason for the decreased fractional dissociation.

4.4 DISCUSSION OF THE RESULTS

In accord with the results obtained from rocket flight experiments, the present preliminary measurements show an absence of atomic oxygen in both omegatron systems. However, the measured values of the net recombination of atoms do not agree with flight measurements. The essentially identical results obtained from the gold-plated and stainless steel systems indicate that the gold-plating is ineffective. In both cases the net recombination is flux-dependent. The unexpected finite recombination of atoms which occurred even during the initial exposure caused concern about the measurement technique and the extent to which the atmospheric conditions had been simulated.

It is recalled that the knowledge of the relative concentration of atomic oxygen in the beam depends on the knowledge of the kinetic temperature of the oxygen atoms and molecules. It is conceivable that the atom concentration in the beam is so low that all of the molecular oxygen in the omegatron results from incoming molecular oxygen only. If it can be shown that this can indeed be the case, there is at least no disagreement between the measurements made in the upper atmosphere and the results obtained in this experiment. If one assumes for a moment that all incoming oxygen atoms are absorbed on the omegatron walls (no recombination), then the change in the molecular oxygen flux, when the dissociation is in progress, must be the same in the omegatron and the quadrupole.

$$\frac{\phi_h(O_2)}{\phi_c(O_2)} = \frac{\phi_{\Omega h}(O_2)}{\phi_{\Omega c}(O_2)}. \quad (4.5)$$

Or, in terms of the output signals of the instruments,

$$\frac{U_h(O_2)}{U_c(O_2)} \sqrt{\frac{T_h(O_2)}{T_c(O_2)}} = \frac{I_{\Omega h}(O_2)}{I_{\Omega c}(O_2)}. \quad (4.6)$$

The kinetic temperatures $T_h(O_2)$ which are required to satisfy Equation (4.6) were computed for all measurements and are listed in Table 4.2. For all cases $T_c(O_2)$ is assumed to be 300°K. It is seen that the computed temperatures $T_h(O_2)$ fluctuate from 5750°K to 1750°K. Although it is perhaps possible that the molecular oxygen assumes a kinetic temperature which is close to the temperature of the tungsten filament, it is not likely that the molecular oxygen assumes a temperature which is higher than the filament temperature. Only if most of the molecular oxygen in the hot beam results from atom recombination and newly formed molecules evaporate with an excess kinetic energy, is it possible to explain the results. The large fluctuations in the apparent temperatures do not support the argument.

To find a correspondence between the variation of the molecular oxygen ion currents in the omegatron and the quadrupole, a test was performed where the two output signals were simultaneously recorded while the tungsten filament temperature was increased step-by-step from room temperature to 2800°K. Both output signals, normalized to their values

TABLE 4.2

MEASURED QUADRUPOLE AND OMEGATRON DATA AND
APPARENT KINETIC TEMPERATURE OF THE MOLECULAR OXYGEN

	$U_c(O_2)$ (V)	$U_h(O_2)$ (V)	$I_{\Omega C}(O_2)$ (A)	$I_{\Omega T}(O_2)$ (A)	$T_h(O_2)$ (°K)
1	0.375	0.04	3.60×10^{-12}	1.02×10^{-12}	2090
2	0.095	0.0083	9.16×10^{-13}	3.55×10^{-13}	5750
3	0.265	0.024	2.50×10^{-12}	9.16×10^{-13}	5040
4	1.000	0.125	9.00×10^{-12}	3.10×10^{-12}	2350
5	0.087	0.006	1.50×10^{-12}	3.60×10^{-13}	3660
6	0.280	0.0265	4.34×10^{-12}	1.20×10^{-12}	2560
7	0.081	0.00625	2.50×10^{-12}	6.66×10^{-13}	3570
8	0.100	0.00825	7.34×10^{-13}	2.00×10^{-13}	3280
9	0.240	0.024	1.75×10^{-12}	5.00×10^{-13}	2430
10	0.091	0.0055	4.50×10^{-13}	1.00×10^{-13}	4060
11	0.086	0.00525	7.00×10^{-13}	1.85×10^{-13}	5620
12	0.258	0.0235	2.40×10^{-12}	6.75×10^{-13}	2860
13	0.071	0.0065	1.30×10^{-12}	3.83×10^{-13}	3110
14	0.246	0.0295	4.50×10^{-12}	1.47×10^{-12}	2220

at room temperature, are shown in Figure 4.3 as functions of the filament temperature. Clearly, the quadrupole signal (curve B) decreases more rapidly than the omegatron signal (curve A). This suggests an increase in the kinetic temperature of the molecular oxygen. Moreover, at about 2500°K the omegatron signal increases again. A comparison with Figure 3.18 shows that significant amounts of oxygen are generated at this temperature. Hence, it is concluded that the relative increase in the molecular oxygen density in the omegatron is indeed due to atomic recombination.

Several thermal accommodation coefficients were tried to account for the difference between the relative signal levels of the quadrupole and the omegatron at the temperature where no dissociation occurs. It was found that the curves can be brought together when a thermal accommodation coefficient of $\alpha_{\text{eff}} = 0.1$ is chosen and the kinetic temperature of the molecular oxygen is computed from the relation

$$\alpha_{\text{eff}}(\text{O}_2) = \frac{T_{\text{h}}(\text{O}_2) - T_{\text{w}}}{T_{\text{fil}} - T_{\text{w}}}. \quad (4.7)$$

The results are shown in Figure 4.3, curve C.

By assuming that the accommodation coefficient does not change at the high filament temperature, new values for the fractional dissociation, net recombination, and adsorption can be computed. As an example, new parameters were computed for all measured data by assuming that the molecular oxygen and, without further justification, also the

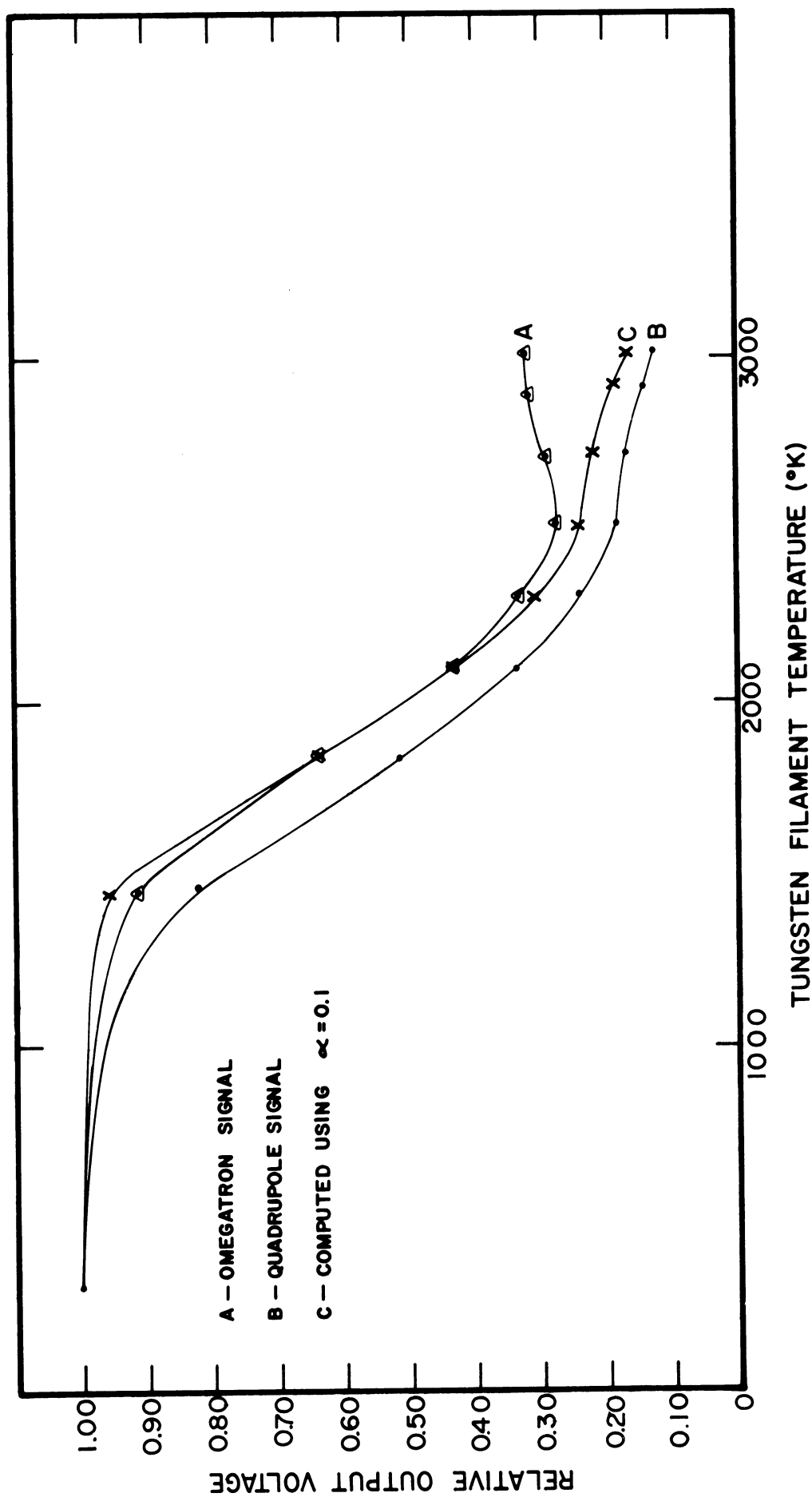


Figure 4.3 Normalized mass 32 output signals of the quadrupole and the omegatron versus temperature of the tungsten filament at constant source flux.

TABLE 4.3

FINAL RESULTS OF NET RECOMBINATION AND
ABSORPTION OF OXYGEN ATOMS IN THE OMEGATRON SYSTEMS

	T'	K'	$K' \phi_{\Omega C} (O_2)$	$\phi'_{\Omega} (O)$	R'	C' = 1-R'
	(molecules/cm ² sec) (atoms/cm ² sec)					
1	0.800	0.720	3.85×10^{13}	3.42×10^{13}	0.240	0.760
2	0.880	0.983	1.34×10^{13}	1.25×10^{13}	0.311	0.689
3	0.846	0.792	2.95×10^{13}	2.71×10^{13}	0.365	0.635
4	0.740	0.646	8.06×10^{13}	7.36×10^{13}	0.370	0.630
5	0.905	0.980	2.18×10^{13}	2.07×10^{13}	0.166	0.834
6	0.844	0.820	5.30×10^{13}	4.85×10^{13}	0.215	0.785
7	0.893	0.971	3.61×10^{13}	3.40×10^{13}	0.187	0.813
8	0.880	0.925	1.01×10^{13}	9.46×10^{12}	0.198	0.802
9	0.830	0.794	2.06×10^{13}	1.87×10^{13}	0.228	0.772
10	0.911	0.918	6.15×10^{12}	5.86×10^{12}	0.168	0.832
11	0.910	0.915	9.51×10^{12}	9.07×10^{12}	0.198	0.802
12	0.884	0.790	2.82×10^{13}	2.58×10^{13}	0.237	0.763
13	0.869	0.940	1.82×10^{13}	1.69×10^{13}	0.210	0.790
14	0.800	0.810	5.42×10^{13}	4.82×10^{13}	0.254	0.746

atomic oxygen are affected by thermal accommodation equivalent to $\alpha_{\text{eff}} = 0.1$. Since the atomic oxygen is initially emitted from the filament we have

$$\alpha_{\text{eff}}(0) = \frac{T_{\text{fil}} - T_{\text{h}}(0)}{T_{\text{fil}} - T_{\text{w}}} \quad (4.8)$$

and with

$$T_{\text{fil}} = 2800^{\circ}\text{K} \text{ and } T_{\text{w}} = 300^{\circ}\text{K} \quad (4.9)$$

$$T_{\text{h}}(0) = 2550^{\circ}\text{K} \text{ and } T_{\text{h}}(\text{O}_2) = 550^{\circ}\text{K}. \quad (4.10)$$

The results are listed in Table 4.3. The absorption coefficients listed in this table are simply the differences $C' = 1 - R'$ because there is no significant amount of atomic oxygen in the omegatron chamber. The measured atomic oxygen ion currents are too close to the noise limit of the system to allow meaningful interpretation.

For comparison, all measured values of R' are plotted in Figure 4.4 as a function of the incoming atomic oxygen flux $\phi_{\Omega}'(0)$. All data points are numbered according to the sequence in which they were obtained. Three groups are clearly distinguished and can be correlated with the particular experimental conditions under which they were obtained. Data points 5, 6, and 7 represent values which were obtained immediately after the system had been exposed to atmospheric pressure and subsequently had gone through a 48-hour bake cycle. Before exposure to atmospheric pressure it had also been subjected to atomic oxygen for a 2-hour period. Data points

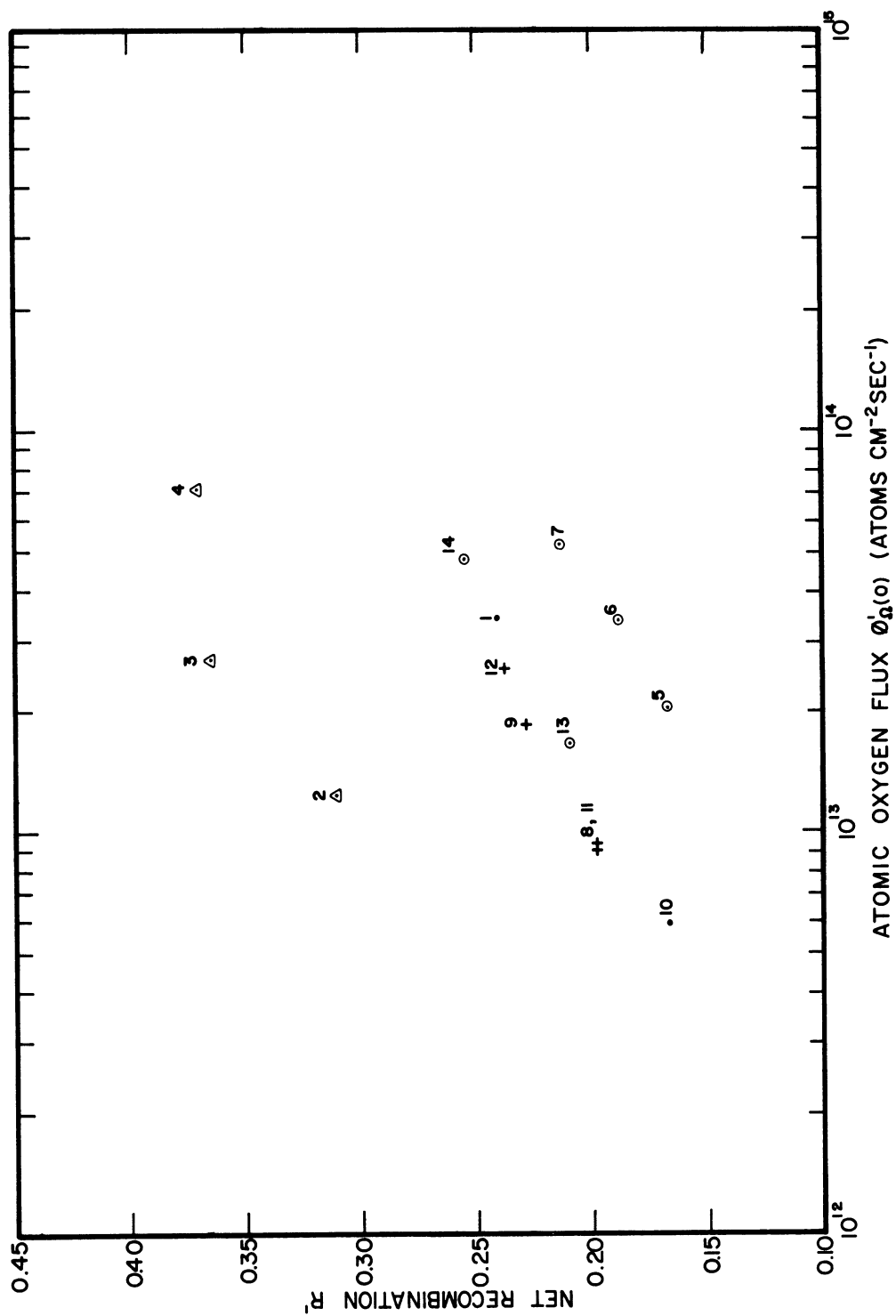


Figure 4.4 Atomic oxygen flux dependence of the measured values of the net atom recombination in the omegatron.

1, 8, and 9 were obtained after the omegatron was exposed to atomic oxygen for a short time interval of approximately 15 minutes.

A significant change occurred after 2 hours of exposure to atomic oxygen as is seen from the data points 2, 3, and 4. Although the system was evacuated after the 2-hour atomic oxygen exposure, and a background pressure of 4×10^{-10} torr was obtained, the partial surface saturation appeared unchanged until the system was exposed to atmospheric pressure and baked at a high temperature. The data for the stainless steel omegatron, points 10 to 14, follow closely the results for the gold-plated omegatron 1, 8, and 9, indicating that there is no difference between the two systems.

In order to relate R' and C' to the correction term defined by Equation (2.41), an absorption term has to be included in Equation (2.41). If no absorption occurs,

$$R' = \frac{1}{1 + \frac{1}{\epsilon(\gamma)}} = \frac{1}{1 - \frac{(1-\gamma)p}{\gamma}} \quad (4.11)$$

Since $\epsilon(\gamma)$ denotes simply the disappearance of atomic oxygen, γ can be replaced by $\gamma + \lambda$ where λ is the probability of adsorption after one bounce and ϵ assumes the form

$$\epsilon(\gamma, \lambda) = \frac{\gamma + \lambda}{(1-\gamma-\lambda)p} \quad (4.12)$$

By inspection the expressions for R' and C' are

$$R' = \frac{\gamma}{\gamma + \lambda} \frac{1}{1 + \frac{(1-\gamma-\lambda)p}{\gamma + \lambda}} \quad (4.13)$$

$$C' = \frac{\lambda}{\gamma + \lambda} \frac{1}{1 + \frac{(1-\gamma-\lambda)}{\gamma + \lambda} p} \quad . \quad (4.14)$$

Solving for γ and λ in terms of p , R , and C ,

$$\gamma = \frac{R' p}{1 - (1-p) (R+C')} \quad (4.15)$$

$$\lambda = \frac{C' p}{1 - (1-p) (R+C')} \quad . \quad (4.16)$$

These equations give meaningless answers when $R' + C' = 1$ because the conditions of quasi-equilibrium in the omegatron chamber are not satisfied. The atomic oxygen recombines or is absorbed before it can enter the ionization region of the omegatron. The recombined oxygen is free to move into the ionization region, however, without being absorbed on the walls. Hence, only the ratio of the recombination coefficient to the absorption coefficients can be computed. In order to measure the absolute values of γ and λ , a more open gauge structure is needed to permit atoms to enter the ionization region after fewer wall collisions. For greater accuracy a detailed knowledge of the collision distribution is desirable. However, the disagreement in the measured value of the net recombination between the flight results and the laboratory tests is real. In summarizing, it has been demonstrated in this experiment that atomic oxygen, when introduced into the flight-type omegatron mass spectrometer does partially recombine into molecular oxygen and partially absorb on the walls of the instrument. Recombination and absorption are flux

dependent and a gradual decrease in the net absorption and a corresponding increase in the net recombination occurs after a long time exposure to atomic oxygen, indicating a partial saturation of the surface.

The saturation is not permanent and can be removed by an instrument bakeout. The results also show that no oxygen remains in the atomic state when it has reached the ionization region of the omegatron. While the latter result is in agreement with observations made on flight experiments, the results of the finite atomic recombination, although expected from theory, do not agree with flight observations. Further studies using the atomic oxygen beam system are necessary to fully satisfy this question.

CHAPTER V

CONCLUSIONS AND SUGGESTIONS

The objective of the work here described has been to develop an experimental technique to evaluate mass spectrometer systems for atomic oxygen measurements in the upper atmosphere. A very suitable technique is provided by employing a neutral particle beam of known composition and flux intensity to simulate the conditions encountered in an upper atmosphere experiment.

In all major respects this objective has been achieved. An atomic oxygen beam source of known concentration and composition has been designed and tested. Relative atomic concentrations of more than 70% have been obtained in the beam which is free of chemically active contaminants. The relative atomic concentration and the flux intensity of the beam can be varied and permit a close simulation of atmospheric conditions at about 200 km altitude. It has been found that for the flux range of interest the method of thermal dissociation of oxygen molecules on a hot tungsten surface is superior to other known methods for atomic oxygen generation. Undesirable beam contaminants, hydrocarbons, and water vapor, for example, are eliminated by intensive chemical and cryogenic pumping. The particular design of

the oxygen source makes the contributions of tungsten oxides in the beam negligible.

The combined use of the open ion source quadrupole mass spectrometer and the closed ion source omegatron mass spectrometer made it possible to obtain a flux calibration. The accuracy of the calibration depends on the accuracy of the measurements of the omegatron sensitivity to molecular oxygen. The necessary measurements can be obtained from conventional calibration methods. The accuracy of the beam calibration also depends on the information available regarding the ionization cross section ratio of the oxygen atoms and molecules and on the kinetic temperature of the beam particles acceptably determined in relation to the source temperature. The square root relation between the flux and the kinetic temperature makes the sensitivity to temperature uncertainties a minor limitation.

The preliminary measurement of the net recombination and absorption of atomic oxygen in the gold-plated and stainless steel omegatron systems showed that a large fraction of the atomic oxygen is absorbed by the wall of the instrument in accord with results obtained in flight experiments. The finite atomic recombination in the omegatron chamber which was measured in the laboratory experiment is not in full agreement with the very limited amount of data from flight observations.

Clearly the experimental results indicate a need for further tests, employing mass spectrometers with different

surface materials and different instrument geometries.

The following suggestions are offered for improvement of the beam system and for further experiments.

Suggested system improvements:

(1) A time-of-flight analysis of the beam should be carried out in order to determine the velocity of the beam particles directly. This can be done by using a fast mechanical chopper to intercept the beam near the source and by observing the quadrupole signal in time-correlation with the chopper period (Zorn and Pearl, 1967).

(2) The beam system can be built more compactly to increase the flux range available at the target. Better thermal insulation of the liquid nitrogen container for the getter pumps and replacement of the titanium filaments by electron beam titanium evaporators make the system operation more efficient.

Suggested experiments:

(1) A more open omegatron system should be designed and tested. Pure gold, platinum, or titanium should be used as surface material. Steady state as well as time response tests are required for a thorough instrument evaluation. Time response measurements can be obtained by rapidly chopping the oxygen beam. The times required to saturate the surfaces need to be determined.

(2) Measurements at different angles of attack need to be made. These can be done in a step-by-step sequence or by mounting the test instrument on flexible bellows so it can be moved continuously.

(3) Of great interest are atom recombination, adsorption, and thermal accommodation measurements on pure thin film surfaces which can be produced under ultrahigh vacuum conditions by electron beam evaporation of the film material. Studies on truly virgin surfaces can be carried out in this manner. Measurements of conductivity changes and contact potential changes should give important information about the adsorption processes.

The omegatron must be removed for these measurements but the quadrupole can be used for beam calibration after it has been cross-calibrated with the omegatron. With the present instrumentation, to avoid the uncertainties arising from a gain change of the secondary electron multiplier, a pulse counting technique instead of the direct current measurement should be employed.

BIBLIOGRAPHY

- Aehlig, Achim, OGO-F-04 Electron Multiplier Study, University of Michigan, College of Engineering, Department of Electrical Engineering, Space Physics Research Laboratory, Ann Arbor, Technical Note 08041-1-T, January 1968.
- Alpert, D., and Buritz, R. S., "Ultra-High Vacuum. II. Limiting Factors on the Attainment of Very Low Pressures," Journal of Applied Physics, 25, No. 2, 202-209, February 1954.
- Bell, R. L., "The Omegatron as a Leak Detector," Journal of Scientific Instruments, 33, 269-272, July 1956.
- Brennan, D., "The Atomization of Diatomic Molecules by Metals," Advances in Catalysis, 15, 1-30, 1964.
- Brennan, D., and Fletcher, P. C., "The Atomization of Hydrogen on Platinum, Gold, and Carbon, and of Oxygen on Platinum," Transactions of the Faraday Society, 56, 1662-1670, 1960.
- Brunée, C., Delgmann, L., and Kronenberger, K., "The Atlas Quadrupole Mass Spectrometer," paper presented at Mass Spectrometry Conference, ASTM Committee E-14, San Francisco, May 1963. Published by Atlas Mess-und-Analysen Technik, GMBH, Bremen.
- CIRA 1965 (COSPAR International Reference Atmosphere 1965), North-Holland Publishing Company, Amsterdam, 1965.
- Clausing, P., "Über die Strömung sehr verdünnter Gase durch Röhren von beliebiger Länge," Annalen der Physik, 5, No. 12, 961-989, 1932.
- Clausing, R. E., "A Large-scale Getter Pumping Experiment Using Vapor Deposited Titanium Films," 1961 Transactions of the Eighth National Vacuum Symposium (American Vacuum Society) Combined with the Second International Congress of Vacuum Science and Technology (International Organization for Vacuum Science and Technology), Luther E. Preuss, editor, Pergamon Press, New York, Volume I, 345-356, 1962.
- DeMarcus, W. C., Knudsen Flow through a Channel with Rough Walls, Technical Report K-1435, Union Carbide Nuclear Company, Union Carbide Corporation, Oak Ridge Gaseous Diffusion Plant, Oak Ridge, Tennessee, 20 October 1959.

- DeMarcus, W. C., The Problem of Knudsen Flow, Part I: General Theory, 5 September 1956; Part II: Solution of Integral Equations with Probability Kernals, 4 October 1956; Part III: Solutions for One-Dimensional Systems, 19 March 1957. Technical Report K-1302, Union Carbide Nuclear Company, Union Carbide and Carbon Corporation, Oak Ridge Gaseous Diffusion Plant, Oak Ridge, Tennessee.
- Dickens, P. G., and Sutcliffe, M. B., "Recombination of Oxygen Atoms on Oxide Surfaces, Part I: Activation Energies of Recombination," Transactions of the Faraday Society, 60, No. 499, 1272-1285, July 1964.
- Dow, W. G., and Reifman, A., Technical Report on the Measurement of Temperature and Pressure in the Ionosphere, Engineering Research Institute, The University of Michigan, July 1946.
- Dushman, Saul, Scientific Foundations of Vacuum Technique, Second Edition, J. M. Lafferty, editor, John Wiley and Sons, Inc., New York, 1962, p. 94.
- Edwards, A. G., "Some Properties of a Simple Omegatron-Type Mass Spectrometer," British Journal of Applied Physics, 6, 44-48, February 1955.
- Ehrlich, Gert, "Molecular Dissociation and Reconstitution on Solids," The Journal of Chemical Physics, 31, No. 4, 1111-1126, October 1959.
- Fite, W. L., and Brackmann, R. T., "Ionization of Atomic Oxygen on Electron Impact," Physical Review, 113, 815-816, 1959.
- Greaves, J. C., and Linnett, J. W., "The Recombination of Oxygen Atoms at Surfaces," Transactions of the Faraday Society, 54, 1323-1330, September 1958.
- Greaves, J. C., and Linnett, J. W., "Recombination of Atoms at Surfaces, Part 4--Theory of Method and Measurement of Atom Concentrations," Transactions of the Faraday Society, 55, 1338-1345, August 1959(a).
- Greaves, J. C., and Linnett, J. W., "Recombination of Atoms at Surfaces, Part 5--Oxygen Atoms at Oxide Surfaces," Transactions of the Faraday Society, 55, 1346-1354, August 1959(b).
- Greaves, J. C., and Linnett, J. W., "Recombination of Atoms at Surfaces, Part 6--Recombination of Oxygen Atoms on Silica from 20°C to 600°C," Transactions of the Faraday Society, 55, 1355-1361, August 1959(c).

- Gross, J., Offerman, D., and von Zahn, U., "Neutral Particle Densities in the Lower Thermosphere as Measured by Mass Spectrometers Above Fort Churchill and Sardinia," paper presented at the Tenth Meeting of COSPAR, London 1967.
- Hedin, A. E., Avery, C. P., and Tschetter, C. D., "An Analysis of Spin Modulation Effects on Data Obtained with a Rocket-Borne Mass Spectrometer," Journal of Geophysical Research, 69, No. 21, 4637-4648, 1 November 1964.
- Hedin, A. E., and Nier, A. O., "A Determination of the Neutral Composition, Number Density and Temperature of the Upper Atmosphere from 120 to 200 Kilometers with Rocket-Borne Mass Spectrometers," Journal of Geophysical Research, 71, 4121-4131, 1966.
- Herzberg, Gerhard, Atomic Spectra and Atomic Structure, Dover Publications, New York, 1944.
- Herzog, Richard F. K., Development, Fabrication, Calibration and Testing of an Atomic Beam System, Final Report, Contract No. NAS5-3251, Geophysics Corporation of America, Bedford, Massachusetts, September 1964.
- Herzog, R. F. K., Research on the Application of the Atomic Beam System, Interim Final Report, Contract No. NAS5-9188, Geophysics Corporation of America, Bedford, Massachusetts, August 1968.
- Kaufman, F., Progress in Reaction Kinetics, Volume I, G. Porter, editor, Pergamon Press, New York, 1-39, 1961.
- Kaufman, Frederick, and Kelso, John R., "Rate Constant of the Reaction $O + 2O_2 \rightarrow O_3 + O_2$," Discussions of the Faraday Society, Chemical Reactions in the Atmosphere, 37, 26-37, 1964.
- Kelso, John R., The Production of Atomic Oxygen by the Thermal Decomposition of Ozone, Report No. 1323, U.S. Army Materiel Command, Ballistic Research Laboratories, Aberdeen Proving Ground, Maryland, June 1966.
- Kieffer, L. J., and Dunn, Gordon H., "Electron Impact Ionization Cross-Section Data for Atoms, Atomic Ions, and Diatomic Molecules: I. Experimental Data," Reviews of Modern Physics, 38, No. 1, 1-35, January 1966.
- Krankowsky, D., Kasprzak, W. T., and Nier, Alfred O., "Mass Spectrometric Studies of the Composition of the Lower Thermosphere during Summer 1967," Journal of Geophysical Research, Space Physics, 73, No. 23, 7291-7306, 1 December 1968.

- Langmuir, I., "A Chemically Active Modification of Hydrogen," Journal of American Chemical Society, 34, No. 9, 1310-1325, September 1912.
- Langmuir, I., "The Dissociation of Hydrogen into Atoms. Part II: Calculation of the Degree of Dissociation and the Heat of Formation," Journal of American Chemical Society, 37, No. 3, 417-458, March 1915.
- Lennard-Jones, J. E., "The Migration and Aggregation of Atoms on Solid Surfaces," Proceedings of the Physical Society A, 49, 140-150, 1937.
- Lighthill, M. J., "Dynamics of a Dissociating Gas, Part I: Equilibrium Flow," Journal of Fluid Mechanics, 2, 1-32, 1957.
- Linnett, J. W., and Marsden, D. G. H., "The Kinetics of the Recombination of Oxygen Atoms at a Glass Surface," Proceedings of the Royal Society A, 234, No. 1199, 489-504, 6 March 1956.
- Linnett, J. W., and Marsden, D. G. H., "The Recombination of Oxygen Atoms at Salt and Oxide Surfaces," Proceedings of the Royal Society A, 234, No. 1199, 504-515, 6 March 1956.
- Mauersberger, K., Müller, D., Offerman, D., and von Zahn, U., "A Mass Spectrometric Determination of the Neutral Constituents in the Lower Thermosphere above Sardinia," Journal of Geophysical Research, 73, 1071-1076, 1968; also published as "Neutral Constituents of the Upper Atmosphere in the Altitude Range of 110 to 160 Km Above Sardinia," Proceedings of the Seventh International Space Science Symposium, Space Research VII, 1150-1158, 1967.
- Meadows, E. B., and Townsend, J. W., "IGY Rocket Measurements of Arctic Atmospheric Composition Above 100 Km," Proceedings of the First International Space Science Symposium, Space Science I, 175-198, 1960.
- Moore, A. D., Heat Transfer Notes for Electrical Engineering, George Wahr Publishing Co., Ann Arbor, Michigan, 1959.
- Morgan, J. E., and Schiff, H. I., Atom Recombination on Surfaces, McGill University, Montreal, Province of Quebec, Canada, November 1965, Technical Report, Contract No. AF19(628)-2425.
- Myerson, A. L., "Mechanisms of Surface Recombination from Step-Function Flows of Atomic Oxygen over Noble Metals," The Journal of Chemical Physics, 42, No. 9, 3270-3276, 1 May 1965.

- Myerson, A. L., Surface Recombination Efficiencies in Flows Containing Step-Function Increases in Atomic Oxygen, AFOSR Scientific Report AFOSR-68-0893, Cornell University, Buffalo, New York, March 1968.
- Nagy, A. F., Spencer, N. U., Niemann, H. B., and Carignan, G. R., Measurements of Atmospheric Pressure, Temperature, and Density at Very High Altitudes, University of Michigan, College of Engineering, Department of Electrical Engineering Space Physics Research Laboratory, Ann Arbor, Final Scientific Report 02804-7-F, August 1961.
- Narcisi, R. S., Schiff, H. I., Morgan, J. E., and Cohen, H. A., "Calibration of a Flyable Mass Spectrometer for N and O Atom Sensitivity," Proceedings of the Third International Space Science Symposium, Space Research III, 1156-1167, 1963.
- Niemann, Hasso B., and Kennedy, Brian C., "Omegatron Mass Spectrometer for Partial Pressure Measurements in Upper Atmosphere," The Review of Scientific Instruments, 37, No. 6, 722-728, June 1966.
- Niemann, Hasso B., and Kreick, John R., Application of a Quasi-Open Ion Source for Neutral Particle Density Measurements in the Thermosphere, University of Michigan, College of Engineering, Department of Electrical Engineering, Space Physics Research Laboratory, Ann Arbor, Scientific Report 07065-3-S, August 1966.
- Nier, Alfred O., "Small General Purpose Double Focusing Mass Spectrometer," The Review of Scientific Instruments, 31, No. 10, 1127-1132, October 1960.
- Nier, Alfred O., Hoffman, J. H., Johnson, C. Y., and Holmes, J. C., "Neutral Composition of the Atmosphere in the 100- to 200-Kilometer Range," Journal of Geophysical Research, 69, No. 5, 979-989, 1 March 1964.
- Nier, Alfred O., Hoffman, J. H., Johnson, C. Y., and Holmes, J. C., "Neutral Constituents of the Upper Atmosphere: The Minor Peaks Observed in a Mass Spectrometer," Journal of Geophysical Research, 69, No. 21, 4629-4636, 1 November 1964.
- Offerman, D., and von Zahn, U., "Studie über ein Massenfilter zur Anwendung in Raketen und Satelliten," Forschungsberichte des Landes Nordrhein-Westfalen, Nr. 1400, Westdeutscher Verlag, Köln und Opladen, 1964.
- Paul, W., and Raether, M., "Das elektrische Massenfilter," Zeitschrift für Physik, 140, 262-273, 1955.

- Paul, W., Reinhard, H. P., and von Zahn, U., "Das elektrische Massenfilter als Massenspektrometer und Isotopentrenner," Zeitschrift für Physik, 152, 143-182, 1958.
- Philbrick, C. R., Narcisi, R. S., and Wlodyka, R. A., "Preliminary Results of the Neutral Atmospheric Composition on the OVI-15 Satellite," Transactions American Geophysical Union, 49, No. 4, 722, December 1968.
- Pokhunkov, A. A., "Mass-Spectrometer Investigations of the Structural Parameters of the Earth's Atmosphere at Altitudes from 100 to 210 Km," Planetary Space Science, 9, 269-279, 1962.
- Ramsey, Norman F., Molecular Beams, Oxford University Press, London, 1963.
- Reber, Carl, "Data from Explorer 17 on Composition of the Upper Atmosphere," Journal of Geophysical Research, 69, No. 21, 4681-4685, 1 November 1964.
- Reber, C. A. and Hall, L. G., A Double-Focusing Magnetic Mass Spectrometer for Satellite Use, NASA Technical Note TN D-3211, Washington, D.C., March 1966.
- Reber, C. A., and Harpold, D. N., "Mass Spectrometric Measurements of Atomic Oxygen in the Earth's Upper Atmosphere," paper presented at the 48th Annual Meeting of the American Geophysical Union, Washington, D.C., 1967.
- Schaefer, E. J., and Nichols, M. H., "Mass Spectrometer for Upper Air Measurements," American Rocket Society Journal, 31, 1773-1776, 1961.
- Schaefer, E. J., and Nichols, M. H., "Upper Air Neutral Composition Measurements by a Mass Spectrometer," Journal of Geophysical Research, 69, No. 21, 4649-4660, 1 November 1964.
- Schissel, P. O., and Trulson, O. C., "Mass-Spectrometric Study of the Oxidation of Tungsten," The Journal of Chemical Physics, 43, No. 2, 737-743, 15 July 1965.
- Schultz, F. V., Spencer, N. W., and Reifman, A., Atmospheric Pressure and Temperature Measurements Between the Altitudes of 40 and 110 Kilometers, Upper Atmosphere Report No. 2, University of Michigan Research Institute, Ann Arbor, July 1948.
- Sommer, H., Thomas, H. A., and Hipple, J. A., "The Measurement of e/m by Cyclotron Resonance," Physical Review, 32, No. 5, 697-702, 1 June 1951.

- Spencer, N. W., Brace, L. H., Niemann, H. B., Carignan, G. R., and Taeusch, D. R., "Some Energy Implications of Direct Measurements of Thermospheric Structure," Proceedings of the Sixth International Space Science Symposium, Space Research VI, May 1965.
- Spencer, N. W., and Reber, C. A., "A Mass Spectrometer for an Aeronomy Satellite," Proceedings of the Third International Space Science Symposium, Space Research III, 1151-1155, 1963.
- Taeusch, D. R., and Carignan, G. R., NASA 18.05 Thermosphere Probe Experiment, University of Michigan, College of Engineering, Department of Electrical Engineering, Space Physics Research Laboratory, Ann Arbor, Sounding Rocket Flight Report 07065-5-R, October 1967.
- Taeusch, D. R., and Carignan, G. R., NASA 18.06 Thermosphere Probe Experiment, University of Michigan, College of Engineering, Department of Electrical Engineering, Space Physics Research Laboratory, Ann Arbor, Sounding Rocket Flight Report 07065-6-R, January 1968.
- Taeusch, D. R., and Carignan, G. R., NASA 18.22 Thermosphere Probe Experiment, University of Michigan, College of Engineering, Department of Electrical Engineering, Space Physics Research Laboratory, Ann Arbor, Sounding Rocket Flight Report 07065-7-R, June 1967.
- Taeusch, D. R., Carignan, G. R., Nagy, A. F., and Niemann, H. B., Diurnal Survey of the Thermosphere, University of Michigan, College of Engineering, Department of Electrical Engineering, Space Physics Research Laboratory, Ann Arbor, Final Report 07446-1-F, October 1967.
- Taeusch, D. R., Smith, R. E., Niemann, H. B., Carignan, G. R., and Ballance, Y. O., "Diurnal Survey of the Thermosphere, I: Neutral Particle Results," Proceedings of the Eighth International Space Science Symposium, Space Research VIII, 1967.
- Townsend, J. W., Jr., "Radiofrequency Mass Spectrometer for Upper Air Research," The Review of Scientific Instruments, 23, 538-541, 1952.
- Turner, B. R., Compton, D. M. J., and McGowan, J. Wm., Electronic and Ionic Reactions in Atmospheric Gases, General Atomic Division of General Dynamics, San Diego, California, 14 November 1966, DASA-1863, GA-7419, Technical Report, Contract No. DA-49-146-XZ-354.
- von Zahn, U., "Mass Spectrometric Measurements of Atomic Oxygen in the Upper Atmosphere: A Critical Review," Journal of Geophysical Research, 72, No. 23, 5933-5937, 1 December 1967.

- Wagener, J. S., and Marth, P. T., "Analysis of Gases at Very Low Pressures by Using the Omegatron Spectrometer," Journal of Applied Physics, 28, No. 9, 1027-1030, September 1957.
- Weast, Robert C., Selby, Samuel M., and Hodgman, Charles D., editors, Handbook of Chemistry and Physics, 46th edition, The Chemical Rubber Company, Cleveland, 1965.
- Wise, Henry, Wood, Bernard, J., and Rajapakse, Yapa, "Heat Transfer in Reacting Gases: Thermal Conductivity and Accommodation Coefficient Measurements in Gas Mixture of O and O₂," The Physics of Fluids, 9, No. 7, 1321-1327, July 1966.
- Zorn, Jens C., and Pearl, John C., A Feasible Satellite Experiment for Gas Molecule-Solid Surface Interaction Studies, University of Michigan, College of Engineering, Department of Electrical Engineering, Space Physics Research Laboratory, Ann Arbor, Final Report 08700-1-F, October 1967.

APPENDIX A

ATOMIC OXYGEN GENERATION BY THERMAL DISSOCIATION ON HOT TUNGSTEN

A simple technique to generate atomic oxygen by thermal dissociation is the method used by Schissel and Trulson (1965) for oxidation studies of tungsten. Schissel and Trulson placed a hot tungsten ribbon in a molecular oxygen atmosphere and measured the gas composition in the immediate vicinity of the walls with a mass spectrometer. From the measured data they computed rate constants for the dissociation rate and the oxidation rates. Based on their model, flow rates of atomic oxygen and tungsten oxides are computed for an assumed surface temperature of the tungsten of 2800°K. The following rate constants are obtained for the most important reactions.



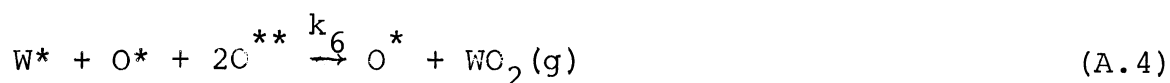
$$k_3 = 5 \times 10^{28} \exp(-25.9) = 2.94 \times 10^{17} \text{ cm}^{-2} \text{ sec}^{-1}$$



$$k_4 = 5 \times 10^{28} \exp(-16) = 5.74 \times 10^{21} \text{ cm}^{-2} \text{ sec}^{-1}$$



$$k_5 = 1.2 \times 10^{29} \exp(-20.5) = 1.51 \times 10^{20} \text{ cm}^{-2} \text{ sec}^{-1}$$



$$k_6 = 4.6 \times 10^{28} \exp(-18.35) = 5.04 \times 10^{19} \text{ cm}^{-2} \text{ sec}^{-1}$$



$$k_7 = 1.8 \times 10^{28} \exp(-18.35) = 1.97 \times 10^{20} \text{ cm}^{-2} \text{ sec}^{-1}$$



$$\frac{k_9}{k_8} = 7.2 \times 10^6 \exp(-11.32) = 86.5.$$

The symbols chosen are those used by Schissel and Trulson. The single asterisk (*) denotes the surface species in the first adsorption layer and the double asterisk (**) denotes the surface species in the second adsorption layer. The postscript (g) denotes the gaseous species and S* and S** denote empty surface sites. The adsorption on the first and second layer is assumed to occur with unity efficiency according to the relation



and



where \bar{U} is the impact rate of molecules on the tungsten surface.

By using the same impact flux that was used by Schissel and Trulson ($\phi(O_2) = 7.5 \times 10^{16} \text{ cm}^{-2} \text{ sec}^{-1}$) which corresponds to an impact pressure of 2.1×10^{-4} torr, the fractional coverages θ_1 and θ_2 for the first and second layer are computed.

From Equations 12 and 13 of Schissel and Trulson

$$\theta_1 = \frac{1}{2}(2 + 1.96) \left\{ 1 - \left[1 - \left(\frac{2}{2 + 1.96} \right)^2 \right]^{\frac{1}{2}} \right\} = 0.273 \quad (\text{A.10})$$

$$\frac{\theta_2}{\theta_1} \approx \left(\frac{\phi(O_2)}{k_4} \right)^{\frac{1}{2}} = \left(\frac{7.5 \times 10^{16}}{5.74 \times 10^{21}} \right)^{\frac{1}{2}} = 3.6 \times 10^{-3} \quad (\text{A.11})$$

and therefore

$$\theta_2 = 9.84 \times 10^{-4}. \quad (\text{A.12})$$

The atomic oxygen flow rate is obtained,

$$\begin{aligned} r_O &= r_3 + r_5 = \theta_1 k_3 + \theta_2 k_5 = 8.02 \times 10^{16} + 1.483 \times 10^{17} \\ &= 2.285 \times 10^{17} \text{ cm}^{-2} \text{ sec}^{-1}. \end{aligned} \quad (\text{A.13})$$

The flux rate agrees with the rates shown in Figure 7 of Schissel and Trulson but this is clearly too high since the evaporation rate of atomic oxygen exceeds the condensation rate of molecular oxygen. The maximum evaporation rate which can be expected is

$$r_O = 1.5 \times 10^{17} \text{ cm}^{-2} \text{ sec}^{-1}. \quad (\text{A.14})$$

A possible explanation for this disagreement is found in the

uncertainty of the rate constants. However, in the calculations of θ_2 the atomic oxygen flow from the second layer was neglected. If it is included in the computations, the flux balance equation can be written

$$\phi(O_2) (\theta_1 - \theta_2)^2 = \theta_2^2 k_4 + \frac{1}{2} \theta_2 k_5. \quad (A.15)$$

The left side of Equation (A.15) is the rate of condensation on the second layer. The first term on the right side is the rate at which oxygen molecules evaporate and the second term on the right side is the rate of evaporation of oxygen atoms. From Equation (A.15), θ_2 is obtained.

$$\theta_2 = \frac{1}{2} \frac{2\theta_1 + \frac{k_5}{\phi(O_2)}}{1 - \frac{k_4}{\phi(O_2)}} \left\{ 1 - \left[1 - \frac{4 \left(1 - \frac{k_4}{\phi(O_2)} \right) \theta_1^2}{\left(2\theta_1 + \frac{k_5}{\phi(O_2)} \right)^2} \right]^{\frac{1}{2}} \right\} \quad (A.16)$$

and since $\frac{k_5}{\phi(O_2)} \gg 1$ and $\frac{k_4}{\phi(O_2)} \gg 1$

$$\theta_2 \approx \frac{1}{4} \frac{k_5}{k_4} \left[\left(1 + \frac{16 \theta_1^2 k_4 \phi(O_2)}{k_5^2} \right)^{\frac{1}{2}} - 1 \right]. \quad (A.17)$$

By substituting numerical values

$$\theta_2 = 0.74 \times 10^{-4}, \quad (A.18)$$

which is more than an order-of-magnitude below the previously computed value and shows that at 2800°K the oxygen coverage on the second layer is governed by the evaporation rate of atomic oxygen. The newly computed evaporation rate from the second layer is then

$$r_5 = 0.74 \times 10^{-4} \times 1.51 \times 10^{20} = 1.118 \times 10^{16} \text{ cm}^{-2} \text{ sec}^{-1} \quad (\text{A.19})$$

and therefore the total atomic oxygen flow rate is

$$r_o = 9.138 \times 10^{16} \text{ cm}^{-2} \text{ sec}^{-1}. \quad (\text{A.20})$$

The rate of recombined atomic oxygen is

$$r_4 = \theta_2^2 k_4 = 0.74^2 \times 10^{-8} \times 5.74 \times 10^{21} = 3.14 \times 10^{13} \text{ cm}^{-2} \text{ sec}^{-1}. \quad (\text{A.21})$$

The dissociation efficiency is now less than unity

$$\frac{r_o}{2 \phi(O_2)} = \frac{9.138 \times 10^{16}}{1.5 \times 10^{17}} = 0.61. \quad (\text{A.22})$$

The rates of oxide evaporation are obtained from Equations 16 and 17 of Schissel and Trulson.

$$r_6 = k_6 \theta_1 \theta_2^2 + r_7 \frac{k_9}{k_8} \quad (\text{WO}_2) \quad (\text{A.23})$$

$$r_7 = k_7 \theta_1 \theta_2^2 \frac{1}{1 + \frac{k_9}{k_8}} \quad (\text{WO}_3). \quad (\text{A.24})$$

And after substitution, the numerical value is obtained.

$$r_6 = 3.674 \times 10^{11} \text{ cm}^{-2} \text{ sec}^{-1} \quad (\text{A.25})$$

$$r_7 = 3.67 \times 10^9 \text{ cm}^{-2} \text{ sec}^{-1}. \quad (\text{A.26})$$

These rates are extremely low and do not agree with the measured values of Schissel and Trulson. Also, about 39% of the incoming molecular oxygen flux is unaccounted for in

this model. The required balance can be obtained by adjusting the rate constants k_3 and k_5 or by assuming that the condensation efficiency is less than unity.

Based on this model, rates of atomic oxygen and tungsten oxide formations were computed for a number of different primary flux rates. The results normalized to the primary flux are shown in Figure 3.1. The computations can be valued only as order-of-magnitude estimates because of the model inadequacy.

APPENDIX B

DETERMINATION OF THE WALL TEMPERATURE OF THE ATOMIC OXYGEN SOURCE

The double wall atomic oxygen source, shown in Figure 3.6, is chosen for efficient dissociation of oxygen molecules and effective trapping of tungsten oxide. In order to keep the walls of the titanium envelope near room temperature while the tungsten filament in the center is at 2800°K or 3000°K, water flows continuously through the double wall tube system.

In the following computations, which were used to aid in the design of the source, it is assumed that the system can be approximated by two infinitely long concentric cylinders. The tungsten filament forms the inner cylinder, and the titanium tube forms the outer cylinder. The net heat flow W into the outer cylinder radiated by the inner cylinder is given by Moore (1959):

$$W = A_1 (X_1 - X_2) e \quad (B.1)$$

where

$$e = \frac{e_1 e_2}{e_1 \frac{A_1}{A_2} + e_2 - e_1 e_2 \frac{A_1}{A_2}} \quad (B.2)$$

e is the effective emissivity of the system,
 e_1, e_2 are the emissivities of the inner and the outer cylinders,
 A_1, A_2 are the respective surface areas,
 X_1, X_2 are the radiated energies of the tungsten filament and the titanium tube.

In general,

$$X = 5.75 \times 10^4 \left(\frac{T}{1000} \right)^4 \text{ watt m}^{-2} \quad (\text{B.3})$$

where T is the temperature of the radiating surface. For tungsten at 3000°K , $e_1 = 0.334$ and for titanium $e_2 \approx 0.5$ (Weast, Selby, and Hodgman, 1965). The heat flow through the tube walls is given as

$$W = \frac{A_2}{d} q (T_2 - T_3) \quad (\text{B.4})$$

where

d is the wall thickness of the titanium tube,
 q is the heat conductivity, and
 T_2, T_3 are the inner and outer wall temperatures of the titanium tube.

For titanium, $q = 15.1 \text{ watts m}^{-1}\text{ }^\circ\text{C}^{-1}$. The wall temperature T_2 is obtained from Equations B.1 and B.4 since $X_1 \gg X_2$,

$$T_2 \approx \frac{A_1}{A_2} X_1 d \frac{e}{q} + T_3. \quad (\text{B.5})$$

The diameter of the tungsten filament is 0.005 m, the inside diameter of the titanium tube is 0.011 m, and the wall thickness is 0.001 m. We have

$$e = \frac{0.335 \times 0.5}{0.334 \times \frac{25}{121} + 0.5 - 0.334 \times 0.5 \times \frac{25}{121}} = 0.313. \quad (\text{B.6})$$

For a filament temperature of 3000°K

$$x_1 = 5.75 \times 10^4 \left(\frac{3000}{1000} \right)^4 = 4.66 \times 10^6 \text{ watts m}^{-2} \quad (\text{B.7})$$

and

$$T_2 = \frac{25}{121} \times 10^{-3} \times 4.66 \times 10^6 \times \frac{0.313}{15.1} + T_3 = 20 + T_3. \quad (\text{B.8})$$

The cooling water temperature varies between 4°C and 10°C, and therefore T_2 varies between 297°K and 303°K. This temperature can be maintained only if the oxide layer on the tube walls remains sufficiently thin.

APPENDIX C

DERIVATION OF EQUATIONS RELATING ATOMIC AND MOLECULAR FLUXES OF THE OXYGEN BEAM TO THE PARTICLE DENSITIES, NET RECOMBINATION, AND ADSORPTION INSIDE THE OMEGATRON CHAMBER

Assuming that the fractional dissociation and therefore the flux ratios $\phi(O)/\phi(O_2)$ in the beam are known, and that the absolute flux at the omegatron orifice is measurable as described in Chapter III, we can relate these values and the measured particle densities in the omegatron to obtain the net atom recombination and the net atom adsorption. Because of the atomic oxygen absorption and the possible formation of new gaseous compounds, the incoming and outgoing fluxes are not balanced. The incoming flux consists of atomic and molecular oxygen during dissociation and of molecular oxygen only without dissociation. The outgoing flux consists of atomic oxygen which was not recombined or absorbed, of molecular oxygen which is the sum of the incoming molecular oxygen and the recombined atomic oxygen, and of the gas formed on the surface of the chamber by the reaction of atomic oxygen with surface adsorbed species, i.e., carbon, hydrogen, and perhaps nitrogen. The outgoing particle flux is therefore

$$\sum_{\ell} \phi_{\Omega out}(\ell) = \phi_{\Omega out}(O) + \phi_{\Omega out}(O_2) + \sum_{\ell} \phi_p(\ell) \quad (C.1)$$

where the last term on the right side contains all gaseous products formed on the surface. If the particles in the omegatron chamber have a Maxwellian velocity distribution, the particle densities in the chamber are related to the flux by simple kinetic theory.

$$\phi_{\Omega\text{out}}(\text{O}) = \frac{1}{4} n_{\Omega\text{h}}(\text{O}) \bar{v}_{\Omega\text{h}}(\text{O}) \quad (\text{C.2})$$

$$\phi_{\Omega\text{out}}(\text{O}_2) = \frac{1}{4} n_{\Omega\text{h}}(\text{O}_2) \bar{v}_{\Omega\text{h}}(\text{O}_2) + \frac{1}{4} n_{\Omega\text{R}}(\text{O}_2) \bar{v}_{\Omega\text{R}}(\text{O}_2) \quad (\text{C.3})$$

$$\sum_{\ell} \phi_{\text{p}}(\ell) = \frac{1}{4} \sum_{\ell} n_{\Omega\text{h}}(\ell) \bar{v}_{\Omega\text{h}}(\ell). \quad (\text{C.4})$$

The two terms on the right side of Equation (C.3) are the contributions from the incoming molecular oxygen flux and the recombined atomic oxygen. The particle density caused by the incoming molecular oxygen is $n_{\Omega\text{h}}(\text{O}_2)$, and $n_{\Omega\text{R}}(\text{O}_2)$ results from recombined atomic oxygen. The corresponding average thermal velocities are $\bar{v}_{\Omega\text{h}}(\text{O})$, $\bar{v}_{\Omega\text{h}}(\text{O}_2)$, $\bar{v}_{\Omega\text{R}}(\text{O}_2)$. In general

$$\bar{v}_i \equiv \sqrt{\frac{8kT_i}{\pi m_i}}. \quad (\text{C.5})$$

The letter ℓ is used in Equation (C.4) to denote the different products which can be formed on the surface.

If R is the fraction of the incoming atomic oxygen flux which recombines to molecular oxygen, δ_{ℓ} is the fraction of the incoming atomic oxygen flux which forms another compound (i.e., CO , or, H_2O), and \bar{c} is the fraction of the atomic

oxygen flux which is absorbed by the surface, we can write the following relations,

$$\phi_{\Omega\text{out}}(\text{O}_2) = \phi_{\Omega\text{h}}(\text{O}_2) + \phi_{\Omega\text{h}}(\text{O}) \frac{R}{2} \quad (\text{C.6})$$

$$\phi_{\Omega\text{h}}(\text{O}) \frac{R}{2} = \frac{1}{4} n_{\Omega\text{R}}(\text{O}_2) \bar{v}_{\Omega\text{R}}(\text{O}_2) \quad (\text{C.7})$$

$$\phi_{\Omega\text{h}}(\text{O}_2) = \frac{1}{4} n_{\Omega\text{h}}(\text{O}_2) \bar{v}_{\Omega\text{h}}(\text{O}_2) \quad (\text{C.8})$$

$$\phi_{\Omega\text{h}}(\text{O}) \delta_\ell = \frac{1}{4} \sum_\ell \left(n_{\Omega\text{h}}(\ell) \bar{v}_{\Omega\text{h}}(\ell) \right) \quad (\text{C.9})$$

$$\phi_{\Omega\text{h}}(\text{O}) \bar{c} = \sum_m \phi_{\Omega\text{ads}}(\text{O}) \quad (\text{C.10})$$

$$\frac{1}{4} n_{\Omega\text{h}}(\text{O}) \bar{v}_{\Omega\text{h}}(\text{O}) = \phi_{\Omega\text{h}}(\text{O}) (1 - R - \bar{c} - \delta_\ell) . \quad (\text{C.11})$$

By noting that only the sum of the molecular oxygen densities in the omegatron is detected

$$n_{\Omega\text{T}}(\text{O}_2) = n_{\Omega\text{h}}(\text{O}_2) + n_{\Omega\text{R}}(\text{O}_2) , \quad (\text{C.12})$$

and the quantity R is obtained from Equations (C.7) and (C.8).

$$R = \frac{n_{\Omega\text{T}}(\text{O}_2) \bar{v}_{\Omega\text{R}}(\text{O}_2)}{2 \phi_{\Omega\text{h}}(\text{O})} - 2 \frac{\phi_{\Omega\text{h}}(\text{O}_2) \bar{v}_{\Omega\text{R}}(\text{O}_2)}{\phi_{\Omega\text{h}}(\text{O}) \bar{v}_{\Omega\text{h}}(\text{O}_2)} . \quad (\text{C.13})$$

It is useful to express R in terms of density ratios and flux ratios rather than in terms of absolute quantities.

For the incoming flux we have

$$K \phi_{\Omega\text{C}}(\text{O}_2) = \frac{1}{2} \phi_{\Omega\text{h}}(\text{O}) + \phi_{\Omega\text{h}}(\text{O}_2) = K \frac{1}{4} n_{\Omega\text{C}}(\text{O}_2) \bar{v}_{\Omega\text{C}}(\text{O}_2) \quad (\text{C.14})$$

where K is the loss factor of molecular oxygen in the beam source. It is defined by Equation (3.64) of Chapter III. Solving Equation (C.14) for $\phi_{\Omega h}(0)$ and substituting into Equation (C.13) yields

$$R = \frac{n_{\Omega T}(O_2) \bar{v}_{\Omega R}(O_2)}{K n_{\Omega C}(O_2) \bar{v}_{\Omega C}(O_2)} \left(1 + 2 \frac{\phi_{\Omega h}(O_2)}{\phi_{\Omega h}(0)} \right) - 2 \frac{\phi_{\Omega h}(O_2)}{\phi_{\Omega h}(0)} \frac{\bar{v}_{\Omega R}(O_2)}{v_{\Omega h}(O_2)}. \quad (C.15)$$

\bar{C} is obtained from Equations (C.9), (C.11) and (C.13)

$$\bar{C} = 1 - R - \delta_{\ell} - \frac{1}{4} \frac{n_{\Omega h}(0) \bar{v}_{\Omega h}(0)}{\phi_{\Omega h}(0)} \quad (C.16)$$

$$= 1 + 2 \frac{\bar{v}_{\Omega R}(O_2) \phi_{\Omega h}(O_2)}{\bar{v}_{\Omega h}(O_2) \phi_{\Omega h}(0)} -$$

$$\left(1 + 2 \frac{\phi_{\Omega h}(O_2)}{\phi_{\Omega h}(0)} \right) \left[\frac{n_{\Omega T}(O_2) \bar{v}_{\Omega R}(O_2)}{K n_{\Omega C}(O_2) \bar{v}_{\Omega C}(O_2)} + \frac{1}{2} \frac{n_{\Omega h}(0) \bar{v}_{\Omega h}(0)}{K n_{\Omega C}(O_2) \bar{v}_{\Omega C}(O_2)} + \sum_{\ell} \left(\frac{n_{\Omega h}(\ell) \bar{v}_{\Omega h}(\ell)}{K n_{\Omega C}(O_2) \bar{v}_{\Omega C}(O_2)} \right) \right].$$

The fractions of the molecular oxygen resulting from recombination and from the incoming molecular oxygen are obtained from Equations (C.8), (C.12) and (C.14).

$$\frac{n_{\Omega h}(O_2)}{n_{\Omega T}(O_2)} = \frac{K n_{\Omega C}(O_2) \bar{v}_{\Omega C}(O_2)}{n_{\Omega T}(O_2) \bar{v}_{\Omega h}(O_2)} \frac{1}{1 + \frac{1}{2} \frac{\phi_{\Omega h}(0)}{\phi_{\Omega h}(O_2)}} \quad (C.17)$$

and

$$\frac{n_{\Omega R}(O_2)}{n_{\Omega T}(O_2)} = 1 - \frac{n_{\Omega h}(O_2)}{n_{\Omega T}(O_2)} . \quad (C.18)$$

Expressing the average velocities in terms of the kinetic temperature and noting that

$$1 + 2 \frac{\phi_{\Omega h}(O_2)}{\phi_{\Omega h}(O)} = \frac{1}{T} \quad (C.19)$$

we have

$$R = \frac{n_{\Omega T}(O_2)}{K n_{\Omega C}(O_2)} \sqrt{\frac{T_{\Omega R}(O_2)}{T_{\Omega C}(O_2)}} \frac{1}{T} - \sqrt{\frac{T_{\Omega R}(O_2)}{T_{\Omega h}(O_2)}} \frac{1 - T}{T} \quad (C.20)$$

$$\bar{C} = 1 + \sqrt{\frac{T_{\Omega R}(O_2)}{T_{\Omega h}(O_2)}} \frac{1 - T}{T} - \frac{1}{T} \left[\frac{n_{\Omega T}(O_2)}{K n_{\Omega C}(O_2)} \sqrt{\frac{T_{\Omega R}(O_2)}{T_{\Omega C}(O_2)}} + \right.$$

$$\left. \frac{1}{\sqrt{2}} \frac{n_{\Omega h}(O)}{K n_{\Omega C}(O_2)} \sqrt{\frac{T_{\Omega h}(O)}{T_{\Omega C}(O_2)}} + \sum_{\ell} \left(\frac{n_{\Omega h}(\ell)}{K n_{\Omega C}(O_2)} \sqrt{\frac{m(O_2) T_{\Omega h}(\ell)}{m(\ell) T_{\Omega C}(O_2)}} \right) \right] \quad (C.21)$$

and

$$\frac{n_{\Omega h}(O_2)}{n_{\Omega T}(O_2)} = \frac{K n_{\Omega C}(O_2)}{n_{\Omega T}(O_2)} \sqrt{\frac{T_{\Omega C}(O_2)}{T_{\Omega h}(O_2)}} (1 - T) . \quad (C.22)$$

If all particles in the omegatron chamber accommodate thermally to the wall temperature, $T_{\Omega C}(O_2) = T_{\Omega h}(O_2) = T_{\Omega R}(O_2) = T_{\Omega h}(\ell) = T_{\Omega}$

then

$$R = \frac{n_{\Omega T}(O_2)}{K n_{\Omega C}(O_2)} \frac{1}{T} - \frac{1 - T}{T} \quad (C.23)$$

$$\bar{C} = \frac{1}{T} \left\{ 1 - \left[\frac{n_{\Omega T}(O_2)}{K n_{\Omega C}(O_2)} + \frac{1}{\sqrt{2}} \frac{n_{\Omega h}(O)}{K n_{\Omega C}(O_2)} + \sum_{\ell} \frac{n_{\Omega h}(\ell)}{K n_{\Omega C}(O_2)} \sqrt{\frac{m(O_2)}{m(\ell)}} \right] \right\} \quad (C.24)$$

and

$$\frac{n_{\Omega h}(O_2)}{n_{\Omega T}(O_2)} = \frac{K n_{\Omega C}(O_2)}{n_{\Omega T}(O_2)} (1 - T). \quad (C.25)$$

It is useful to define the total fraction of atomic oxygen which is lost by absorption or by formation of another gaseous compound to be C, where

$$C = \frac{1}{T} \left[1 - \frac{n_{\Omega T}(O_2)}{K n_{\Omega C}(O_2)} + \frac{1}{\sqrt{2}} \frac{n_{\Omega h}(O)}{K n_{\Omega C}(O_2)} \right]. \quad (C.26)$$

APPENDIX D

DERIVATION OF RELATIONS BETWEEN INCOMING AND OUTGOING MASS FLUXES IN THE OMEGATRON SYSTEM BY TAKING INTO CONSIDERATION RECOMBINATION, PERMANENT ADSORPTION OF ATOMIC OXYGEN, AND THE FORMATION OF NITROUS OXIDE

Suppose that there is a finite probability that molecular nitrogen and atomic oxygen can recombine on the walls of the omegatron system and form nitrous oxide (N_2O). In principle, this can occur in three ways:

- (1) Gaseous atomic oxygen collides with adsorbed molecular nitrogen and forms N_2O , or
- (2) Gaseous molecular nitrogen collides with adsorbed atomic oxygen and forms N_2O , and
- (3) Adsorbed molecular nitrogen and atomic oxygen collide on the surface because of migrations of one or both of the constituents and form N_2O .

The following derivations apply for free molecular flow and steady state conditions. Surface recombination of atomic oxygen and formation of N_2O by surface migration of both constituents are neglected.

We let p be the probability of escape after one bounce,

γ_{11} be the recombination coefficient for atomic oxygen, γ_{12} and γ_{21} be the probabilities that gaseous atomic oxygen forms N_2O when it collides with adsorbed nitrogen, and that gaseous molecular nitrogen forms N_2O when it collides with adsorbed atomic oxygen. By assuming that the permanent absorption of atomic oxygen on the walls is independent of time and any permanently adsorbed atomic oxygen could disappear without trace and change of the surface character, the atomic oxygen flux $\phi_2(O)$ which flows out of the omegatron chamber is given by

$$\begin{aligned} \phi_2(O) = & p \phi_1(O) (1-\gamma_{11}-\gamma_{12}-\gamma_{21}-\lambda) + [p \phi_1(O) (1-p)] \\ & [(1-\gamma_{11}-\gamma_{12}-\gamma_{21}-\lambda)^2] + \dots + [p \phi_1(O) (1-p)^{m-1}] \\ & [(1-\gamma_{11}-\gamma_{12}-\gamma_{21}-\lambda)^m] + \dots \end{aligned} \quad (D.1)$$

where $\phi_1(O)$ is the incoming atomic oxygen flux and λ is the probability that atomic oxygen will be permanently adsorbed during a collision. The terms of the right side of Equation (D.1) are the fraction of the total incoming flux which leaves after the first, second, and the m^{th} collision. Similarly, the outgoing molecular oxygen flux $\phi_2(O_2)$, caused by recombination of atomic oxygen, is given by

$$\begin{aligned} 2 \phi_2(O_2) = & \phi_1(O) \gamma_{11} + \phi_1(O) (1-p) (1-\gamma_{11}-\gamma_{12}-\gamma_{21}-\lambda) \gamma_{11} + \\ & \dots + \phi_1(O) (1-p)^{m-1} (1-\gamma_{11}-\gamma_{12}-\gamma_{21}-\lambda)^{m-1} \gamma_{11} + \\ & \dots + \end{aligned} \quad (D.2)$$

and the outgoing molecular nitrogen flux is given by

$$\phi_2(N_2) = p \phi_1(N_2) (1-\gamma_{12}-\gamma_{21}) + p \phi_1(N_2) (1-p) (1-\gamma_{12}-\gamma_{21})^2 + \dots \quad (D.3)$$

where $\phi_1(N_2)$ is the incoming molecular nitrogen flux. The outgoing nitrous oxide flux is

$$\begin{aligned} \phi_2(N_2O) = & \phi_1(O) \gamma_{12} + \phi_1(O) (1-p) (1-\gamma_{11}-\gamma_{12}-\gamma_{21}-\lambda) \gamma_{12} + \\ & \dots + \phi_1(O) (1-p)^{m-1} (1-\gamma_{11}-\gamma_{12}-\gamma_{21}-\lambda)^{m-1} \gamma_{12} + \\ & \dots + \phi_1(N_2) \gamma_{21} + \phi_1(N_2) (1-p) (1-\gamma_{12}-\gamma_{21}) \gamma_{21} + \\ & \dots + \phi_1(N_2) (1-p)^{m-1} (1-\gamma_{12}-\gamma_{21})^{m-1} \gamma_{21} + \dots \end{aligned} \quad (D.4)$$

Equations (D.1) through (D.4) are easily summed, and we obtain

$$\phi_2(O) = \phi_1(O) \frac{1}{1 + \frac{\gamma_{11} + \gamma_{12} + \gamma_{21} + \lambda}{(1 - \gamma_{11} - \gamma_{12} - \gamma_{21} - \lambda) p}} \quad (D.5)$$

$$\phi_2(O_2) = \frac{1}{2} \phi_1(O) \frac{1}{1 + \frac{(1-p)(\gamma_{12} + \gamma_{21} + \lambda) + p(1-\gamma_{11})}{\gamma_{11}}} \quad (D.6)$$

$$\phi_2(N_2) = \phi_1(N_2) \frac{1}{1 + \frac{\gamma_{12} + \gamma_{21}}{(1 - \gamma_{12} - \gamma_{21}) p}} \quad (D.7)$$

$$\begin{aligned} \phi_2(N_2O) = & \phi_1(O) \frac{1}{1 + \frac{(1-p)(\gamma_{11} + \lambda) + p(1-\gamma_{12}-\gamma_{21})}{\gamma_{12}}} + \\ & \phi_1(N_2) \frac{1}{1 + \frac{p(1-\gamma_{12}-\gamma_{21})}{\gamma_{21}}} \end{aligned} \quad (D.8)$$

Since surface recombination of O and surface formation of N₂O are neglected, we have

$$\gamma_{11} = 2 \theta' \kappa_D \quad (D.9)$$

$$\gamma_{12} = \theta'' \omega_{12} \quad (D.10)$$

$$\gamma_{21} = \theta' \omega_{21} \quad (D.11)$$

where θ' and θ'' are the fractional surface coverages of atomic oxygen and molecular nitrogen, κ_D is the probability of recombination for an oxygen atom when it collides with an atom adsorbed on the surface, and ω_{12} and ω_{21} are the probabilities of forming N₂O from gaseous atomic oxygen and adsorbed molecular nitrogen and gaseous molecular nitrogen and adsorbed atomic oxygen.

To determine the fractional coverages θ' and θ'' , we assume that the gas in the omegatron chamber is in quasi-equilibrium with the walls. Equating then the rate of adsorption to the rate of desorption and recombination, we can write

$$\phi_2(O) (1 - \theta' - \theta'') a_1 = b_1 \theta' + \phi_2(O) \theta' \kappa_D + \phi_2(N_2) \theta' \omega_{21} \quad (D.12)$$

and

$$\phi_2(N_2) (1 - \theta' - \theta'') a_2 = b_2 \theta'' + \phi_2(O) \theta'' \omega_{12} \quad (D.13)$$

where the terms on the left side of Equations (D.12) and (D.13) are the adsorption rates, and a_1 and a_2 are the sticking

probabilities for atomic oxygen and molecular nitrogen. In Equation (D.12) the first term on the right side is the rate of desorption of atomic oxygen, the second term is the rate of recombination of atomic oxygen, and the third term is the rate of formation of nitrous oxide. Equation (D.13) is written in the same sequence.

After rearranging we have

$$\phi_2(O) a_1 = [b_1 + (a_1 + \kappa_D) \phi_2(O) + \omega_{21} \phi_2(N_2)] \theta' + a_1 \phi_2(O) \theta'' \quad (D.14)$$

$$\phi_2(N_2) a_3 = [b_2 + a_2 \phi_2(N_2) + \omega_{12} \phi_2(O)] \theta'' + a_2 \phi_2(N_2) \theta' \quad (D.15)$$

We find θ' and θ'' by solving Equations (D.14 and (D.15) simultaneously:

$$\theta' = \frac{a_1 \phi_2(O) [b_2 + \omega_{12} \phi_2(O)]}{D} \quad (D.16)$$

$$\theta'' = \frac{a_2 \phi_2(N_2) [b_1 + \kappa_D \phi_2(O) + \omega_{21} \phi_2(N_2)]}{D} \quad (D.17)$$

where

$$D = [b_1 + (a_1 + \kappa_D) \phi_2(O) + \omega_{21} \phi_2(N_2)] [b_2 + a_2 \phi_2(N_2) + \omega_{12} \phi_2(O)] - a_1 a_2 \phi_2(O) \phi_2(N_2) \quad (D.18)$$

Substituting Equation (D.16) and (D.17) into Equation (D.9), (D.10), and (D.11), we have

$$\gamma_{11} = \frac{2 \kappa_D a_1 \phi_2(O) [b_2 + \omega_{12} \phi_2(O)]}{D} \quad (D.19)$$

$$\gamma_{12} = \frac{\phi_2(N_2) \omega_{12} a_2 [b_1 + \kappa_D \phi_2(O) + \omega_{21} \phi_2(N_2)]}{D} \quad (D.20)$$

$$\gamma_{21} = \frac{\phi_2(O) \omega_{21} a_1 [b_2 + \omega_{12} \phi_2(O)]}{D} \quad (D.21)$$

APPENDIX E

PARTICLE FLUX THROUGH A KNIFE-EDGE ORIFICE OF A MOVING VEHICLE

The angular flux distribution of particles which enter an ionization chamber through a knife-edge orifice depends on the temperature of the ambient gas particles, the velocity of the vehicle, and the direction of the orifice with respect to the direction of motion.

Assuming free molecular flow, the number of particles per unit area and unit time in the velocity interval $\vec{v} + d\vec{v}$ and \vec{v} which flows through the knife edge orifice is

$$d\phi = \vec{v} f(\vec{v}, \vec{u}) d^3v \quad (\text{E.1})$$

where \vec{v} is the velocity and

$$f(\vec{v}, \vec{u}) = \frac{n_o}{\pi^{3/2} C_o^3} \exp \left[- \frac{(\vec{u} - \vec{v})^2}{C_o^2} \right] \quad (\text{E.2})$$

is the Maxwell-Boltzmann velocity distribution of a moving gas in thermal equilibrium. The ambient particle density is n_o , C_o is the most probable velocity of the ambient particles, and \vec{u} is the velocity of the vehicle. We are interested in the flux per unit solid angle in any direction $\vec{\Omega}$. Referring to Figure E.1 the direction can be specified by the angles θ and ϕ . Expressing Equation (E.1) in spherical coordinates

and noting that the projected area in the direction $\vec{\Omega}$ is proportional to $\cos \theta$ we have

$$d\phi(\vec{\Omega}) = \frac{n_o}{\pi^{3/2} c_o^3} v^3 \cos \theta \exp \left[- \frac{(\vec{u} - \vec{v})^2}{c_o^2} \right] \sin \theta d\theta d\phi dv \quad (E.3)$$

or with $d\Omega = \sin \theta d\theta d\phi$

$$d\phi(\vec{\Omega}) = \frac{n_o}{\pi^{3/2} c_o^3} v^3 \cos \theta \exp \left[- \frac{(\vec{u} - \vec{v})^2}{c_o^2} \right] d\Omega dv \quad (E.4)$$

From Figure E.1 the vector difference in the exponent can be evaluated

$$\begin{aligned} (\vec{u} - \vec{v})^2 &= u^2 + v^2 - 2 u v (\sin \alpha \cos \beta \sin \theta \cos \phi + \\ &\quad \sin \alpha \sin \beta \sin \theta \sin \phi + \cos \alpha \cos \theta) \\ &= u^2 + v^2 - 2 u v \cos \Theta \end{aligned} \quad (E.5)$$

where

$$\cos \Theta = \sin \theta \sin \alpha \cos (\phi - \beta) + \cos \theta \cos \alpha \quad (E.6)$$

Substituting Equation (E.5) into Equation (E.4) and integrating over all velocities we obtain

$$\begin{aligned} \phi(\vec{\Omega}) &= \frac{n_o}{\pi^{3/2} c_o^3} \cos \theta d\Omega \int_{v=0}^{\infty} v^3 \exp \left[- \frac{u^2 + v^2 - 2 u v \cos \Theta}{c_o^2} \right] dv \\ &= \frac{n_o}{4} \frac{\bar{v} \cos \theta d\Omega}{\pi} \Lambda(\bar{S}) \end{aligned} \quad (E.7)$$

where \bar{v} is the average thermal velocity of the ambient particles and

\vec{U} - VEHICLE VELOCITY

$\vec{\Omega}$ - DIRECTION OF FLUX
PER UNIT SOLID
ANGLE.

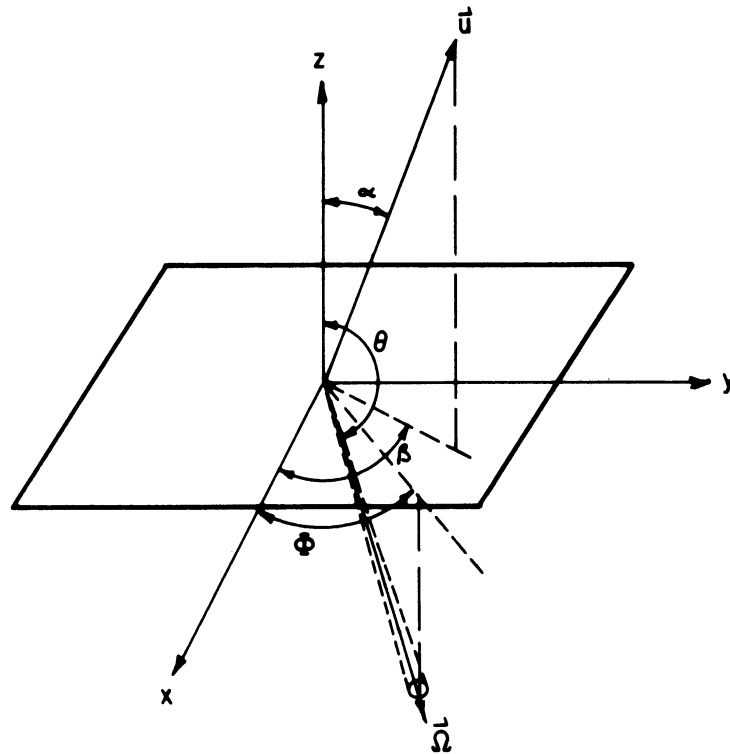


Figure E.1 Vector diagram for the angular distribution of particle flux through a knife edge orifice of a moving vehicle.

$$\Lambda(\bar{S}) = (1 + \bar{S}^2) \exp(-\bar{S}^2) + \sqrt{\pi} \left(\frac{3}{2} \bar{S} + \bar{S}^3 \right) \left[1 + \operatorname{erf}(\bar{S}) \right] \exp \left[-(\bar{S}_0^2 - \bar{S}^2) \right] \quad (\text{E.8})$$

with

$$\bar{S} = \bar{S}_0 \cos \theta \text{ and } \bar{S}_0 = \frac{u}{C_0}. \quad (\text{E.9})$$

Similarly the average particle velocity in the direction $\vec{\Omega}$ is given by

$$\begin{aligned} \overline{v(\vec{\Omega})} &= \frac{1}{\phi(\vec{\Omega})} \int_v v \, d\phi(\vec{\Omega}) \\ &= \frac{n_0}{\phi(\vec{\Omega}) \pi^{3/2} C_0^3} \cos \theta \, d\Omega \int_0^\infty v^4 \exp \left[-\frac{u^2 + v^2 - 2uv \cos \theta}{C_0^2} \right] dv. \end{aligned} \quad (\text{E.10})$$

After integration we obtain

$$\overline{v(\vec{\Omega})} = C_0 \frac{\left(\frac{5}{2} \bar{S} + \bar{S}^3 \right) \exp(-\bar{S}^2) + \sqrt{\pi} \left(\frac{3}{4} + 3\bar{S}^2 + \bar{S}^4 \right) [1 + \operatorname{erf}(\bar{S})]}{(1 + \bar{S}^2) \exp(-\bar{S}^2) + \sqrt{\pi} \left(\frac{3}{2} \bar{S} + \bar{S}^3 \right) [1 + \operatorname{erf}(\bar{S})]}. \quad (\text{E.11})$$

It is of interest to compare the velocity distribution of the particles which enter the chamber during a rocket flight to the velocity distribution of the particles of the atomic oxygen beam. In Figure (3.23) the normalized velocity distribution of atomic oxygen which enters a chamber at normal

incidence during a rocket flight at about 200 km is compared with the velocity distribution of the atomic oxygen in the laboratory beam. The rocket velocity was assumed to be 2000 m/sec and the kinetic temperature of the ambient atomic oxygen was assumed to be 750°K. The kinetic temperature of the atomic oxygen in the beam was assumed to be 2800°K.

The ordinate in Figure (3.23) is labeled in arbitrary units and the curves are normalized so that there are equal areas under the curves.

